Integrated MEMS Technologies for Adaptive Optics

Blake Ching-Yu Lin

Electrical Engineering and Computer Sciences
University of California at Berkeley

Technical Report No. UCB/EECS-2008-94
http://www.eecs.berkeley.edu/Pubs/TechRpts/2008/EECS-2008-94.html

August 14, 2008

Integrated MEMS Technologies for Adaptive Optics

by

Blake Ching-Yu Lin

B.S. (National Taiwan University) 1997
M.S. (University of California, Berkeley) 2002

A dissertation submitted in partial satisfaction of the

requirements for the degree of

Doctor of Philosophy

in

Engineering - Electrical Engineering and Computer Sciences

in the

Graduate Division

of the

University of California, Berkeley

Committee in charge:

Professor Richard S. Muller, Chair
Professor Tsu-Jae King Liu
Professor Liwei Lin

Fall 2008

The dissertation of Blake Ching-Yu Lin is approved:

Chair _____ Date _____

_____ Date _____

_____ Date _____

University of California, Berkeley

Fall 2008

Integrated MEMS Technologies for Adaptive Optics

by Blake Ching-Yu Lin

Abstract

Integrated MEMS Technologies for Adaptive Optics

by

Blake Ching-Yu Lin

Doctor of Philosophy in Engineering - Electrical Engineering and Computer Sciences

University of California, Berkeley

Professor Richard S. Muller, Chair

Image resolutions of modern optical systems are many times limited by wavefront aberrations due to turbulence in the optical media. Adaptive Optics (AO) is a technology that utilizes deformable mirrors (DM) to correct the wavefront distortion, thereby enhancing the image resolution. In this research, we investigate the design and fabrication of micromechanical-deformable-mirror arrays for AO applications. The mirror arrays are produced using surface micromachining techniques developed for the fabrication of Microelectromechanical Systems (MEMS).

Because many AO applications require large arrays (100s-1000s of segments) of closely-spaced deformable mirrors that need to be controlled individually, it is highly desirable that the DM arrays can be integrated with CMOS control electronics. In this research, we develop a CMOS-compatible fabrication

process for MEMS DM arrays, in which polycrystalline-silicon-germanium (poly-SiGe) and polycrystalline-germanium (poly-Ge) are used as the structural and sacrificial materials, respectively.

One major challenge of using poly-SiGe as the structural material is to reduce the high strain gradient in as-deposited poly-SiGe films, because the low-thermal-budget requirement for post-CMOS integration prohibits the use of a high-temperature annealing step. In this research, we demonstrate a means to use bilayer films to modify curving effects in the SiGe platforms that carry the deformable mirrors.

The AO applications also require that the micromechanical deformable mirrors can be controllably moved distances that are relatively large for MEMS (i.e. 10-20 μm). In this research, we demonstrate a means to utilize strain gradients in poly-SiGe to form mirror-support structures that lift the deformable mirrors away from the substrate by large distances (i.e. 10-50 μm), creating room for large mirror movements.

Using the technologies developed in this research, we demonstrate a 37-segment deformable-mirror array that is fabricated using a micromachining process that can potentially be carried out on top of a CMOS integrated circuit built with selection- and drive-electronics for the mirrors. The thermal budget of the demonstrated process is below the maximum allowed for integration with a CMOS 0.25 μm foundry technology. The deformable-mirror array, which has 37 three-degree-of-freedom segments forming an aperture 3.5 mm in diameter, was designed

specifically for use in adaptive-optics applications to vision science. The DM achieves a maximum stroke of 15-17 μm and a maximum tip/tilt angle of 15.7 mrad (0.9 degree) at a maximum actuation voltage of 68 V. The frequency bandwidth of the DM array is approximately 200 Hz. These specifications meet the requirements for vision-science AO applications.

_____

Professor Richard S. Muller, Chair Date

Contents

Acknowledgements

First and foremost, I would like to thank my advisors, Professor Tsu-Jae King Liu and Professor Richard S. Muller, for their guidance through the course of my graduate study at Berkeley. Professor King Liu introduced me to the field of integrated MEMS and gave me the opportunity to work with this promising and challenging material, polycrystalline silicon-germanium. Having no research experience prior to joining the SiGe MEMS group, I learned to approach and to solve problems like a researcher from Professor King Liu. She has been my role model since the day I joined her group. Professor Muller gave me the opportunity to work on the micromirror project. He taught me to always have a clear direction to keep the research in perspective, and to keep a thorough documentation throughout the course of the project, which was extremely beneficial when it came the time to write the dissertation. During the dissertation editing process, Professor Muller spent a tremendous amount of time meticulously teaching me how to put the research results into elegant and professional writing. I feel very grateful and honored to have been mentored by the two greatest advisors.

I am also thankful to Professor Roger T. Howe for his insightful advice at research meetings for many years. Professor Howe's enthusiasm for MEMS is truly inspirational.

Michael A. Helmbrecht introduced me to the micromirror project and provided me with an enormous amount of help over the years whenever I needed it.

He is truly the underground advisor of this research. I am also indebted to Min He, who helped me tremendously with the mirror-assembly process.

There are many other individuals who helped me during the course of this research, including Sunil Bhave, Brian Bircumshaw, Jimmy Chang, Christoph Duenn, Mohan Dunga, Bill Flounders, Bob Hamilton, Joanna Lai, Donovan Lee, Carrie Low, Emmanuel Quévy, Roger Su, Hideki Takeuchi, Matthew Wasilik, Hiu-Yung Wong and Kyoungsik Yu. I would not have been able to complete my research without the help of these individuals.

All the experimental work in this research was conducted in the Berkeley Microfabrication Laboratory. The research was funded by the National Science Foundation Center for Adaptive Optics.

Chapter 1 : MEMS Deformable Mirrors for Adaptive Optics

1.1 Adaptive Optics

Image resolutions of modern optical systems are many times limited by wavefront aberrations due to turbulence in the optical media. When we use a ground-based telescope to observe a star, turbulence in the atmosphere interferes with the traveling light and distorts its wavefront. Because the wavefront is distorted, the image we observe in the telescope becomes blurry. A similar situation occurs in the clinical diagnosis of the human retina. The aberrations in the human eye induced by the cornea, lens, and ocular media cause wavefront distortion in the optical path, resulting in a blurred image.

Adaptive Optics (AO) is a technology that utilizes a deformable mirror (DM) to correct the wavefront distortion, thereby enhancing the image resolution. Figure 1.1 illustrates the concept of using a DM to correct wavefront distortion. The DM deforms in a way that compensates the distortion of the incoming wavefront. The required mirror deformation is exactly half of the wavefront distortion. In every AO system, there is a feedback-control loop that controls the

deformation of the DM. A wavefront sensor senses the distortion in the reflected wavefront. Based on this information, a control unit then determines the required deformation of the DM. The DM receives the control signals and deforms accordingly. Figure 1.2 shows that the image resolutions are much improved through the use of AO systems.

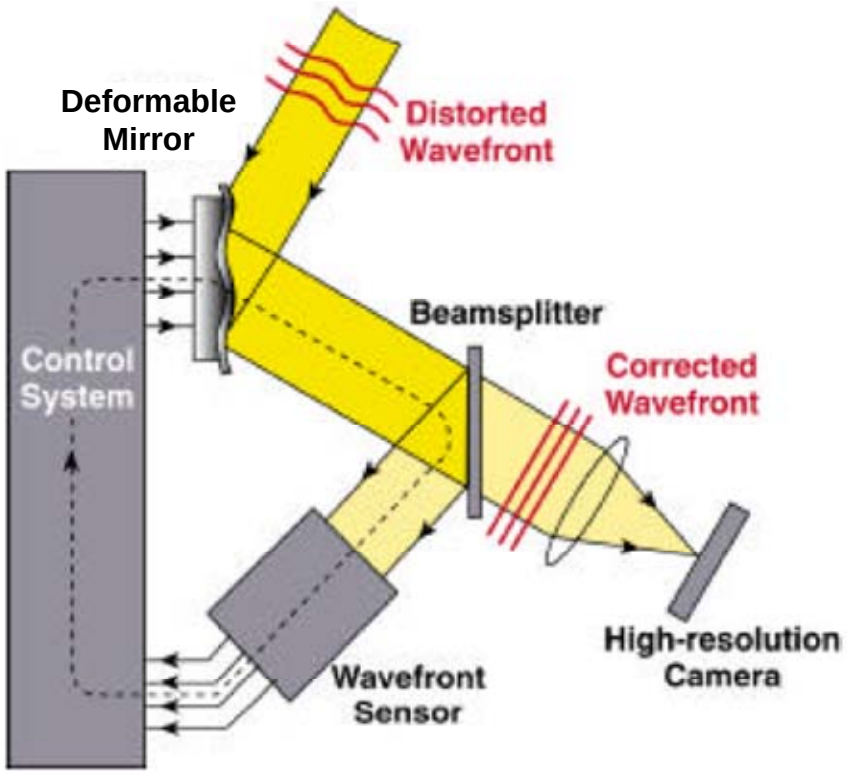

Figure 1.1: A schematic illustrating the concept of adaptive optics. Image credit: Lawrence Livermore National Laboratory and NSF Center for Adaptive Optics.

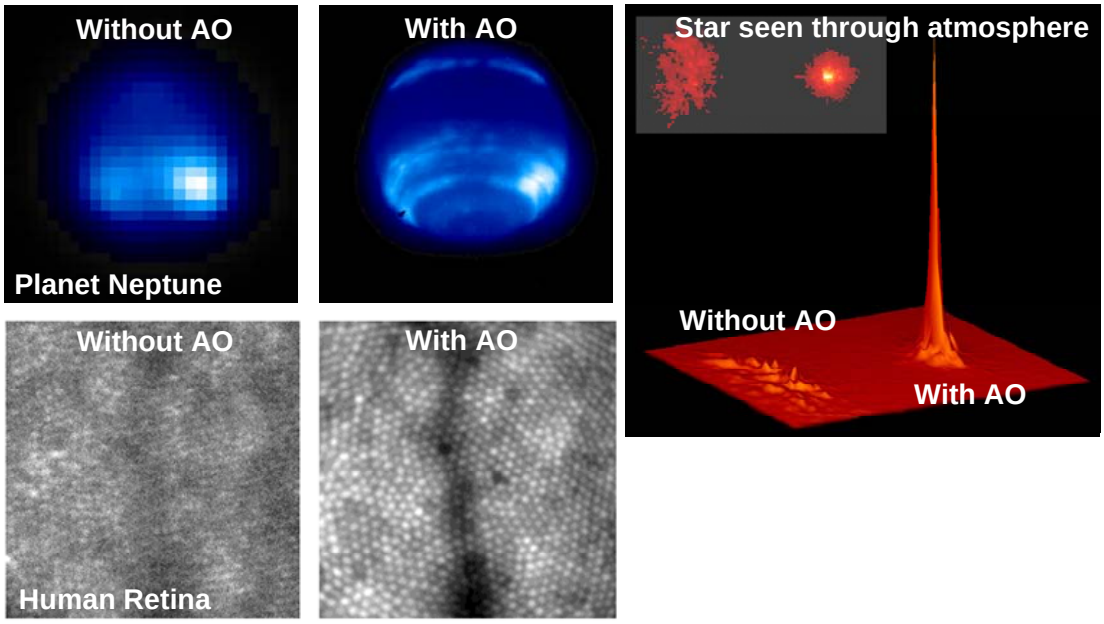

Figure 1.2: Improvement in image resolution through the use of AO systems. Image credit: Lawrence Livermore National Laboratory and NSF Center for Adaptive Optics.

Figure 1.3 illustrates the concept of correcting a distorted wavefront using a deformable mirror. The required deformation on the deformable mirror is half of the distortion in the incoming wavefront. The control system shown in Figure 1.1 controls the deformation of the deformable mirror according to the real-time measurements of the aberrations, measured using the wavefront sensor.

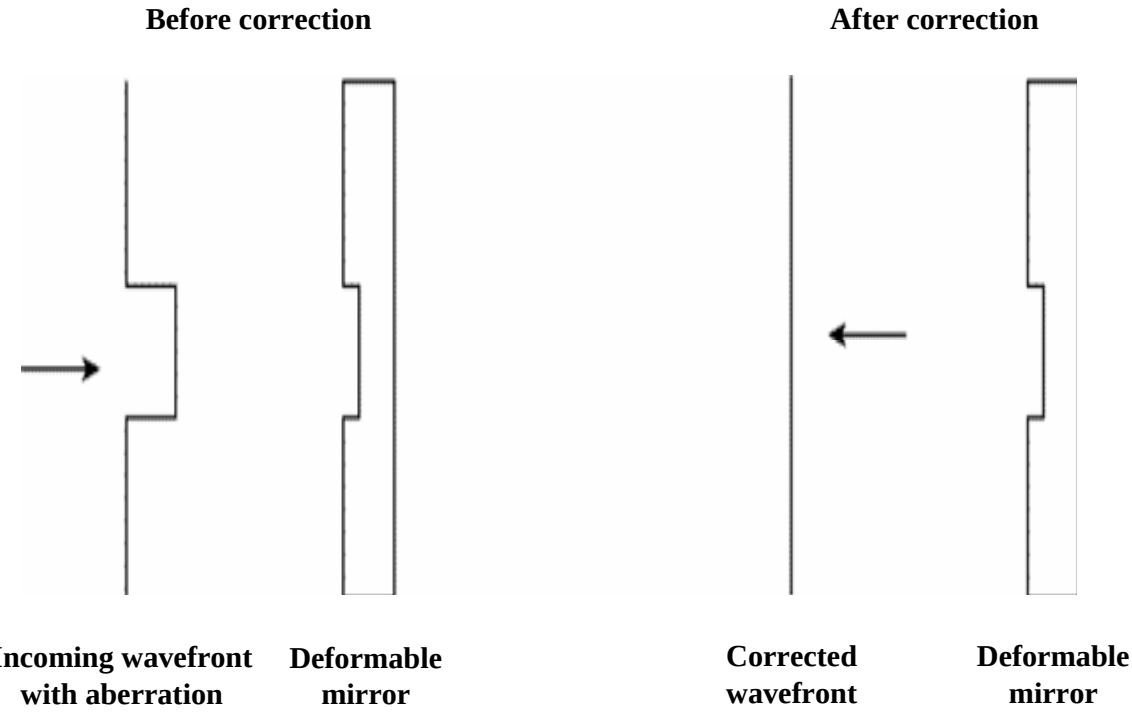

Figure 1.3: Schematics illustrating the concept of correcting a distorted wavefront using a deformable mirror. Image credit: Lawrence Livermore National Laboratory and NSF Center for Adaptive Optics.

Deformable mirrors play a vital role in every AO system. The subject of this research is to develop technologies for deformable mirrors.

1.2 Deformable Mirrors

In this research, we make use of micromachining technologies to fabricate micromechanical deformable mirrors, because the advancement of micromachining technologies has provided a way to fabricate closely-spaced actuator arrays that can

support micromirrors. The micromirror assembly can then be configured to perform adaptive optics.

Deformable mirrors are typically classified into two categories: continuous-face-sheet deformable mirrors and segmented deformable mirrors. A continuous-face-sheet deformable mirror has one continuous mirror surface lying on top of an array of actuators. Because the surface is continuous, when one of the underlying actuators deforms the mirror surface, the deformation also spreads to the surrounding area. As a result, the total deformation caused by each actuator is the combination of the deformation caused by its own actuation with the deformations caused by those surrounding it. This cross-dependency is called cross-talk between actuators.

A segmented deformable mirror is actually an array of closely-spaced mirror segments. Each mirror segment is equipped with its own actuator(s). Hence, the movement of each DM segment is independent of the surrounding segments. Consequently, a segmented DM typically requires a lower actuation voltage to achieve a similar amount of deformation compared to the voltage needed for a continuous-face-sheet DM of similar dimensions. One shortcoming of the segmented structure is the diffraction caused by the edges of the segments. Therefore, to overcome the diffraction, it is desirable that each segment can be actuated in both piston mode and tip/tilt mode. The multiple-degrees-of-freedom motions allow the micromirrors to exhibit smooth transitions between segments, making the segmented deformable surface appear closer to a continuous face sheet.

The goal of this research is to demonstrate deformable mirrors that can be integrated with CMOS control electronics. The maximum voltage that can be supplied by CMOS electronics is limited by the breakdown voltage of the transistors. Therefore, we chose a segmented structure for the reason that it requires a lower actuation voltage to achieve a similar amount of deformation compared to a continuous-face-sheet structure of similar dimensions.

1.3 Deformable-Mirror Specifications

The specifications for a DM are application-dependent. In this research, we are concerned with applications in vision science. Key specifications for a segmented DM include aperture size, stroke, frequency bandwidth, fill factor, mirror-surface flatness, and segment count. Aperture size is the area of the DM that receives and reflects light. Stroke is the maximum distance a mirror segment can deflect from its original position. Cut-off frequency is the highest frequency at which the mirror segment can be actuated. Fill factor is the percentage of the entire DM surface that is reflective (the gaps between mirror segments are not reflective). Mirror-surface flatness measures the deviation from planarity in the reflective surface, resulting from residual stresses and/or surface roughness. Segment count is the number of mirror segments. For a fixed aperture size, higher segment counts lead to higher resolution in the optical system.

To our knowledge, there is not yet a mathematical model that predicts the time-varying aberrations in the human eye. Accordingly, we base our research for AO applied to retinal optics on parameters drawn from population studies. Population studies show that to correct wavefront distortions fully in a 3.5 mm (diameter) pupil (human average), a stroke of 20 μm is required [1]. For images that have had the defocus aberrations removed prior to entering the AO system, the requirement on stroke can be relaxed to 10 μm [1]. Ideally, the aperture size should be the same as the pupil size. If the aperture size of the deformable mirror is larger than the pupil size, additional optics would be required to magnify the retinal image before the image enters the AO system. The space required to accommodate the additional optics is proportional to the ratio of the aperture size to the pupil size. Therefore, an aperture size that is many times larger than the pupil size is not suitable for a clinical setup. As for the specifications on segment count and fill factor, population studies show that about 37 segments with fill factor of 98% are required if using a three-degrees-of-freedom segmented DM [1].

Mirror-surface flatness is related to the optical quality of the mirror surface. In an optical system, flatness is typically specified by system designers to be less than 1/20 of the sampled wavelength [1]. For vision-science applications, visible red light (wavelength = 600 nm) is often used as the defining wavelength. Therefore, the root-mean-square (rms) surface deformation in the mirrors is specified to be lower than 30 nm.

Aberrations in the light rays traversing the eye occur at roughly 1 to 2 Hz. AO systems typically sample at 10 times the frequency of the distortion to be corrected, and the DMs are typically required to have a flat response at frequencies that are 5 to 10 times the sampling frequency. Hence, the DMs are required to have a frequency bandwidth of at least 200 Hz for vision-science applications. Table 1.1 summarizes the specifications for DMs in vision-science AO systems.

Table 1.1: Specifications for DMs in vision-science AO systems

Aperture size	3.5 mm
Stroke	10 to 20 μm
Segment count (3 DOF segmented DM)	37
Fill factor	98%
Mirror-surface deformation (root mean square)	30 nm
Frequency bandwidth	200 Hz

1.4 State-of-the-Art Deformable Mirrors

Table 1.2 is adapted from Devaney et al. [2] (published in January 2008), in which eight commercially available deformable mirrors are characterized to determine their suitability as the wavefront corrector in adaptive-optics systems. Details about these deformable mirrors are published in [3-5].

Table 1.2: Characteristics of state-of-the-art deformable mirrors

Mirror	Technology	Aperture (mm)	Actuators	Stroke (μm)	Actuation voltage
OKO37	Electrostatic	15	37	0.3-0.6	150 V
O19_PZT	Piezoelectric	30	19	3, 7-9	400 V
AOptix35	Bimorph	10.2	35	3, 7	300 V
MIRAO52	Magnetic	15	52	10-15	1 V (50 A)
BMC140	Electrostatic	3.3×3.3	140	1.5	275 V
AgilOptics37	Electrostatic	16	37	0.2, 0.6	n/a
IrisAO37	Electrostatic	3.5	37	7	60 V
OKO37_PZT	Piezoelectric	30	37	2, 3.5-5	400 V

Among the eight DMs shown in Table 1.2, The BMC140 DM and IrisAO37 DM are the only two DMs that have aperture sizes comparable to the size of human pupil. The BMC140 DM can only be actuated in piston mode and hence has a larger number of actuators (140). The IrisAO37 DM is the only segmented DM, whereas all the other seven DMs are continuous-face-sheet DMs. As a result, the IrisAO37 DM requires the lowest actuation voltage compared to the other DMs except the MIRAO52 DM, which is actuated using magnetic force. The MIROAO DM provides the largest stroke (10-15 μm) with a low actuation voltage (1 V) but a high actuation current (50 A). This is due to the fact that the magnetic force is proportional to the square of the current flowing in the toroids that are placed underneath the continuous-face-sheet mirror surface. The high power consumption (50W) of the magnetic DM makes it unsuitable for integration with CMOS. Most of the DMs shown in Table 1.2 require high actuation voltages (>150V), which also make them unsuitable for integration with CMOS. In fact, none of the eight DMs shown in Table 1.2 is fabricated using a process that can be integrated with CMOS. As far as the stroke is concerned, the MIRAO52 DM is the only DM that can

provide strokes larger than 10 μm. However, the aperture size of the MIRAO52 DM (15 mm) is also significantly larger than the size of human pupil (3.5 mm). Therefore, with the same technology, the MIRAO52 DM would not be able to provide the same amount of stroke if its aperture size were to be scaled to the size of the human pupil.

1.5 Design of a Large-Stroke Integrated Micromechanical Deformable Mirror

As shown in Table 1.1, the specifications for a DM require a closely-spaced array of actuators. Therefore, it is desirable to integrate the micromechanical mirrors and actuators with CMOS control electronics. An integrated DM, in which the micromechanical mirrors and actuators are fabricated directly on top of CMOS control electronics, can provide higher performance (due to lower parasitics) at lower cost (one packaging and fewer wire-bonding connections). In this research, we investigate the possibility of fabricating a large-stroke micromechanical DM using a CMOS-compatible micromachining process. The actuation voltages required to drive the DM should also be within the breakdown voltages of modern CMOS technologies. For example, as of early 2008, the highest-voltage CMOS technology offered through MOSIS for engineering runs is an 80-V 0.8-μm CMOS technology.

Figure 1.4 illustrates our design of a large-stroke integrated micromechanical deformable mirror for vision-science AO applications. As

discussed in Section 1.2, we chose a segmented structure over a continuous-face-sheet structure because to achieve a similar amount of maximum stroke, the maximum voltage required to drive a segmented DM is typically lower than that for a continuous-face-sheet DM. To minimize the diffractions caused by the edges of the segments in a segmented DM, we design each segment in a way such that it can move in both piston mode and tip/tilt mode. As shown in Figure 1.4, the DM segment we design in this research is a hexagonal-shape structure with three underlying diamond-shape electrodes. To actuate the DM segment, we bias the top electrode at the ground potential and supply driving voltages to the three bottom electrodes. The electrostatic force between each bottom electrode and the top electrode is proportional to the square of the voltage supplied to the bottom electrode. As a result, the DM segment moves in piston mode when the same voltage is supplied to all the three bottom electrodes, and in tip/tilt mode when different voltages are supplied to the three bottom electrodes.

In our design, 37 mirror segments are closely positioned to form a high-fill-factor aperture of 3.5 mm in diameter. The aperture size of 3.5 mm and the actuator count of 37 are designed in accordance to the specifications shown in Table 1.1. As a result, each hexagonal-shape DM segment is about 350 μm on each side. To achieve a fill factor greater than 98%, the gap between the segments is designed to be 4 μm.

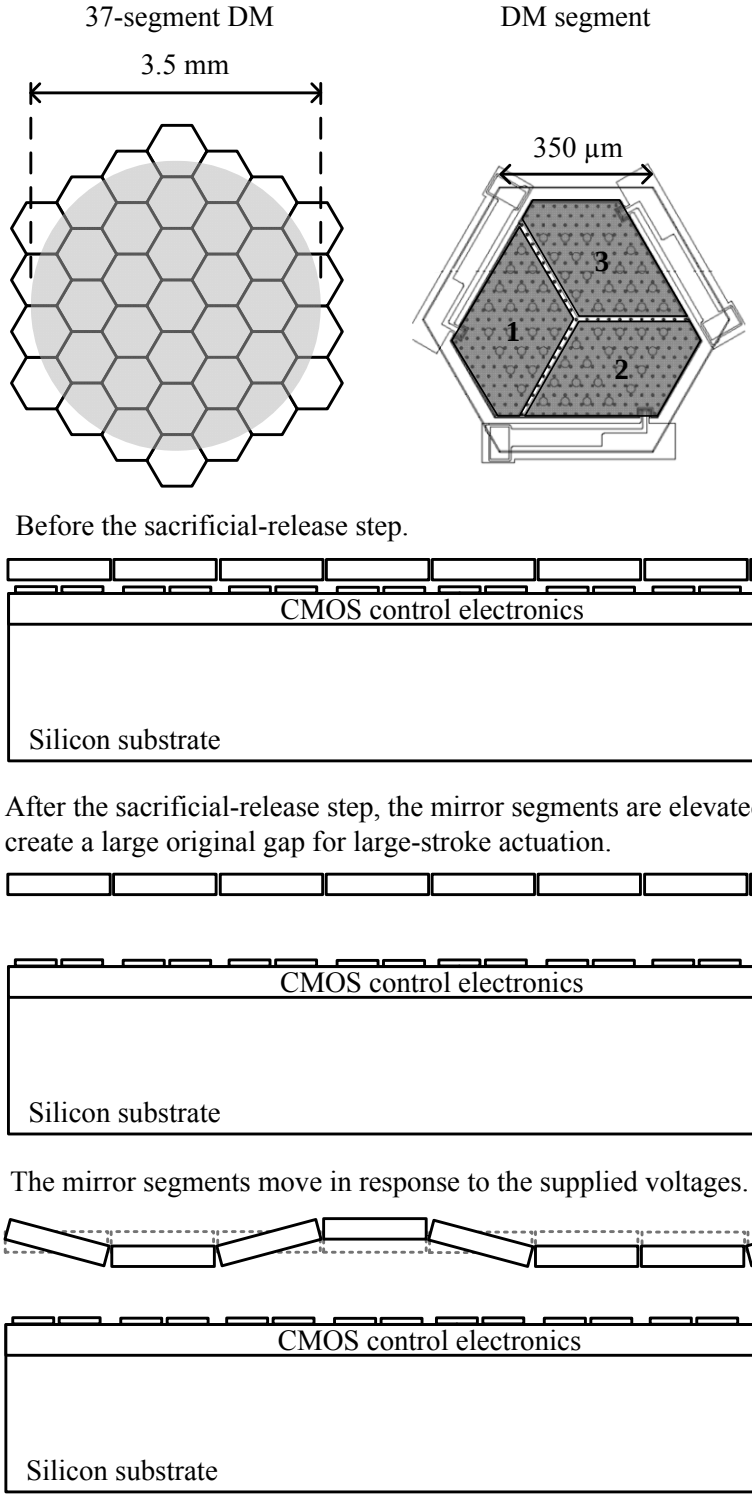

Figure 1.4: Schematic sketches illustrating our design of a large-stroke micromechanical segmented DM.

The specifications for DMs used in vision-science AO systems require a stroke of 10 to 20 μm, as shown in Table 1.1. The maximum stroke that an electrostatic parallel-plate actuator can achieve is typically limited to one-third of the original gap between the parallel plates, which is called the pull-in limit. Therefore, in order to achieve 15 μm of stroke, the original gap of the parallel-plate actuator needs to be at least 45 μm. Conventionally, the original gap of a parallel-plate actuator fabricated using surface micromachining process is equal to the thickness of the sacrificial layer deposited between the bottom-electrode and the top-electrode layers. However, it is impractical to deposit 45 μm of sacrificial material in order to obtain an original gap of 45 μm, because the deposition time would be excessively long for integration with CMOS (about 50 hours at 400°C if low-temperature oxide is the sacrificial material, or about 135 hours at 350°C if polycrystalline germanium is the sacrificial material). Moreover, the thicknesses of the structural layers that are deposited before and after the sacrificial layer are 0.25 μm and 0.9 μm, respectively (the reasons for the choices of these thicknesses are discussed in Chapter 4). With a sacrificial-layer thickness of 45 μm, it would require an etch selectivity of 180:1 during the anchor-hole-opening step to etch through the 45 μm-thick sacrificial layer and stop on the underlying 0.25 μm-thick layer. After the anchor holes are opened, the deposition of the 0.9 μm-thick structural layer would also need to cover a step height of 45 μm.

Therefore, in order to obtain a large original gap for large-stroke actuation, our design of the segmented DM incorporates a novel structure of flexural supports that elevates the mirror segments after the sacrificial-release step to create an original gap that is much larger than the thickness of the sacrificial layer, as shown in Figure 1.4. The designs of the flexural supports are discussed in Chapter 3.

To take full advantage of the integration of the micromechanical elements and the control electronics, it is desirable to fabricate the control electronics using a foundry CMOS technology, which can typically provide high performance, consistent quality, and low cost. The micromechanical parts of an integrated DM, including the actuators and the mirrors, are fabricated after the control electronics. Therefore, it is required that the fabrication process for these elements is compatible with the foundry CMOS technology. This requirement sets an upper limit on the thermal budget of the process producing the micromechanical elements.

1.6 Polycrystalline Silicon-Germanium for Post-CMOS Integration of Micromechanical Structures

Polycrystalline silicon-germanium (poly-SiGe) is a promising material for post-CMOS integration of micromechanical structures because poly-SiGe can be deposited at temperatures below 450°C using a LPCVD furnace, and the electrical and mechanical properties of poly-SiGe are similar to those of polysilicon [6-9].

The poly-SiGe films can be *in-situ* doped to achieve low resistivity (~0.55 mΩ-cm [10]). Research conducted by Eyoum et al. [11] at UC Berkeley has also shown that p-type poly-SiGe can de directly deposited onto a CMOS metal interconnect layer (i.e. TiN-coated Al-2%Si) to form a low-resistance contact (contact resistivity ~ 2-5 $\mu\Omega\text{-cm}^2$).

Furthermore, when a poly-SiGe film with germanium content below 70% is used as the structural material, we can use polycrystalline germanium (poly-Ge) as the sacrificial material and use hydrogen peroxide (H_2O_2) as the release etchant to remove poly-Ge during the sacrificial-release step. Hence, using poly-Ge as the sacrificial material allows us to avoid the use of hydrofluoric acid (HF) in the sacrificial-release step, which is undesirable for post-CMOS integration because the materials used in the interconnect stacks of most CMOS technologies (i.e. aluminum and silicon dioxide) do not have etch resistance to HF. Research conducted by Bircumshaw et al. [12] at UC Berkeley showed that the etch rate of *in-situ*-doped poly-Ge in 90°C H_2O_2 is 0.5 $\mu\text{m-min}^{-1}$, whereas the etch rate of *in-situ*-doped poly-SiGe with a germanium content of 70% is 4 nm-min^{-1}. The etch rate of poly-SiGe in H_2O_2 is nearly zero if the germanium content is below 65%.

Figure 1.5 shows a SEM photo of a post-CMOS integrated micromechanical comb-drive resonator demonstrated by Franke et al. [13]. The micromechanical resonator is formed of a 3 μm-thick poly-SiGe, deposited at 450°C for 3 hours. The underlying control electronics for the micromechanical

resonator were fabricated using a baseline 3-μm-gate-length CMOS technology in the UC Berkeley Microfabrication Laboratory.

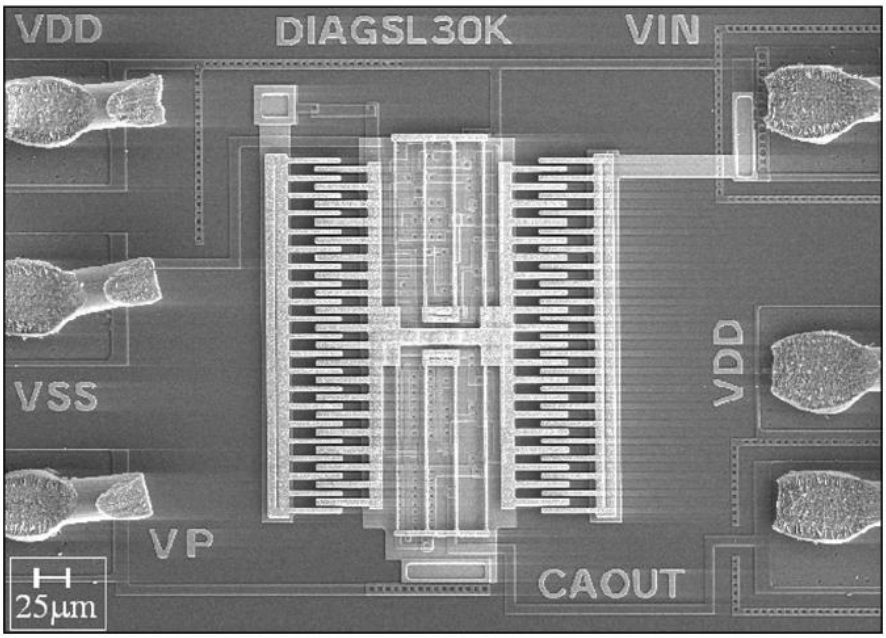

Figure 1.5: SEM photo of a post-CMOS integrated micromechanical resonator fabricated using poly-SiGe. Image credit: Franke et al. [13].

Poly-SiGe films deposited at temperatures between 425 and 450°C exhibit low residual stress (within ±100 MPa) but high strain gradients (on the order of 10^{-3}-10^{-4} μm^{-1} for a film thickness of about 2 μm, depending on the deposition conditions). Figure 1.6 shows a cantilever array formed of 2 μm-thick poly-SiGe deposited at 450°C. The lengths of the cantilevers range from 50 μm to 1 mm. Due

to the strain gradient in the poly-SiGe film, the freed ends of the 100, 200, and 300 μm-long cantilevers deflect out-of-plane by approximately 0.5 μm, 2 μm, and 4.5 μm, respectively, measured using a Wyko interferometer. The deflection of each cantilever is proportional to the square of the beam length.

The definition of strain gradient is the change in strain per unit thickness of the film. According to the beam theory, the strain gradient is equal to the reciprocal of the radius-of-curvature, and can be calculated from the vertical deflection at the freed end of a cantilever using the flowing equation.

$$\frac{1}{\rho} = \frac{2y}{L^2} \qquad 1.1$$

where

$\frac{1}{\rho}$ is the strain gradient of the film.

ρ is the radius-of-curvature of the cantilever as a result of the strain gradient.

y is the vertical deflection at the free end of the cantilever.

L is the length of the cantilever.

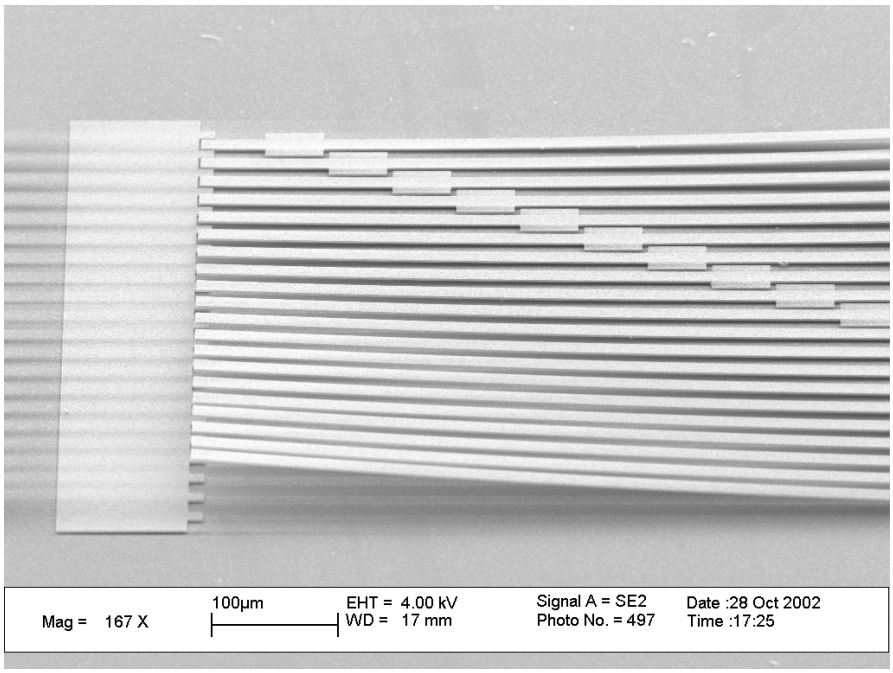

Figure 1.6: SEM photo of a cantilever array formed of a 2 µm-thick poly-SiGe film deposited at 450°C.

Using Equation 1.1, the strain gradient of the cantilever array shown in Figure 1.6 is calculated to be approximately 10^{-4} μm^{-1} (the radius-of-curvature is approximately 10 mm). Equation 1.1 also indicates that, for a given strain gradient, the out-of-plane deflection of a cantilever is proportional to the square of the length of the beam, which is the same relationship observed from the deflection measurements of the cantilever array shown in Figure 1.6.

Using Equation 1.1, we can calculate the deflection of a cantilever of arbitrary beam length for a given strain gradient. For example, with a strain

gradient of 10^{-4} μm^{-1}, the deflection at the freed end of a 50 μm-long cantilever is calculated to be 0.125 μm. The same strain gradient would cause a 350 μm-long cantilever to deflect by 6 μm at the freed end. Therefore, the strain gradient of poly-SiGe is not of significant concern for structures with small dimensions such as the micromechanical resonator shown in Figure 1.5.

The hexagonal DM segment shown in Figure 1.4 is about 350 μm on each side. If the hexagonal segment is formed of a poly-SiGe layer with a strain gradient of 10^{-4} μm^{-1}, the strain gradient would cause the surface of the segment to curve and exhibit a shape similar to a dish, with a difference in height of approximately 6μm between the center and the vertices of the hexagon, estimated using Equation 1.1. Hence, we need to take the strain gradient into consideration when designing the micromechanical DM structures using poly-SiGe as the structural material. In Chapter 2, we discuss the use of a bilayer structure to reduce the strain gradients in as-deposited poly-SiGe films. We first discuss how the residual stresses and strain gradients of poly-SiGe films can be controlled via deposition conditions. Then we present mathematical models and experimental results for the bilayer structure.

On the other hand, we can utilize the strain gradient of poly-SiGe to fabricate curving beams that elevate the DM segments to create the large original gap for large-stroke actuation. The design, modeling, and demonstration of the poly-SiGe flexural supports to enhance mirror elevations are discussed in Chapter 3.

In Chapter 4, we discuss and the design, modeling, and demonstration of a 37-segment large-stroke micromechanical DM array that incorporates both the bilayer poly-SiGe structure described in Chapter 2 (which is used to form the platforms that carry the micro mirrors) and the poly-SiGe flexural supports described in

Chapter 5 summarizes the contributions of this research and suggests future research directions.

1.7 Conclusion

In this chapter, we discuss the motivations and goals of this thesis research. After discussing the specifications for DMs used in vision-science AO systems, we review the performance of the state-of-the-art deformable mirrors, and then present our design of a large-stroke segmented DM, which is schematically shown in Figure 1.4. The goal of this thesis research is to demonstrate this DM design using micromachining technologies that can allow the DM to be integrated with CMOS control electronics. The following chapters of this dissertation discuss the developments of the micromachining technologies that are required to demonstrate the segmented DM structure presented in this chapter.

Chapter 2 : A Bilayer Structure to Reduce the Curvature of Surface-Micromachined Polycrystalline-Silicon-Germanium Films

2.1 Low-Pressure Chemical-Vapor-Deposition of Polycrystalline-Silicon-Germanium

In this chapter, we present the mathematical model and experimental results of using a bilayer structure to reduce the curvature of surface-micromachined polycrystalline-silicon-germanium (poly-SiGe) films. The poly-SiGe films were deposited in a Low-Pressure Chemical-Vapor-Deposition (LPCVD) furnace at the Microfabrication Laboratory of University of California, Berkeley.

The furnace is equipped with controllers for the temperature, pressure, and flow rates of the reactants during each deposition. The reactants used in this research include silane (SiH_4), germane (GeH_4), 1% boron trichloride (BCl_3) in helium (since March 2005), and 10% diborane (B_2H_6) in hydrogen (before March 2005). Silane and germane react to form SiGe, and boron trichloride (or diborane) decomposes during the deposition to *in-situ* dope the SiGe film with boron.

Previous research conducted at UC Berkeley has shown that we can deposit poly-SiGe films with low resistivity (~1 mΩ-cm) and low residual stress (< ±100 MPa) using the LPCVD furnace [14-15]. However, freed micromechanical structures made of the poly-SiGe films exhibit large curvature (caused by high strain gradients). When measured using released cantilever beams, the radius-of-curvature is in the range of 1 to 10 mm, which is too high for many designs of micromechanical structures. The curvature corresponds to a strain gradient in the deposited material. A radius-of-curvature of 1 mm is typically caused by a strain gradient of 10^{-3} μm^{-1}.

The research presented in this chapter was motivated by the goal of finding a solution that could reduce the curvature of poly-SiGe microstructures.

2.2 A Design-of-Experiment to Characterize the Effects of Deposition Parameters on the Residual Stress and Strain Gradient of LPCVD Poly-SiGe

A Design-of-Experiment (DOE) was conducted in 2002 to characterize the effects of deposition parameters on the residual stress and strain gradient of poly-SiGe. The DOE had three parameters: temperature, pressure, and flow rate of GeH_4 (the flow rates of all the other reactants were kept constant) and is illustrated with a cube in Figure 2.1. The 15 dots represent the 15 runs of this DOE. The flow rates of

SiH_4 and 1% B_2H_6 were 100 sccm and 60 sccm, respectively, in all 15 runs. The order of the runs was randomly selected.

The ranges of the parameters were determined based on the results of depositions conducted in the same furnace before the DOE. Poly-SiGe films deposited in the selected ranges of temperature, pressure, and flow rate of reactants have Ge content between 60% and 70%. As reported in [16], SiGe films deposited at 425-450°C need to have Ge content above 60% to become polycrystalline, and below 70% in order to have resistance to H_2O_2 etch. The resistance to H_2O_2 etch is required for poly-SiGe when pure Ge is used as the sacrificial material, which is etched away by H_2O_2 during sacrificial release.

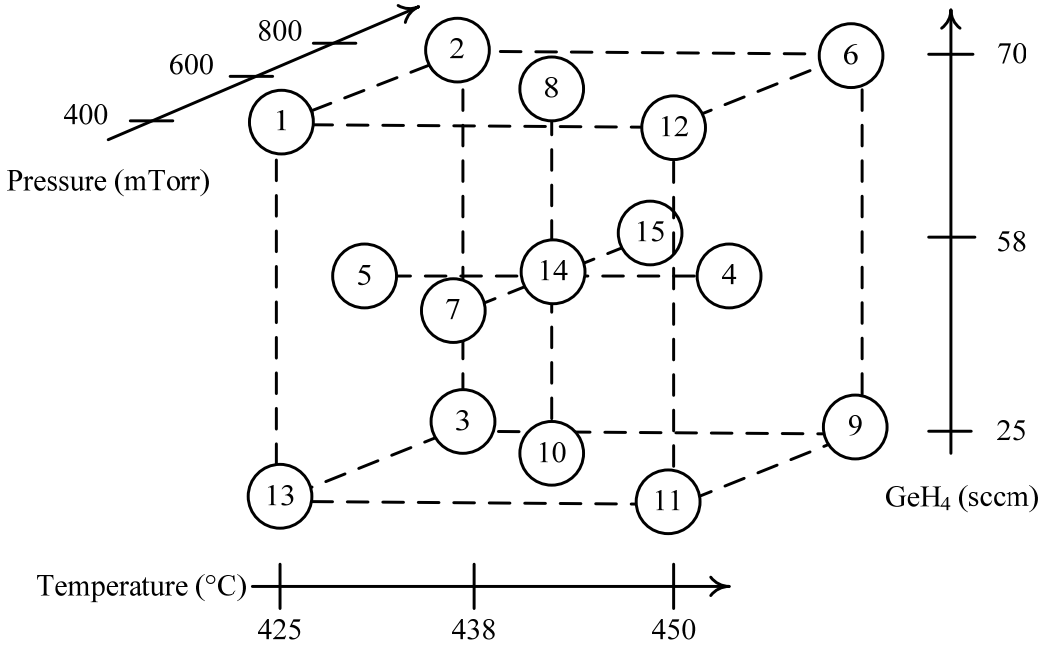

Figure 2.1: A cube that illustrates the 3-parameter, 15-run Design-of-Experiment.

The fabrication process for the DOE was a single-mask process using Low-Temperature-Oxide (LTO) deposited at 400°C as the sacrificial material. Figure 2.2 illustrates the process flow.

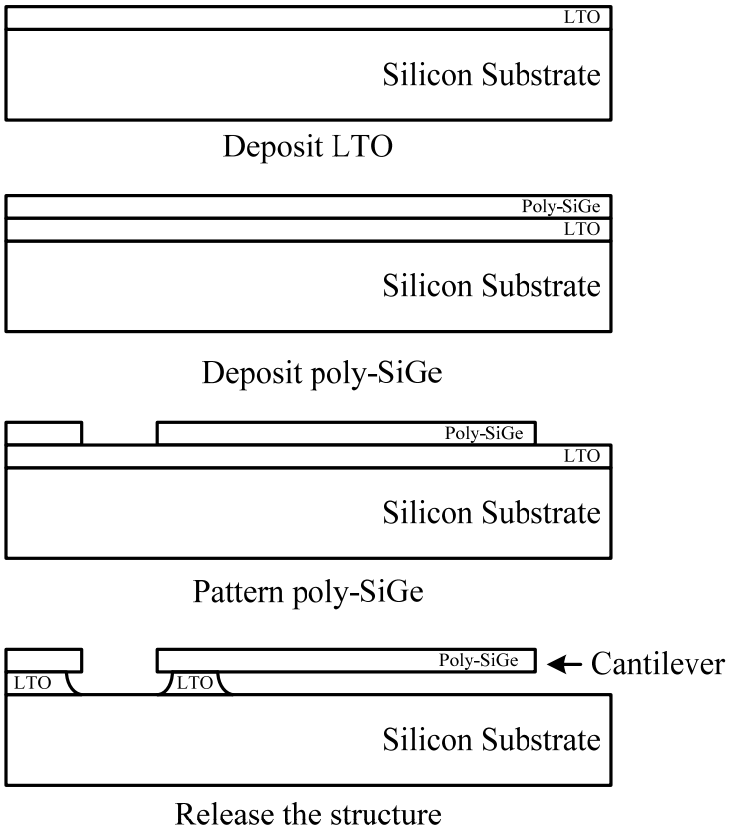

Figure 2.2: The single-mask process to fabricate SiGe cantilevers on LTO.

The process began with a deposition of 2 μm undoped low-temperature oxide (LTO) at 400°C, followed by the deposition of poly-SiGe (~2 μm). The poly-SiGe was then patterned. The lithographic mask contains patterns of a cantilever array that was used to measure the strain gradient in the SiGe film. Figure 2.3 shows the top view of the cantilever array before the sacrificial release step.

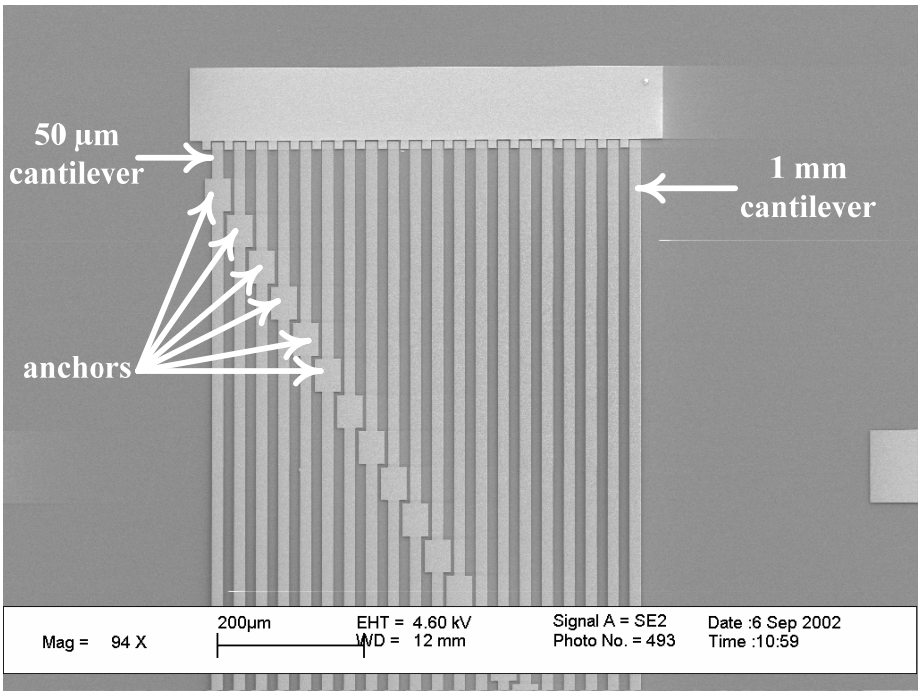

Figure 2.3: SEM photo of a SiGe cantilever array after patterning, but before the sacrificial release step.

The poly-SiGe cantilevers were released by etching away the sacrificial LTO in concentrated hydrofluoric acid (49% HF). Because the sacrificial LTO layer was not patterned, the structural poly-SiGe was not in direct contact with the silicon substrate. Therefore, the poly-SiGe structures were designed to be twice as wide at the "anchor" areas, as seen in Figure 2.3. The release step was timed and monitored, and was stopped when the LTO underneath the cantilevers was completely undercut. The etch rate of 400°C LTO in concentrated HF was also calibrated (~1 µm/min) for the release step. Because the out-of-plane bending of

the 1 mm cantilever was very high in most of the 15 runs, it was possible to see the bending with naked eyes after the cantilevers were released.

The curvature of the cantilevers was measured using a Wyko interferometer. Figure 2.4 shows a SEM photo of a released poly-SiGe cantilever array. (We did not take a SEM photo for any of the cantilever arrays made in the DOE. The cantilever array shown in this photo was made in a run after the DOE.) The interferometer measures the radius-of-curvature and the out-of-plane deflections at the tips of the cantilevers. The strain gradient was calculated using Equation 1.1.

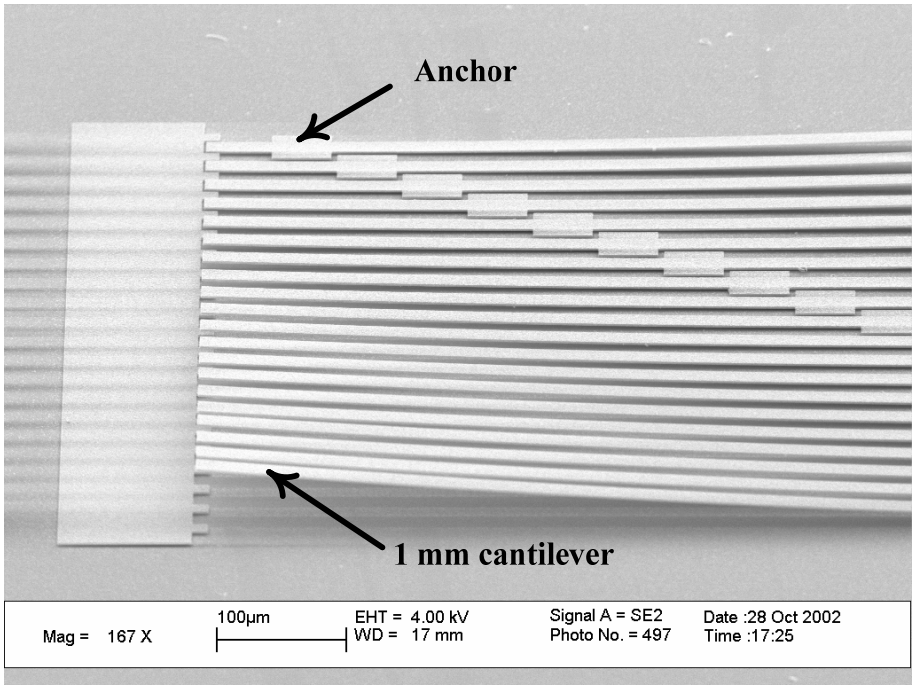

Figure 2.4: SEM photo of a released poly-SiGe cantilever array.

At the time the DOE was conducted, the residual stress of the poly-SiGe was measured using on-chip stress verniers. Figure 2.5 shows a schematic of a specially designed measurement structure that is useful for measurements of compressive residual stress in the beam cross sections. Any residual stress causes beams A and B (in Figure 2.5) to extend (compressive residual stress) or contract (tensile residual stress). As a result of these dimensional changes beam C rotates either clockwise or counterclockwise, respectively. The measurement structure "amplifies" the movements caused by the residual stress making it more easily detectable at the verniers. The structure was designed by Dr. Sunil A. Behave during his time as a doctoral student at Berkeley, but it never appeared in any of his publications.

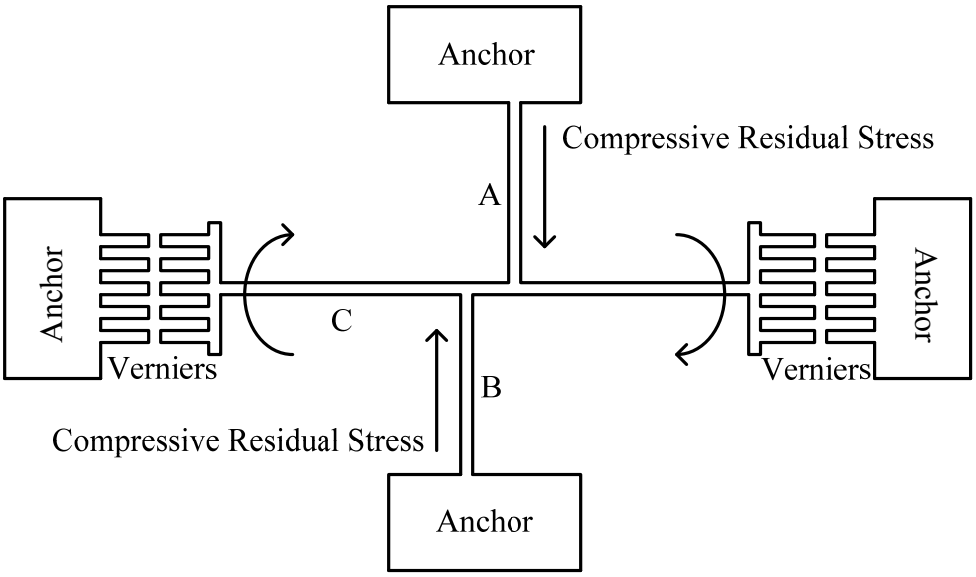

Figure 2.5: Schematic of on-chip stress-detection verniers used to determine residual stress in released poly-SiGe beams.

Due to the high stress gradients in the poly-SiGe films, the verniers at both ends of beam C deflect out-of-plane after the sacrificial release step. Because we do not have a microscope that has a depth-of-focus deep enough to show both the deflected and anchored verniers in one focus, in order to read the residual stress, we focus the microscope on the deflected verniers first, mark the locations of the major teeth of the verniers on the display of the microscope, and then refocus the microscope on the anchored verniers to read the disparity between its major teeth and the marks on the display. Because we can only read the major teeth of the verniers, and the major teeth was designed such that the residual stress required to rotate beam C by one major tooth is 3 MPa, all the measurements we take for the residual stress are multiples of 3 (i.e. 0, 18, 27, 36…), as seen in Figure 2.6. Therefore, the minimum detectability of this measurement is 3 MPa.

The measured values of residual stress and strain gradients of all the 15 DOE runs are shown in Figure 2.6. Because the minimum detectability of the residual-stress measurements is 3 MPa, we use the term “close to 0” for the films that exhibit residual stress below this minimum detectability when they are measured using the on-chip stress verniers.

Run	Temperature (°C)	Pressure (mTorr)	GeH_4 (sccm)	Residual Stress (MPa)	Strain Gradient (10^{-4} μm^{-1})
1	425	400	70	close to 0	2.3
2	425	800	70	-36	4.7
3	425	800	25	-36	4.6
4	450	600	58	-36	2.0
5	425	600	58	-63	3.2
6	450	800	70	-27	3.5
7	438	400	58	close to 0	3.5
8	438	600	70	close to 0	3.2
9	450	800	25	-36	7.2
10	438	600	25	-36	6.2
11	450	400	25	-36	4.2
12	450	400	70	18	2.3
13	425	400	25	close to 0	6.2
14	438	600	58	close to 0	3.1
15	438	800	58	close to 0	4.4

Figure 2.6: Measured residual stress- and strain- gradients of poly-SiGe films deposited in the DOE.

Figure 2.7 is a plot of the residual-stress and strain-gradients versus temperature, pressure, and GeH_4 flow rate. Each plot is made up using data from all 15 measurements listed in Figure 2.6. There are fewer than 15 points on the plots because of duplications in the deduced values of residual stress or strain gradient which overlie one another on the plots. The straight line in each plot represents the first-order trend calculated from all 15 data points.

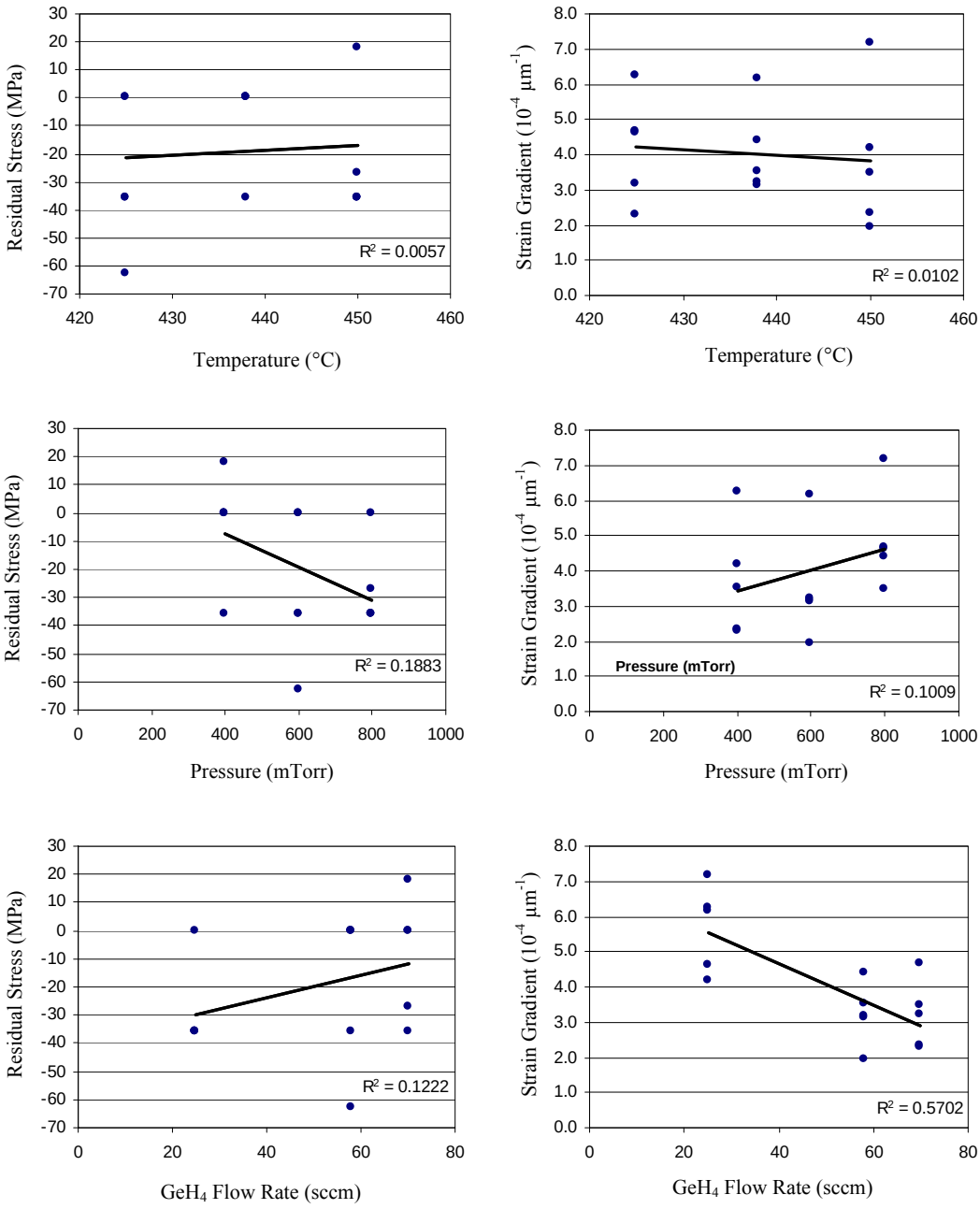

Figure 2.7: Plots of residual-stress values and strain gradients as functions of temperature, pressure, and GeH_4 flow rate. Figure 2.6 is the source of data.

As observed in Figure 2.7, the data points are scattered in each of the 6 plots. Therefore, from the results of the DOE, we cannot conclude that, in the selected ranges of deposition parameters, temperature, pressure, or GeH_4 flow rate has a linear effect on the residual stress or strain gradient in the deposited poly-SiGe. Nonetheless, the DOE provided us with approximate trends that are caused by changes in each of the fabrication parameters. The results of these experiments imply that: films deposited at higher temperature, lower pressure, and higher GeH_4 flow rate (or GeH_4/SiH_4 ratio, since the SiH_4 flow rate was fixed) exhibit more tensile (or less compressive) residual stress and lower strain gradients.

As discussed in the next section, we use a bilayer structure to reduce the curvature of poly-SiGe. To accomplish this reduction in curvature, the two layers need to have slightly different residual stresses (the residual stress of the top layer needs to be more compressive than is that of the bottom layer). We will use the trends obtained from the DOE as guidelines to adjust the eventual curvature through choice of the deposition parameters.

2.3 The Stress Gradient in Poly-SiGe

The lowest strain gradient we obtained in the DOE was 2×10^{-4} μm^{-1} (Run 4), equivalent to a radius-of-curvature of 5 mm. To demonstrate the concept of using a bilayer structure to reduce the curvature, we chose two deposition recipes from the DOE: Run 12 (fabrication conditions: 450°C, 400 mTorr, SiH_4 100 sccm, GeH_4 70 sccm, B_2H_6/H_2 60 sccm) for the top layer, and Run 5 (fabrication

conditions: 425°C, 600 mTorr, SiH_4 100 sccm, GeH_4 58 sccm, B_2H_6/H_2 60 sccm) for the bottom layer. The reason for these choices was that, compared to the other films deposited in the DOE runs, the film deposited in Run 12 exhibited the highest tensile residual stress, and the film deposited in Run 5 exhibited the highest compressive residual stress. Moreover, the strain gradients of these two films were 2.3×10^{-4} μm^{-1} (Run 12) and 3.2×10^{-4} μm^{-1} (Run 5), which are both below the average strain gradient of the 15 DOE runs (4×10^{-4} μm^{-1}).

Figure 2.8 shows SEM photos of two films: a 2 μm-thick poly-SiGe film (fabrication conditions: 450°C, 400 mTorr, SiH_4 100 sccm, GeH_4 70 sccm, B_2H_6/H_2 60 sccm) and a 0.7 μm-thick poly-SiGe film (fabrication conditions: 425°C, 600 mTorr, SiH_4 100 sccm, GeH_4 58 sccm, B_2H_6/H_2 60 sccm). Owing to laboratory schedules, these two films were deposited two months after the DOE. During the intervening period, the LPCVD furnace underwent a change in setup to improve the uniformity of *in-situ* doping. Therefore, the properties of the depositions may differ somewhat when compared to properties obtained on runs that were part of the DOE.

The 2 μm film (450°C, 400 mTorr) has a tensile residual stress (36 MPa) and a strain gradient of 1×10^{-4} μm^{-1}, equivalent to a radius-of-curvature of 10 mm (Figure 2.8(a)). The 0.7 μm film (425°C, 600mTorr) has a compressive residual stress (-15 MPa) and a strain gradient of 2×10^{-4} μm^{-1}, equivalent to a radius-of-curvature of 5 mm (Figure 2.8(b)). The values of residual stress and strain gradients were measured using the methods discussed in the previous section (Section 2.2).

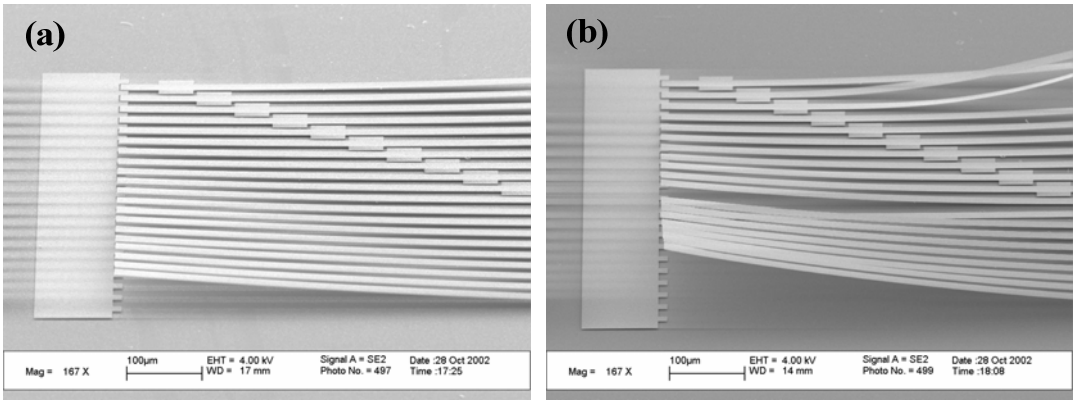

Figure 2.8**:** SEM pictures showing two poly-SiGe cantilever arrays deposited using different fabrication recipes. (a): A 2 µm-thick poly-SiGe array deposited at 450°C, 400 mTorr. (b): A 0.7 µm-thick poly-SiGe array deposited at 425°C, 600mTorr. Residual stress and strain gradient: 36 MPa, 1×10^{-4} μm^{-1} and -15 MPa, 2×10^{-4} μm^{-1}, respectively.

The strain gradients (which lead to the observed cantilever curvatures) are the result of stress gradients in the film, which arise during the polycrystalline grain growth step [17]. At the beginning of a deposition, SiGe compounds nucleate and form closely spaced fine grains on the surface. After nucleation, the grains start to grow in both vertical and lateral directions. The lateral growth causes the grains to compete with each other for room. Some of the grains eventually lose the competition and become overgrown by neighbors. The surviving grains therefore widen as they grow vertically, developing into conical grain structures. The conical structures display triangular patterns in the cross section, as seen in Figure 2.9.

Because there are more grains competing for room at the beginning of the deposition, the lower portion of the film is more compressively stressed. By convention, a "positive stress gradient" means that the stress is more compressive (or less tensile) in the lower portion of the film and becomes less compressive (or more tensile) towards the upper surface. The positive stress gradient in poly-SiGe causes the cantilevers to curve up, as seen in Figure 2.8.

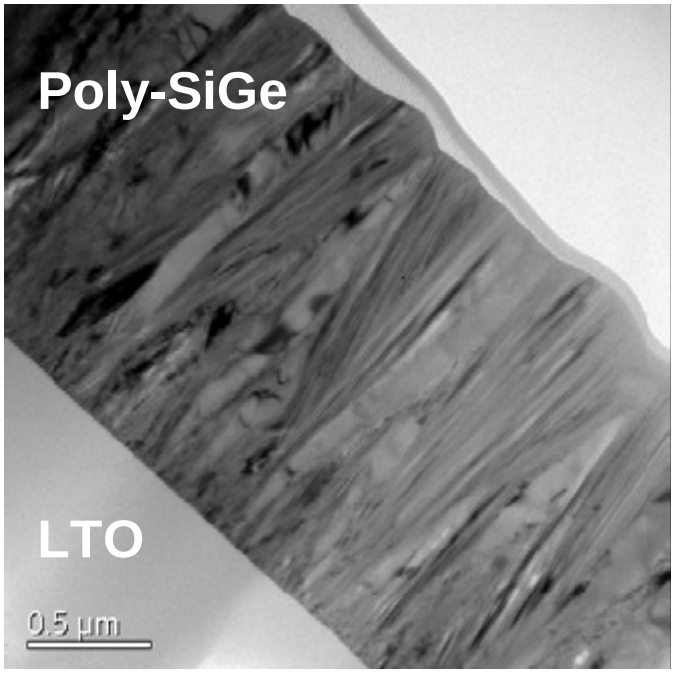

Figure 2.9: A TEM photo showing the cross section of a poly-SiGe film. The triangular patterns seen in the cross section are themselves cross sections of the conical structures that grow from the first-deposition sites. Image credit: C. W. Low [17].

In the following section, we present a mathematical model that relates the curvature of the cantilevers to the stress gradient in the film. The model is used to predict the curvature (effective strain gradient) of a bilayer structure.

2.4 Mathematical Model for a Bilayer Structure

The mathematical model is based on the following assumptions. We discuss errors caused by the assumptions in Section 2.5.

First, we assume that the stress gradient in a poly-SiGe layer is linear. This assumption is a first-order approximation. Research at our laboratory reported that the stress gradient in poly-SiGe is polynomial, and the derivative of the stress gradient is greater in the lower portion of the film, decreasing in the direction of the free surface [17-18]. At this time, however, a universal polynomial function has not been derived that can be used to model the nonlinear stress gradients in films deposited over a range of conditions.

Second, we assume that the residual stress and stress gradient in the top layer is not affected by the surface on which it is deposited. We also assume that the residual stress and stress gradient in the bottom layer remains unchanged after the deposition of the top layer.

Third, in this model, we assume an estimated Young's modulus of 150 GPa for poly-SiGe films with Ge contents between 50% and 70%. As discussed in Chapter 1, the range of Ge content between 50% and 70% is optimal for post-CMOS integration of MEMS because the films become amorphous for Ge contents

below 50% (when deposited below 450°C) and the etch resistance to H_2O_2 becomes lower for Ge contents above 70%. Therefore, in this thesis research, all the deposition conditions for poly-SiGe films were selected with the goal of obtaining Ge contents between 50% and 70%. The Young's modulus of polysilicon and polycrystalline-germanium (poly-Ge) are approximately 173 GPa and 132 GPa, respectively [7]. Using interpolation, we estimate that the Young's modulus of poly-SiGe films with Ge contents between 50% and 70% is approximately 144 to 153 GPa. Therefore, in the following analysis, we assume an estimated Young's modulus of 150 GPa for poly-SiGe films.

Based on the "linear-stress-gradient" assumption, we model the stress gradient by multiplying the strain gradient (measured from the cantilevers) by the Young's modulus of the film. Equation 2.1 is the mathematical form of the stress-thickness relationship in a monolayer poly-SiGe film.

$$\sigma(y) = \bar{\sigma} + E\delta_{\varepsilon}\left(y - \frac{d}{2}\right) \qquad 2.1$$

where

y is the distance from the bottom of the film.

$\sigma(y)$ is the residual stress of poly-SiGe at y.

$\bar{\sigma}$ is the average residual stress of the film. Based on the linear-stress-gradient assumption, we use the measured residual stress for this term.

E is the Young's modulus of the film.

δ_ε is the strain gradient, which is derived using Equation 1.1 and the measured deflections of the cantilevers.

d is the thickness of the film.

From the stress-thickness relationship, we calculate the moment generated by the stress in Equation 2.2.

$$M = \int_0^d \left(\sigma(y) - \bar{\sigma}\right)\ w\ \left(y - \frac{d}{2}\right)\ dy \qquad 2.2$$

where

M is the moment generated by the residual stress gradient

w is the width of the beam.

A nonzero moment causes the cantilevers to curve. In a monolayer poly-SiGe, the moment is positive, which causes the cantilevers to curve up.

Using Equation 2.3, we calculate the strain gradient (δ_ε) from the moment experienced by the cantilever.

$$\delta_\varepsilon = \frac{M}{E\frac{d^3 w}{12}} = \frac{12}{Ed^3}\frac{M}{w} = \frac{12}{Ed^3}\int_0^d \left(\sigma(y) - \bar{\sigma}\right)\ \left(y - \frac{d}{2}\right)dy \qquad 2.3$$

Figure 2.10 is a plot of the stress-thickness relationship of the 2 μm poly-SiGe layer (Measured residual stress and strain gradient: 36 MPa and 1×10^{-4} μm^{-1}). The straight line represents a linear stress gradient. Equation 2.4 is a numerical representation for the straight line representing the data in Fig. 2.10.

$$\sigma(y) = 36 + 15 \times (y - 1) \qquad 2.4$$

The variables $\sigma(y)$ and y in Equation 2.4 are in dimensions of MPa and μm, respectively.

Using Equation 2.2, we calculate the moment-per-unit-beam-width (*M/w*) of the film to be 10 μN. A 10 μN moment-per-unit-beam-width (*M/w*) means that the moment applying on a 10-μm-wide cantilever is 10 μN × 10 μm = 10^{-4} μNm). Using Equation 2.3, we calculate the strain gradient caused by this moment to be $1\times10^{-4}\mu m^{-1}$.

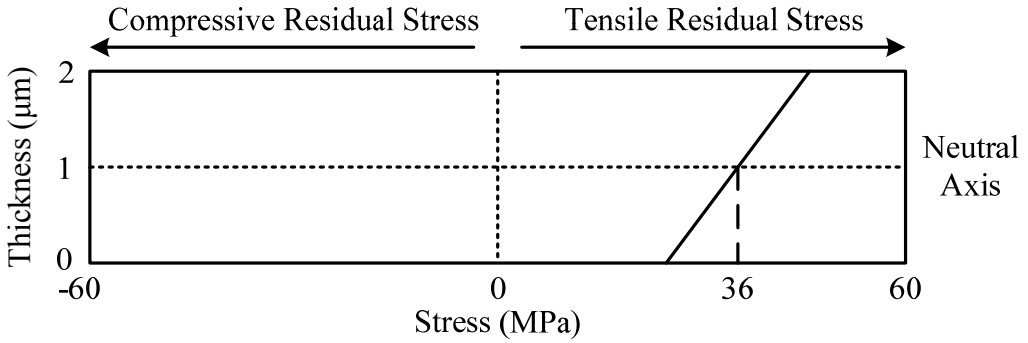

Figure 2.10: The stress-thickness relationship of the 2 μm poly-SiGe layer (Measured residual stress and strain gradient: 36 MPa and 1×10^{-4} μm^{-1}). The straight line represents a linear stress gradient.

Figure 2.11 is a plot of the stress-thickness relationship of a 2.16 μm bilayer poly-SiGe. For the 2 μm bottom layer, the stress-thickness relationship is the same as in Figure 2.10. For the 0.16μm bottom layer, we plot the initial 0.16μm of the stress-thickness relationship of the 0.7μm poly-SiGe shown in Figure 2.8(b) (Measured residual stress and strain gradient: -15 MPa and $2\times10^{-4}\mu m^{-1}$). As seen in Figure 2.11, in the case of a bilayer structure, there is a discontinuity in the stress-thickness relationship, located at the interface of the two layers. The -25.5 MPa stress at the bottom surface of the top layer is extrapolated from the measured residual stress of the 0.7μm poly-SiGe (-15 MPa) using a linear stress gradient of 30 MPa-μm^{-1} (-15 MPa – 30 MPa-μm^{-1} × 0.35μm = -25.5 MPa). The 30 MPa-μm^{-1}

stress gradient is derived by multiplying the $2\times10^{-4}\mu m^{-1}$ strain gradient by a Young's Modulus of 150 GPa.

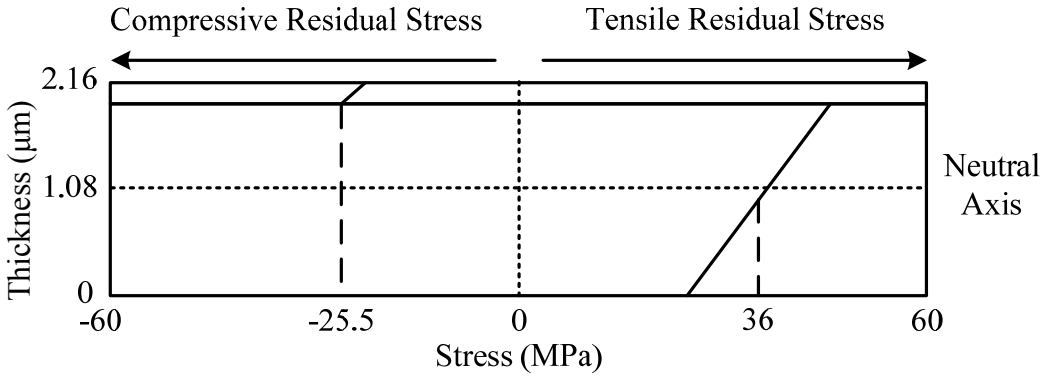

2 μm bottom layer + 0.16 μm top layer
Moment per unit beam width = + 0.55 μN
Positive moment ➔ Cantilevers curve up
Effective strain gradient: $+ 4.4\times10^{-6}$ /μm (or radius-of-curvature: 227 mm)

Figure 2.11: The stress-thickness relationship of a 2.16 μm bilayer poly-SiGe.

Equation 2.5 is the mathematical form that illustrates the stress-thickness relationship of a bilayer film. The subscripts *b* and *t* represent bottom and top layers, respectively.

$$\sigma(y)=\begin{cases}\overline{\sigma}_b+E_b\delta_{\varepsilon b}\left(y-\dfrac{d_b}{2}\right) & for \quad 0\le y\le d_b\\ \overline{\sigma}_t+E_t\delta_{\varepsilon t}\left(y-\left(d_b+\dfrac{d_t}{2}\right)\right) & for \quad d_b\le y\le d_b+d_t\end{cases} \qquad 2.5$$

After the addition of a top layer, the film thickness becomes d_b+d_t and the neutral axis of the film is shifted to $(d_b+d_t)/2$. The average residual stress and the effective Young's modulus of the film become

$$\overline{\sigma} = \frac{\int_0^{d_b+d_t} \sigma(y)dy}{d_b + d_t} \tag{2.6}$$

$$E = \frac{E_b d_b + E_t d_t}{d_b + d_t} \tag{2.7}$$

The purpose of deriving the average residual stress and the effective Young's modulus is that we need these values to calculate the total moment experienced by the bilayer film and the resulting curvature of the film.

By inserting the averaged residual stress (Equation 2.6) and the shifted neutral axis into Equation 2.2 and 2.3, we derive equations 2.8 and 2.9.

$$M = \int_0^d \left(\sigma(y) - \frac{\int_0^{d_b+d_t} \sigma(y)dy}{d_b + d_t} \right) w\left(y - \frac{d_b + d_t}{2} \right) dy \tag{2.8}$$

$$\delta_\varepsilon = \frac{12}{E(d_b + d_t)^3} \frac{M}{w} \tag{2.9}$$

Figure 2.11 also shows the moment-per-unit-beam-width and the predicted "effective strain gradient" calculated using Equation 2.5-2.9.

In Figure 2.12, we increase the thickness of the top layer to 0.2 μm. The calculated moment-per-unit-beam-width and the predicted "effective strain gradient" are shown in the figure.

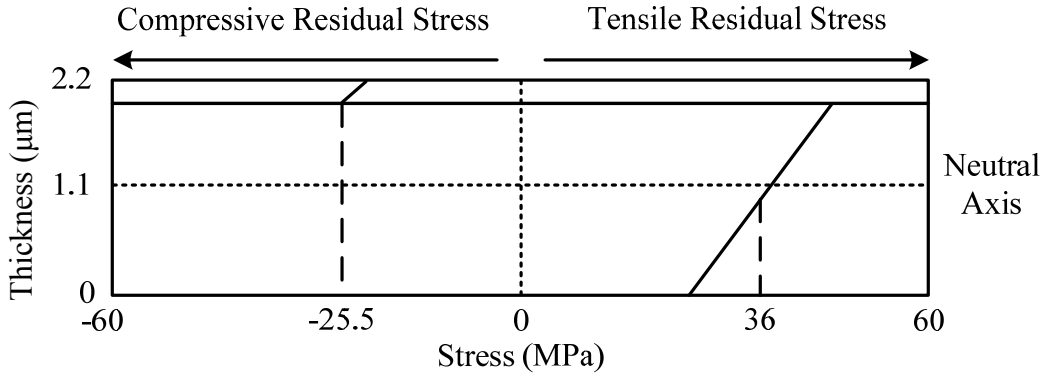

Figure 2.12: The stress-thickness relationship of a 2.2 μm bilayer poly-SiGe.

In our model, when a 0.16 μm poly-SiGe top layer is added to the 2 μm bottom layer, the more compressive stress in the top layer shifts the average stress of the bilayer film, and also creates a negative moment about the new neutral axis (1.08 μm from the bottom of the bottom layer, because the total film thickness becomes 2.16 μm). The moment-per-unit-beam-width is reduced (from +10 μN to +0.55 μN). The predicted effective strain gradient of the bilayer is $4.4\times10^{-6}\mu m^{-1}$, equivalent to a 227 mm radius-of-curvature.

When the thickness of the top layer is increased to 0.2 μm, the moment-per–unit-beam-width becomes -1.68 μN, translating to a down-curving cantilever. The predicted effective strain gradient is $-1.3\times10^{-5}\mu m^{-1}$.

2.5 Sources of Error in the Mathematical Model

There are several sources of error in our model. First, the assumption of linear stress gradient is a first-order approximation. As a result, extensive extrapolation from a layer's neutral axis is likely to result in inaccurate estimation of stress. Errors from the estimation of Young's modulus and the measurements of residual stress and strain gradient could exacerbate the inaccuracy. Second, the residual stress and strain gradient of the top layer could vary when it is deposited on different types of surface.

2.6 Experimental Results for Bilayer Poly-SiGe Cantilevers

Using the model as a guide, we conducted experiment to demonstrate the effect of using bilayer structures for cantilevers. In the experiment, we took 3 unpatterned wafers from the batch that produced the 2μm poly-SiGe shown in Figure 2.8(a), cleaned the surface in 100:1 HF to remove native oxide, and then ran three depositions (one for each wafer) to deposited three different thicknesses (0.1, 0.15, and 0.3 μm) of poly-SiGe as the top layer. The recipe for the top layer was the one that produced the 0.7μm poly-SiGe shown in Figure 2.8(b). After patterning

and sacrificial release, we measured the deflections of the bilayer cantilevers. The effective strain gradients of the bilayer films are derived using Equation 1.1 and the measured deflections.

In Figure 2.13, we plot the effective strain gradients of the bilayer films versus the corresponding thicknesses of the top layers. The strain gradient of the 2μm monolayer in Figure 2.8(a), which represents "zero thickness of top layer", is also plotted in Figure 2.13 to be compared with the bilayers. The theoretical curve (labeled as "Model Prediction") plotted in Figure 2.13 is derived using Equations 2.8-2.9 and the measured values of residual stress- and strain-gradients of the individual layers shown in Figure 2.8(a, b). The mathematical steps to derive this curve are the same as those used in Section 2.4 to derive the predicted effective strain gradients in Figures 2.10-2.12.

The theoretical curve in Figure 2.13 is nonlinear. This is due to the fact that the residual stress of the top layer itself becomes more tensile as it grows thicker. Hence, the down-bending moment generated from the difference in residual stress between the two layers has a decreasing effect.

As shown in Figure 2.13, the experimental results show that the bilayer films exhibit less curvature (lower effective strain gradient) with the additions of top layers.

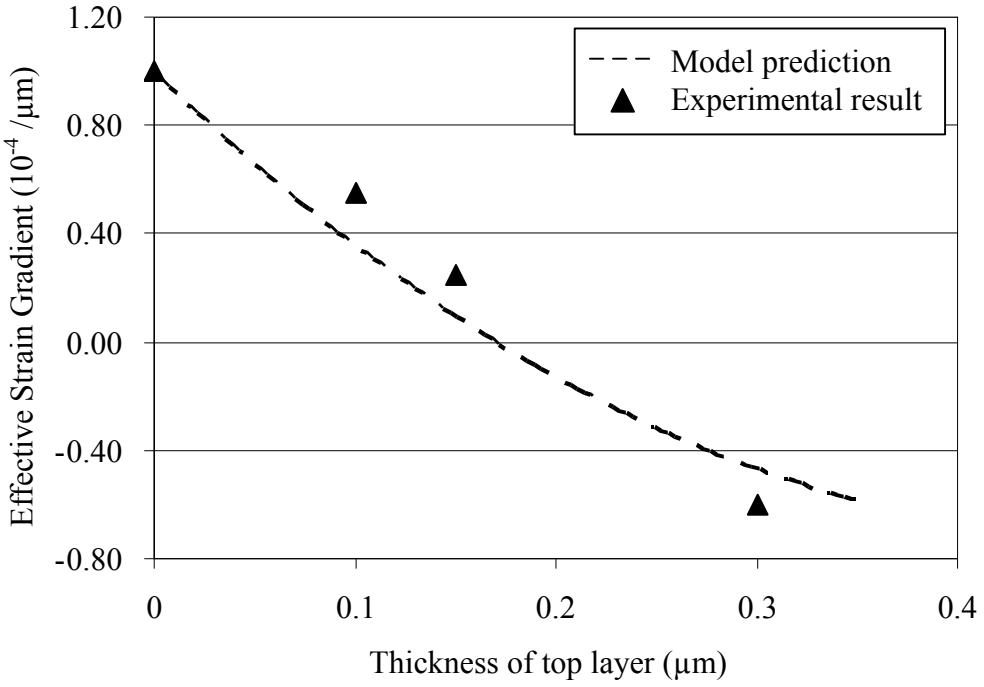

Figure 2.13: Experimental results of adding different thicknesses of top layer to a 2 μm bottom layer. A cantilever array made of the bottom layer only is shown in Figure 2.8(a).

Figure 2.14 shows the SEM photo of the 2.15 μm-thick bilayer cantilevers. The effective strain gradient of this film was derived to be 3×10^{-5} μm^{-1}.

Figure 2.15 shows the 2.3 μm bilayer cantilevers. Because the negative moment generated from the bilayer structure is greater than the positive moment caused by the grain structures, the cantilevers curve down. As seen in Figure 2.15, the free end of the 1 mm cantilever curves down sufficiently to touch the substrate. To derive the effective strain gradient of this bilayer film, we measured the deflections of the shorter cantilevers that do not touch the substrate. The downward

deflection of the 200 μm-long cantilever is 1.2 μm. Using Equation 1.1, the effective strain gradient is derived to be -6×10^{-5} μm^{-1}.

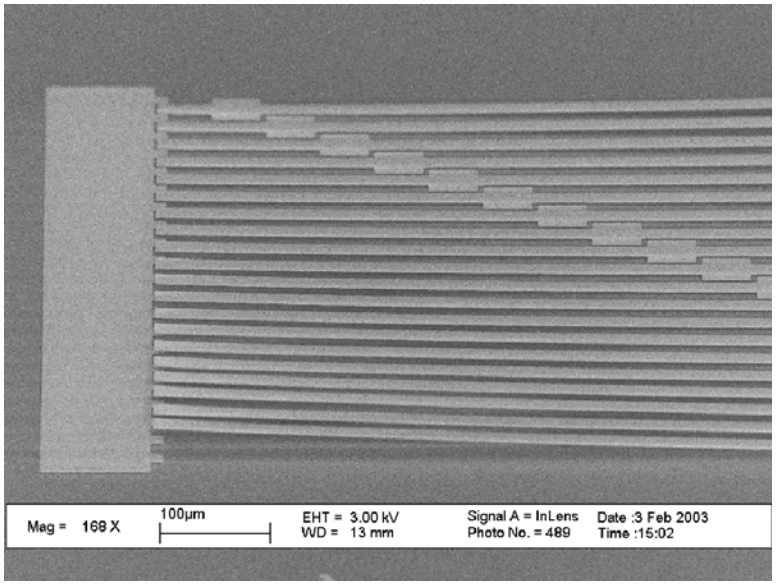

Figure 2.14: The SEM photo of the 2.15 μm-thick bilayer cantilevers. The effective strain gradient derived using Equation 1.1 and measured deflections is 3×10^{-5} μm^{-1}.

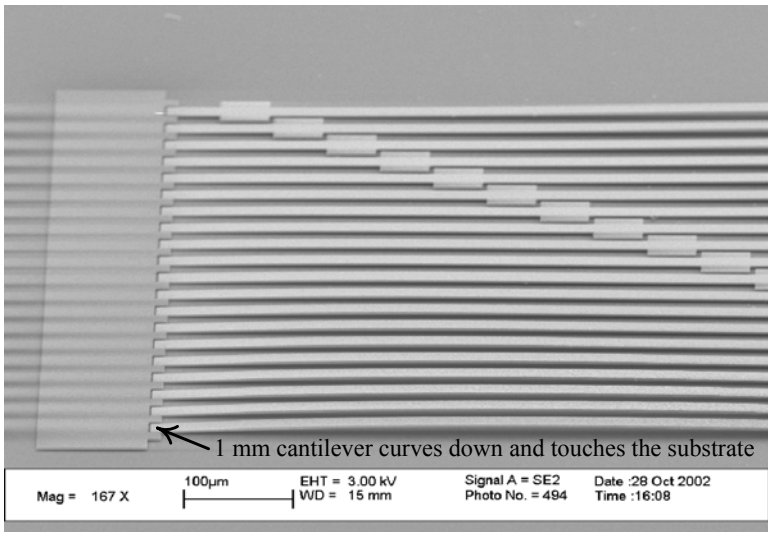

Figure 2.15: The SEM photo of the 2.3 µm-thick bilayer cantilevers. The cantilevers curve down sufficiently that some (longer beams) touch the substrate. The effective strain gradient of this film is -6×10^{-5} μm^{-1}, which is derived using Equation 1.1 and the deflections of the shorter beams that do not touch the substrate.

A joint project carried out in collaboration with Analog Devices, Inc. was established in 2003 to develop a 4 µm bilayer poly-SiGe process for modular integration of MEMS accelerometers. After a series of process development steps, the project led to fabrication of a 3.9 µm bilayer with a strain gradient of 1.1×10^{-5} μm^{-1} (equivalent to 88 mm radius-of-curvature). Beams from this fabrication run are shown in Figures 2.16(c) and 2.16(d). The bilayer consists of a 3.7 µm film on the bottom (deposited at 425°C, 400mTorr) which is overlain by a 0.2 µm top layer (425°C, 600mTorr). Without the 0.2 µm top layer, the 3.7 µm bottom layer

(Figures 2.16(a) and 2.16(b)) exhibits a strain gradient of 6×10^{-5} μm^{-1}. Using the analysis steps given above, the residual stress of the bilayer is found to be -36 MPa, and the resistivity is 0.55 mΩ-cm. The thermal budget to deposit the bilayer totals approximately 10 hours at 425°C.

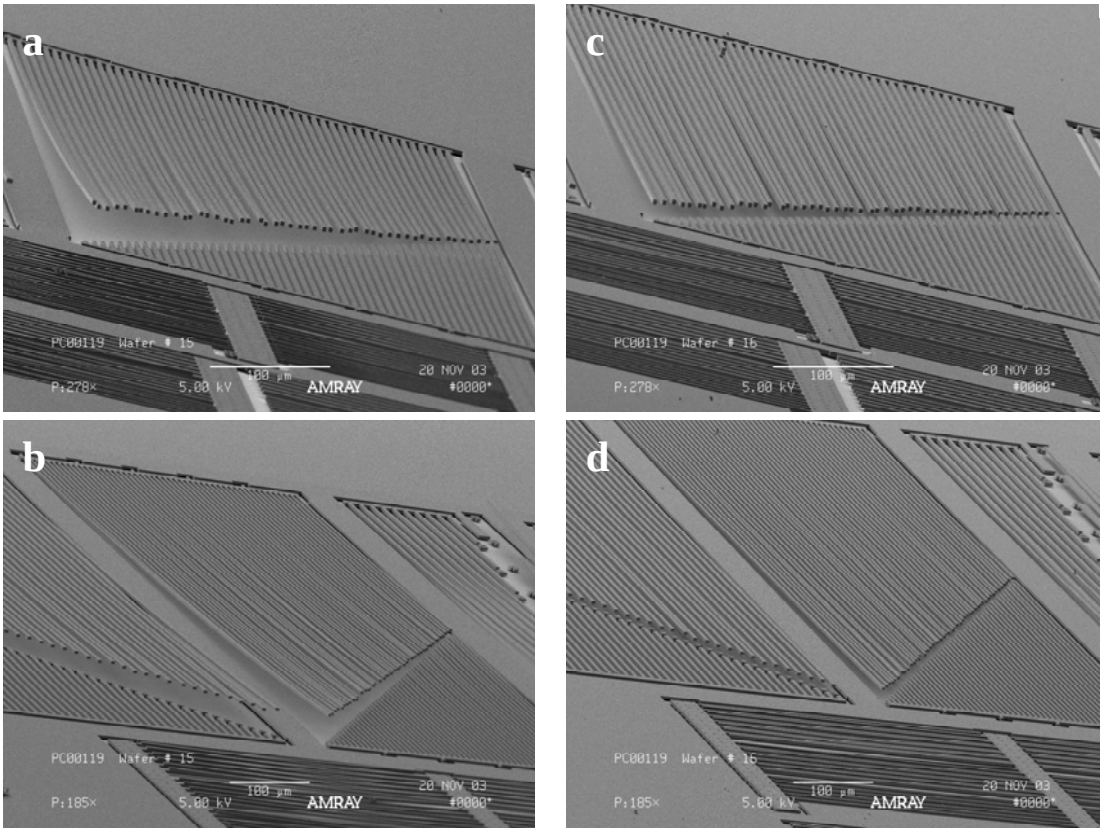

Figure 2.16: Cantilever arrays made of 3.7 μm monolayer poly-SiGe (a, b) and 3.9 μm bilayer poly-SiGe (c, d).

2.7 Conclusion

In this chapter, we describe analysis and experiments that we have carried out on poly-SiGe bilayer cantilevers that we have developed to reduce their curvature. Our best result was to produce cantilevers showing a effective strain gradient of 1.1×10^{-5} μm^{-1}, equivalent to a radius of curvature of 88 mm. This strain gradient was the lowest ever achieved for as-deposited (no post-deposition annealing) poly-SiGe cantilevers of similar dimensions at the time our experimental results were published in 2003 [10]. At that time, as-deposited monolayer poly-SiGe cantilevers of similar dimensions typically exhibit strain gradients greater than 1×10^{-4} μm^{-1}. In 2007, Low [17] discovered a deposition regime at 410°C where the poly-SiGe grains exhibit columnar structures, as opposed to the conical structures typically seen in LPCVD poly-SiGe films (Figure 2.9). The columnar structures result in a more uniform strain gradient across the film thickness. In Low [17], monolayer poly-SiGe cantilevers that exhibit a strain gradient of 1.1×10^{-6} μm^{-1} were demonstrated.

To make the MEMS deformable mirror array that is the goal of this thesis research, we need to produce not only beams to support and actuate the mirrors, but also flat platforms on which high-quality reflecting surfaces can be mounted. The flat platform serves also as the top electrode of an electrostatic parallel-plate actuator. Although our processing capability cannot make the platform truly "flat," it is possible to produce a platform with a very low strain gradient (large radius-of-curvature). In Chapter 4, we discuss fabrication of this platform using a bilayer poly-SiGe.

Chapter 3 : Flexural-Support Design to Increase Mirror Elevation

3.1 Utilization of the Residual Stress Gradient in Poly-SiGe to Increase Mirror Elevation

As shown in Figure 3.1, our MEMS deformable-mirror actuator has one platform and three flexural supports. In Chapter 2, we discuss the bi-layer structure that is used to build the platform. In this chapter, we discuss a “bi-width” flexural support design that utilizes the residual stress gradient in poly-SiGe to elevate the platform. Because the adaptive-optics applications require deformable mirrors with large strokes (i.e. 5 μm for astronomy and 10-20 μm for vision science), the electrostatic parallel-plate gap-closing actuator needs to have a gap commensurate with these dimensions between the top- and bottom-electrodes.

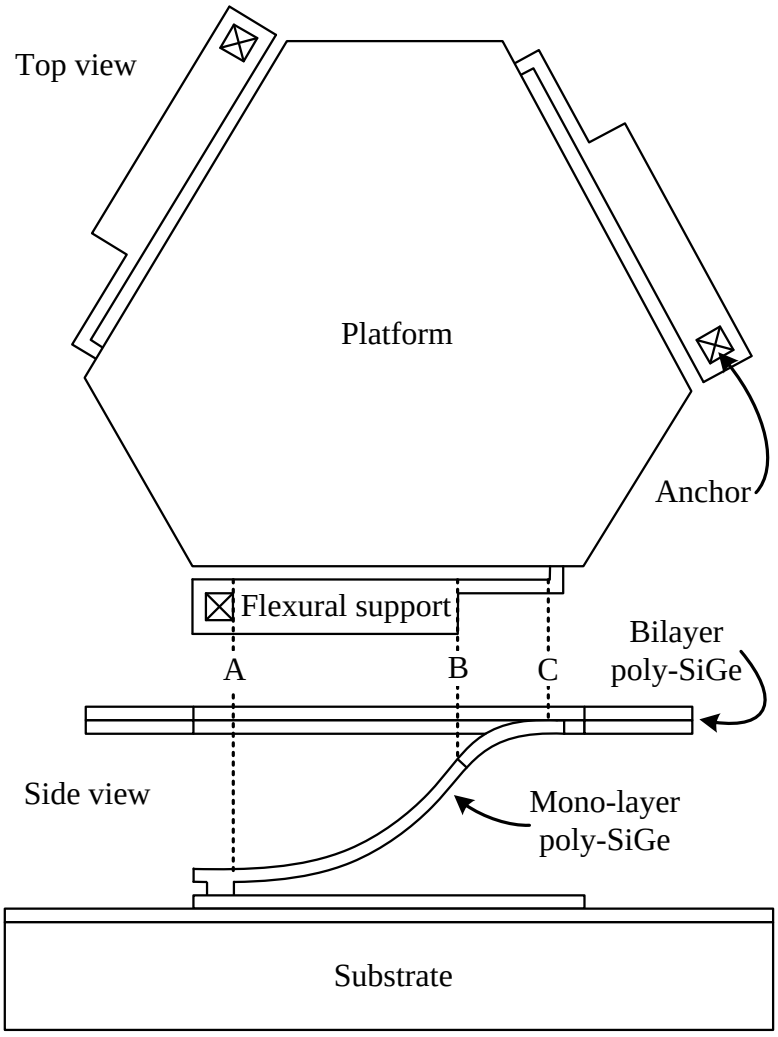

Figure 3.1: Schematics of the parallel-plate gap-closing deformable-mirror actuator.

As seen in Figure 3.1, the flexural supports are formed of one layer of poly-SiGe. The stress gradient in the poly-SiGe layer causes the flexural supports to curve. The platform, however, needs to be flat which is accomplished by two poly-SiGe layers deposited one on top of the other.

The curvature of the flexural support is determined by the residual moments in the beam. These moments include a positive (up-curving) component generated from the stress gradient in the poly-SiGe film, and a counter-moment that is applied at point C (in Figure 3.1) by the joint that connects the flexural support and the platform. The magnitude of the counter-moment is sensitive to the torsional stiffness of the joint. A joint that is infinitely stiff would not allow the flexural support to have any angular deflection at point C. In Section 3.3 of this chapter, we will derive a mathematical model that illustrates the relationship between the torsional spring constant of the joint and the deflection of the flexural support. The torsional spring constant of the joint is defined as the torque required to twist the joint through an angle of 1 radian. Thus, an infinitely stiff joint at the platform has a torsional spring constant of infinity.

As seen in Figure 3.1, the flexural support is designed to be wider between A and B than between B and C. As a result, the up-curving moment in the flexural support is greater in segment AB than in segment BC. In Section 3.2, we derive a mathematical model that illustrates how the deflection of the flexural support is increased in a controllable way using this “bi-width” design.

In Section 3.4, we describe a five-mask fabrication process that was used to demonstrate the “bi-width” flexural support design. The experimental results are then compared to theoretical predictions derived in Sections 3.2 and 3.3.

3.2 A Mathematical Model for the Flexural Support

Figure 3.2 is a sketch of a bi-width flexural support.

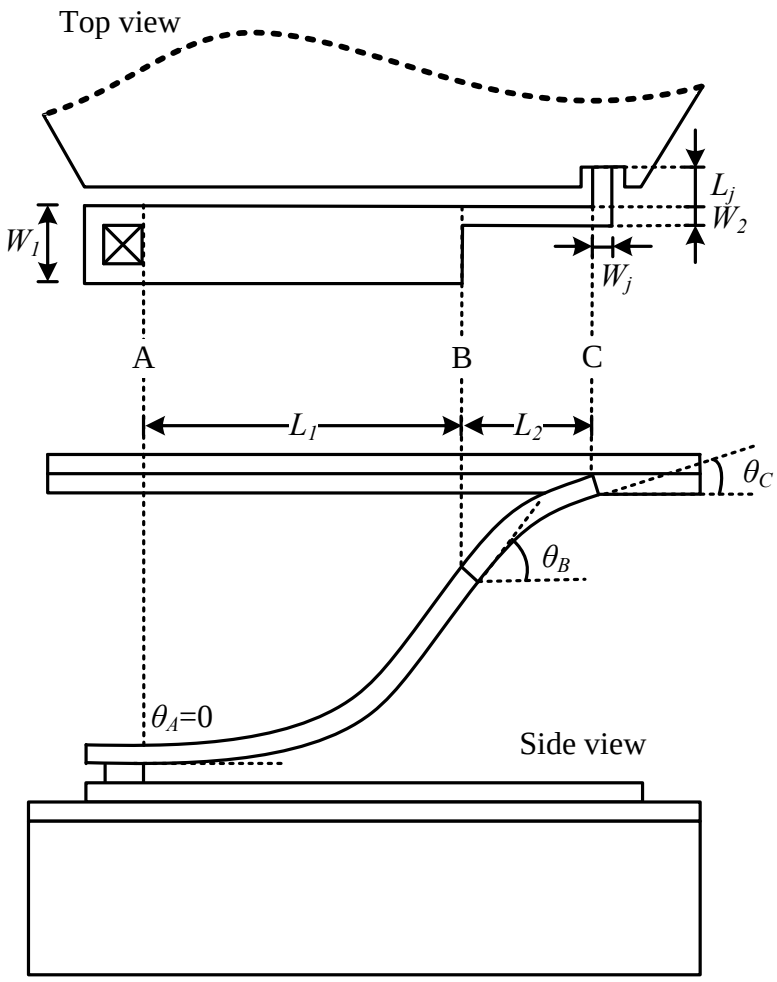

Figure 3.2: Sketch showing the top and side views of a bi-width flexural support.

First, we define a as the ratio between W_1 and W_2.

$$a = \frac{W_1}{W_2} \qquad 3.1$$

According to the mathematical model discussed in Chapter 2, the moment generated from the stress gradient is proportional to the width of the beam (see Equation 2.2).

$$M = \int_0^t \left(\sigma(y) - \bar{\sigma}\right) W \left(y - \frac{t}{2}\right) dy \qquad 2.2$$

where

M is the moment generated by the residual stress gradient

t is the thickness of the flexural support

y is the axis along the thickness of the flexural support

σ is the residual stress of the film

W is the width of the flexural support

Hence,

$$M_1 = aM_2 \qquad 3.2$$

where M_1 and M_2 are the up-curving moments generated from the stress gradients in segment AB and segment BC, respectively.

The moment-of-inertia of a beam is also proportional to its width: $I = t^3 W / 12$, where I, t, W are moment-of-inertia, thickness, and width of the beam, respectively) Therefore, we can write

$$I_1 = aI_2 \qquad 3.3$$

where I_1 and I_2 are the moments-of-inertia of segments AB and BC, respectively.

The counter-moment at point C, the joint between the flexural support and the platform is denoted by (M_j). This down-bending moment subtracts from the up-bending moments in the flexural support and results in net moments in the two beam sections having values of M_1-M_j and M_2-M_j in segments AB and BC, respectively.

Equation 3.4 defines the relationship between θ_B and θ_C (see Figure 3.2), the angular deflections in the flexural support at points B and C, respectively.

$$\theta_B = \frac{M_1 - M_j}{EI_1} L_1 = \frac{M_j - M_2}{EI_2} L_2 + \theta_C \qquad 3.4$$

where E is the Young's modulus of the poly-SiGe flexural support

It can be observed in Equation 3.4 that, in the case of a infinitely stiff joint ($\theta_C = 0$), the flexural support curves up ($\theta_B > 0$) only if $M_1 > M_j > M_2$.

Substituting Equation 3.1-3.3 into 3.4 and rearranging the variables, we obtain the expression of M_j as a function of a, L_1, L_2, and M_2.

$$M_j = \frac{a\frac{L_1}{L_2} + a}{a + \frac{L_1}{L_2}} M_2 - \frac{aEI_2}{L_1 + aL_2}\theta_C \qquad 3.5$$

It is observed in Equation 3.5 that, when $\theta_C = 0$ (infinitely stiff joint), $M_j > M_2$ only if $a > 1$, meaning that when the joint is infinitely stiff, the flexural support curves up only if $W_1 > W_2$.

The mirror elevation of the flexural support (y_C) is equal to the sum of the elevations contributed by the two segments.

$$y_C = y_{AB} + y_{BC} = \frac{M_1 - M_j}{2EI_1} L_1^{\,2} + \frac{M_j - M_2}{2EI_2} L_2^{\,2} + L_2\theta_C \qquad 3.6$$

where

y_C is the mirror elevation, which is equivalent to the vertical deflection between point A and point C (see Figure 3.1).

y_{AB} is the vertical deflection between point A and point B, which is equal to $\frac{M_1 - M_j}{2EI_1} L_1^{\,2}$

y_{BC} is the vertical deflection between point B and point C, which is equal to $\frac{M_j - M_2}{2EI_2} L_2^{\,2} + L_2\theta_C$

Substituting Equations 3.2 to 3.5 into Equation 3.6, we derive another expression for y_C.

$$y_C = \frac{M_2}{2EI_2}\left(\frac{a-1}{a+\frac{L_1}{L_2}}\right)L_1(L_1+L_2)+\left(\frac{\frac{L_1^{\,2}}{L_2}-aL_2}{2\left(a+\frac{L_1}{L_2}\right)}+L_2\right)\theta_C \qquad 3.7$$

The length of the flexural support, denoted by "*L*" (see Figure 3.2), is equal to the sum of the lengths of the two segments ($L = L_1 + L_2$). We define a variable p ($0 \le p \le 1$) as the ratio of L_1 to L. Equations 3.8 through 3.10 illustrate the relationships between L, L_1, L_2, and p.

$$L = L_1 + L_2 \qquad 3.8$$

$$L_1 = pL \qquad 3.9$$

$$L_2 = (1-p)L \qquad 3.10$$

Substituting Equations 3.8-3.10 into Equation 3.7, we derive an expression for y_C as a function of M_2, E, I_2, L, a, p, and θ_C.

$$y_C = \frac{M_2}{2EI_2}L^2\left(\frac{(a-1)p(1-p)}{a-(a-1)p}\right)+\left(\frac{(a-1)p^2-2(a-1)p+a}{a-(a-1)p}\right)\frac{L}{2}\theta_C \qquad 3.11$$

It is observed in Equation 3.11 that the mirror elevation consists of two terms. The first term is a function of the properties of the material that forms the flexural support, including the stress gradient, Young's modulus, and thickness of the poly-SiGe. The second term is a function of θ_C, the angular deflection at point C allowed by the joint connecting the flexural support and the platform.

If the joint is infinitely stiff, no angular deflection is allowed at point C ($\theta_C = 0$), and the second term of Equation 3.11 is zero. In this case, the mirror elevation is determined by the properties of poly-SiGe and the proportions (*a* and *p*) of the flexural support. However, if the flexural support has one uniform width between point A and point C (*a=1* or *p=0 or 1*), the first term of Equation 3.11 also becomes zero, indicating that the elevation of the mirror is zero.

If the joint is infinitely compliant (torsional spring constant = 0), there would be no counter-moment applied by the joint at point C. In this case, the flexural support would curve as if it is not attached to anything, and both the angular deflection at point C and the mirror elevation would be at their maximum values. We define these values as $\theta_{C\max}$ and $y_{C\max}$, and derive them in the following equations.

$$\theta_{C\max} = \frac{M_1}{EI_1}L_1 + \frac{M_2}{EI_2}L_2 = \frac{M_2}{EI_2}(L_1 + L_2) = \frac{M_2}{EI_2}L \qquad 3.12$$

$$y_{C\max} = \frac{M_2}{2EI_2}L^2\left(\frac{(a-1)p(1-p)}{a-(a-1)p}\right)+\left(\frac{(a-1)p^2-2(a-1)p+a}{a-(a-1)p}\right)\frac{L}{2}\theta_{C\max}$$
$$= \frac{M_2}{2EI_2}L^2 = \frac{L}{2}\theta_{c\max}$$

3.13

Experimentally we observe (as is expected) that $\theta_{C\max}$ and $y_{C\max}$ as derived in Equations 3.12-3.13 are equivalent to the angular deflection and vertical deflection at the free end of a cantilever that is made of the same poly-SiGe and has a length *L*. In other words, if the joint is infinitely compliant, the curvature of the flexural support is the same as a cantilever of the same length, regardless of the proportions of the flexural support (since neither *a* nor *p* appears in the equations for $\theta_{C\max}$ and $y_{C\max}$).

In reality, the joint is neither infinitely stiff nor infinitely compliant. The angular deflection at point C (θ_C) is between zero and $\theta_{C\max}$ ($0 < \theta_C < \theta_{C\max}$), and is determined by the equilibrium between the up-curving moment generated from the stress gradient and the torsional spring constant of the joint (discussed in more detail in Section 3.3). Depending on the proportions (*a* and *p*) of the flexural support, the mirror elevation can be derived using Equation 3.11. A special case occurs when the flexural support has a uniform width between point A and point C (*a=1* or *p=0 or 1*). Using Equation 3.11, we derive the mirror elevation of a uniform-width flexural support in Equation 3.14.

$$y_{C\_uniform-width} = \frac{L}{2}\theta_C \qquad 3.14$$

The elevation is equal to the vertical deflection at the free end of a cantilever that has a length L and an angular deflection of θ_C, as expected.

3.3 Flexural Support Design Considerations

To further understand the effects of (1) the proportions (a and p) of the flexural support and (2) the stiffness of the joint on the mirror elevation, we substitute Equations 3.13 and 3.14 into Equation 3.11 to obtain an expression for y_C (Equation 3.15) as a function of $y_{C\max}$, $y_{C\_uniform-width}$, and the proportions (a and p).

$$\begin{aligned} y_C &= \frac{M_2}{2EI_2}L^2\left(\frac{(a-1)p(1-p)}{a-(a-1)p}\right)+\left(\frac{(a-1)p^2-2(a-1)p+a}{a-(a-1)p}\right)\frac{L}{2}\theta_C \\ &= y_{C\max}\left(\frac{(a-1)p(1-p)}{a-(a-1)p}\right)+y_{C\_uniform-width}\left(\frac{(a-1)p^2-2(a-1)p+a}{a-(a-1)p}\right) \end{aligned} \qquad 3.15$$

Dividing y_C by $y_{C\max}$, we obtain an expression for $y_C/y_{C\max}$ in Equation 3.16. The term ($y_C/y_{C\max}$) is defined as the normalized mirror elevation, which is

the mirror elevation of a flexural support divided by the vertical deflection of the same flexural support if it is not attached to anything.

$$\frac{y_C}{y_{C\max}} = \left(\frac{(a-1)p(1-p)}{a-(a-1)p} \right) + \frac{y_{C\_uniform-width}}{y_{C\max}} \left(\frac{(a-1)p^2 - 2(a-1)p + a}{a-(a-1)p} \right) \qquad 3.16$$

The purpose of normalizing the mirror elevation is to remove the material-dependent factors (i.e. the stress gradient and Young's modulus of poly-SiGe) and the actual dimensions (i.e. the actual width, length, and thickness of the flexural support) from the equation so that we can focus on the effects of the geometrical proportions.

The term ($y_{C\_uniform-width} / y_{C\max}$) on the right side of Equation 3.16 is the mirror elevation of a uniform-width flexural support normalized by the vertical deflection of the same flexural support acting as a cantilever, i.e. as if it were not attached to anything. Using the expressions for $y_{C\_uniform-width}$ and $y_{C\max}$ in Equations 3.13 and 3.14, respectively, we derive that $y_{C\_uniform-width} / y_{C\max}$ is equal to $\theta_C / \theta_{C\max}$, as shown in Equation 3.17.

$$\frac{y_{C\_uniform-width}}{y_{C\max}} = \frac{\frac{L}{2}\theta_C}{\frac{L}{2}\theta_{C\max}} = \frac{\theta_C}{\theta_{C\max}} \qquad 3.17$$

Substituting Equation 3.17 into Equation 3.16, we obtain Equation 3.18, which shows the relationship between the normalized mirror elevation ($y_C / y_{C\max}$) and p (=$L_1/(L_1+L_2)$), a (=W_1/W_2), and $\theta_C / \theta_{C\max}$.

$$\frac{y_C}{y_{C\max}} = \left(\frac{(a-1)p(1-p)}{a-(a-1)p} \right) + \frac{\theta_C}{\theta_{C\max}} \left(\frac{(a-1)p^2 - 2(a-1)p + a}{a-(a-1)p} \right) \qquad 3.18$$

Using Equation 3.18, we plot the normalized mirror elevation ($y_C / y_{C\max}$) versus p (=$L_1/(L_1+L_2)$) with two parameters, a (=W_1/W_2) and $\theta_C / \theta_{C\max}$, in Figures 3.3 and 3.4. The curves in the two figures are derived by substituting different values of a (=W_1/W_2) and $\theta_C / \theta_{C\max}$ into Equation 3.18. In Figure 3.3, the value of $\theta_C / \theta_{C\max}$ is fixed at 0 (assuming an infinitely stiff joint) to show the effect of a (=W_1/W_2). In Figure 3.4, the value of a (=W_1/W_2) is fixed at 4 in order to show the effect of $\theta_C / \theta_{C\max}$.

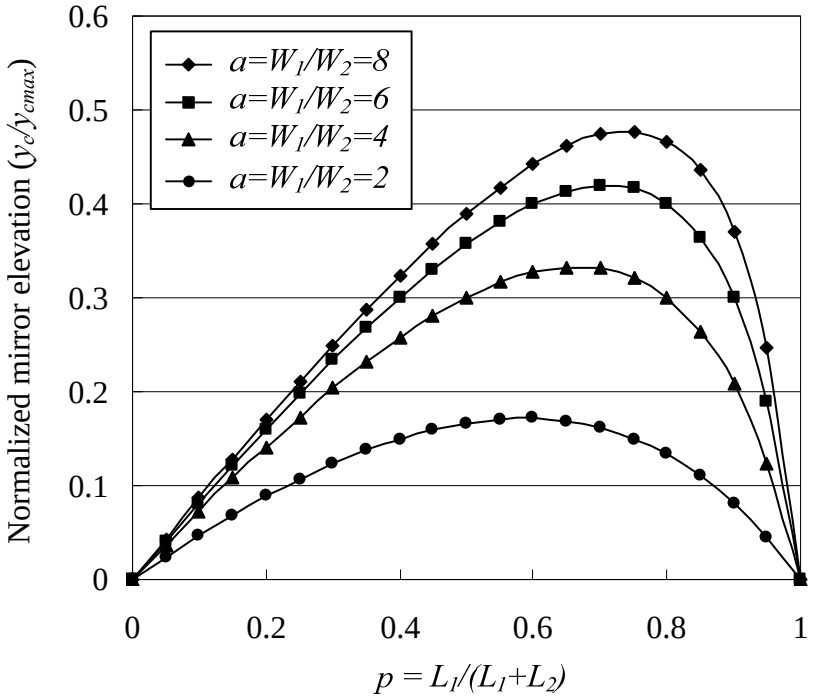

Figure 3.3: A plot of the normalized mirror elevation ($y_C / y_{C\max}$) versus p ($=L_1/(L_1+L_2)$) with $\theta_C / \theta_{C\max}$ =0 and $a=W_1/W_2$= 2, 4, 6 and 8. The curves are derived using Equation 3.18.

It is observed in Figure 3.3 that the normalized mirror elevation increases with the width ratio a ($=W_1/W_2$). The incremental increase becomes less, however, as the ratio a ($=W_1/W_2$) becomes larger. In addition, for each value of W_1/W_2, there exists an optimal proportion (p) between the lengths of the wide and narrow segments, at which the mirror elevation is maximized. For example, in the case of $a=W_1/W_2$=4, the highest normalized mirror elevation is 0.33, which occurs at $p=L_1/(L_1+L_2)$=0.67.

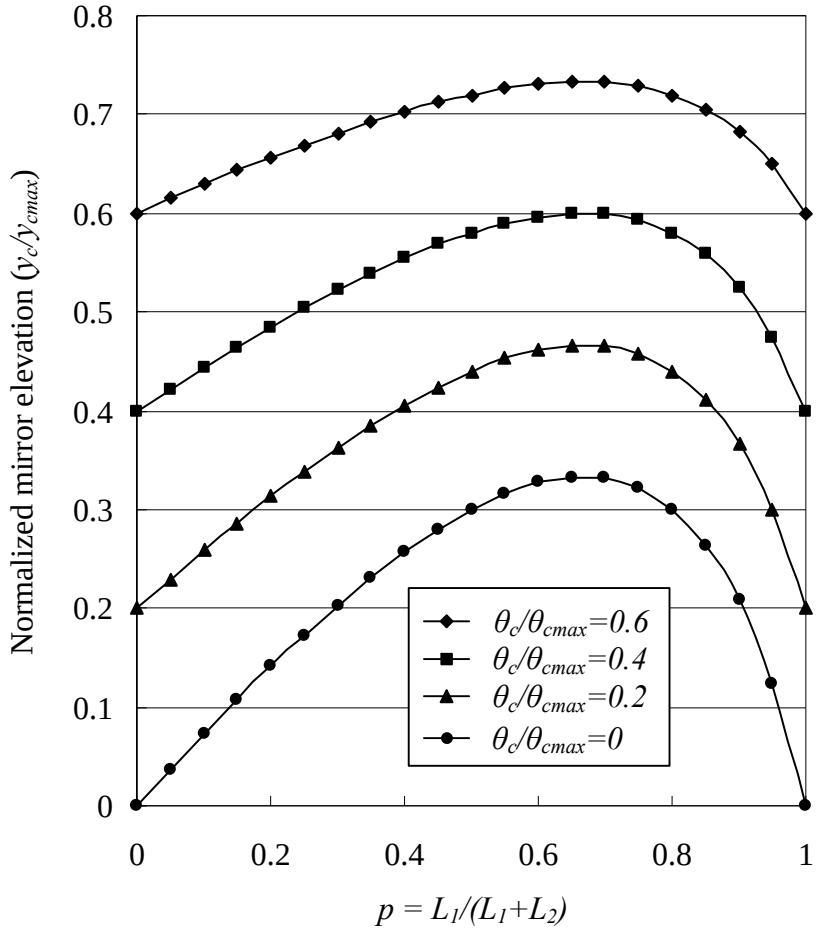

Figure 3.4: A plot of the normalized mirror elevation ($y_C/y_{C\max}$) versus p (=$L_1/(L_1+L_2)$) with $a=W_1/W_2$= 4 and $\theta_C/\theta_{C\max}$ =0, 0.2, 0.4, 0.6, and 0.8. The curves are derived using Equation 3.18.

As seen in Figure 3.4, the normalized mirror elevation increases with $\theta_C/\theta_{C\max}$. For any value of $\theta_C/\theta_{C\max}$, the lowest normalized mirror elevation

occurs when a uniform-width flexural support is used. Within each level of $\theta_C/\theta_{C\max}$ (each curve in Figure 3.4), there also exists an optimal proportion (p) between the lengths of the wide and narrow segments, at which the mirror elevation is maximized.

Although, according to the analysis, the mirror elevation increases with both a ($=W_1/W_2$) and $\theta_C/\theta_{C\max}$, there are practical considerations that limit the highest value for each parameter that we can use (or achieve) in the flexural support design. The following paragraphs discuss these practical considerations further.

For the width ratio a ($=W_1/W_2$), we use values up to 4 in our designs because of the more significant decrease in marginal effect for width ratios higher than 4, as observed in Figure 3.3. In addition, higher width ratios require bigger surface area for the flexural supports, which means less area for the platform/electrode (for a deformable mirror of the same size).

The value of $\theta_C/\theta_{C\max}$ is determined by the equilibrium between the up-curving moment in the poly-SiGe flexural support and the torsional spring constant of the joint. In the following paragraphs, we use a 300-μm-long, 40-μm-wide uniform-width flexural support as an example to estimate the level of $\theta_C/\theta_{C\max}$ we can achieve for our deformable mirror. The 300-μm length and 40-μm width are the maxima for these dimensions that we used for all the deformable mirrors fabricated in this research. Equations 3.19 and 3.20 illustrate the equilibrium in mathematical form for a uniform-width flexural support.

$$\frac{M_{SiGe} - M_j}{EI} L = \theta_C = \frac{M_j}{k_\theta} \quad \text{(when } k_\theta > 0\text{)} \tag{3.19}$$

$$\frac{M_{SiGe}}{EI} L = \theta_{C\max} \quad \text{(when } k_\theta = 0\text{)} \tag{3.20}$$

where

M_{SiGe} is the up-curving moment generate from the stress gradient in poly-SiGe.

E is the Young's modulus of the poly-SiGe film.

I is the moment-of-inertia of the flexural support.

L is the length of the flexural support.

M_j is the moment applied to the joint, which applies a counter moment of the same magnitude to the flexural support.

k_θ is the torsional spring constant of the joint.

Using Equations 3.19 and 3.20, we derive the expressions for M_j and k_θ as functions of $\theta_C / \theta_{C\max}$ and M_{SiGe}, as shown in Equations 3.21 and 3.22.

$$M_j = \left(1 - \frac{\theta_C}{\theta_{C\max}}\right) M_{SiGe} \tag{3.21}$$

$$k_\theta = \frac{M_j}{\theta_C} = \frac{1}{\theta_C}\left(1 - \frac{\theta_C}{\theta_{C\max}}\right) M_{SiGe} = \frac{1}{\frac{\theta_C}{\theta_{C\max}}}\left(1 - \frac{\theta_C}{\theta_{C\max}}\right)\frac{EI}{L} \tag{3.22}$$

As discussed in Chapter 2, the term $\frac{M_{SiGe}}{EI}$ in Equation 3.20 is equivalent to the strain gradient of a poly-SiGe cantilever which in our structures is typically in the range of (10^{-4} to10^{-3}) μm^{-1}. As an example, assume that we use a poly-SiGe film with $\frac{M_{SiGe}}{EI}$ =10^{-3} μm^{-1} to form the flexural support (in order to achieve a large mirror elevation), and assume also that the length of the flexural support is 300 μm. For this case, we calculate $\theta_{C\max}$ to be 0.3 radians (17 degrees) using Equation 3.20. If we assume that the Young's modulus of the poly-SiGe film is 150 GPa and the width and thickness of the flexural support are 40 μm and 1 μm, respectively, we calculate the M_{SiGe} (using Equation 3.20) to be 5×10^{-10} Nm.

It can be calculated using Equation 3.23 (given below) that, in order to achieve a $\theta_C/\theta_{C\max}$ value of 0.5 ($\theta_{C\max}$ =0.5×0.3=0.15 radians), the torsional spring constant of the joint (k_θ) cannot be higher than 1.67×10^{-9} Nm-radian^{-1}.

Figure 3.5 shows the top view and an inset enlargement of a flexural support and a joint. Equation 3.23 illustrates the relationship between the torsional spring constant (k_θ) and the dimensions of the joint.

$$k_\theta = \frac{W_j t_j{}^3 G}{3L_j} \qquad 3.23$$

where L_j, W_j, and t_j are the length, width, and thickness of the joint, respectively, and G is the shear modulus of the poly-SiGe film.

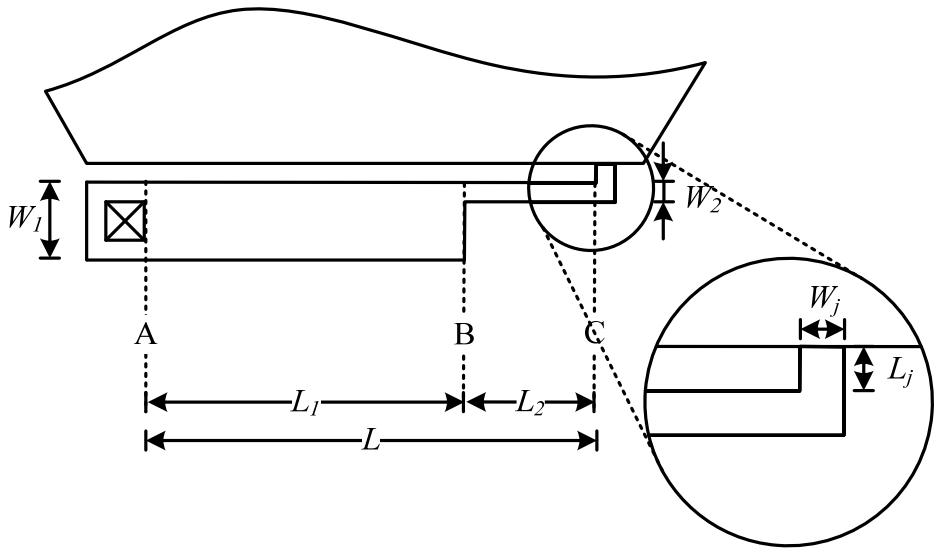

Figure 3.5: A schematic showing the top view of a flexural support and a close-up view at the joint.

Many of the material properties of poly-SiGe are similar to their counterparts in polysilicon, so we assume (for this analysis) that the poly-SiGe film has a shear modulus of 80 GPa. Using this modulus in Equation 3.23, we calculate that for W_j = 5 μm and t_j = 1 μm, the length of the joint (L_j) needs to be 80 μm to achieve a torsional spring constant (k_θ) of 4.17×10^{-10} Nm-radian^{-1}. Repeating the calculations for lower values of $\theta_C/\theta_{C\max}$, we obtain the required L_j to be 34 μm and 9 μm for $\theta_C/\theta_{C\max}$ of 0.3 and 0.1, respectively. The analysis shows that the dimensions of our deformable mirror (~300 μm on each side) make it difficult to achieve a $\theta_C/\theta_{C\max}$ value greater than 0.2 using the simple torsion-beam joint.

Other designs for the joint that can achieve lower torsional spring constants in a compact area (for example, a serpentine joint) could provide a useful future direction to advance this research.

The analysis in this section provides guidelines to maximizing/adjusting $y_C / y_{C\max}$ and $\theta_C / \theta_{C\max}$ via design parameters (i.e. the proportions for the flexural support and the dimensions for the joint) for a given stress gradient in poly-SiGe and the length of the flexural support. The stress gradient of poly-SiGe depends on the deposition parameters (see Chapter 2), and the maximum length that is allowed for the flexural support is determined by the dimensions of the deformable mirror. The deformable-mirror actuators we fabricated in this research have flexural supports that are ~300-μm long.

3.4 A Five-Mask Process to Demonstrate the Poly-SiGe Flexural Supports

A five-mask process was used to demonstrate the poly-SiGe flexural supports. Figure 3.6 illustrates the process flow with cross-sectional views of a poly-SiGe deformable-mirror actuator.

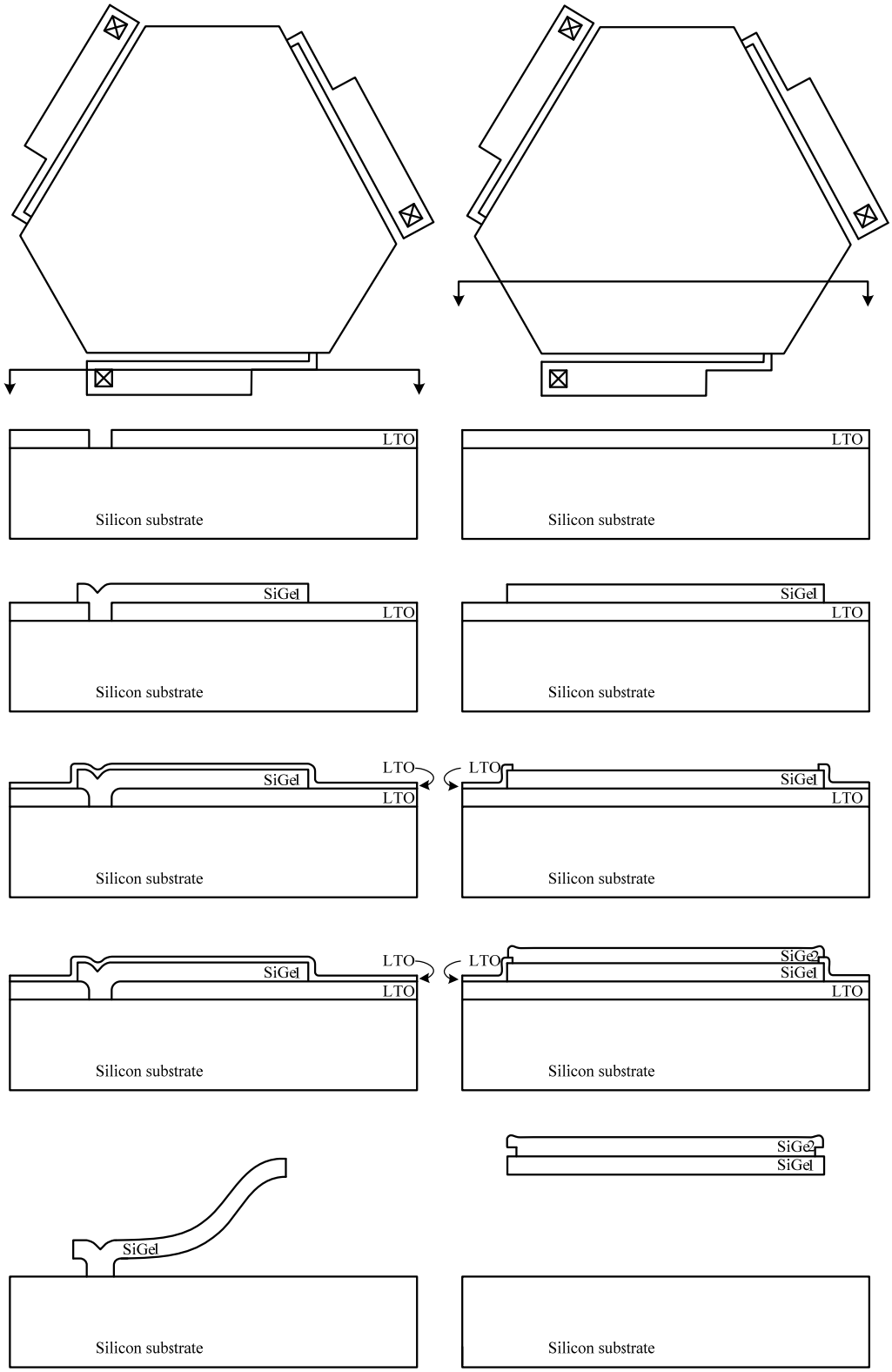

Figure 3.6: The cross-sectional views of a deformable-mirror actuator.

The process begins with a deposition of 1 μm LTO (400°C), followed by the first lithographic step to define the locations for anchors. After the anchor holes are opened, we deposit 1 μm poly-SiGe (SiGe1) at 425°C (600 mTorr, SiH_4 140 sccm, GeH_4 60 sccm, 1%BCl_3 12 sccm) and then pattern it using the second mask to define the flexural supports and the mirror platforms. As shown in Figure 3.6, the first poly-SiGe structural layer (SiGe1) forms the flexural supports and the bottom part of the mirror platforms. After patterning SiGe1, we deposit 0.3 μm LTO (400°C) to cover SiGe1 and then pattern the LTO using the third mask to expose SiGe1 in the areas of the mirror platforms, where a second poly-SiGe layer (SiGe2) is required. The 1 μm SiGe2 is deposited at 410°C (600 mTorr, SiH_4 140 sccm, GeH_4 60 sccm, 1%BCl_3 12 sccm) and then is patterned using the forth mask. The fifth mask defines the etch holes on the mirror platform. In the last step, the devices are sacrificial-released in 5:1 buffered HF. Figure 3.7 shows a SEM photo of a poly-SiGe deformable-mirror actuator after the sacrificial-release step.

Figure 3.8 is a close-up view of one of the flexural supports shown in Figure 3.7. Figure 3.9 shows the curvature of the same flexure measured using a Wyko interferometer.

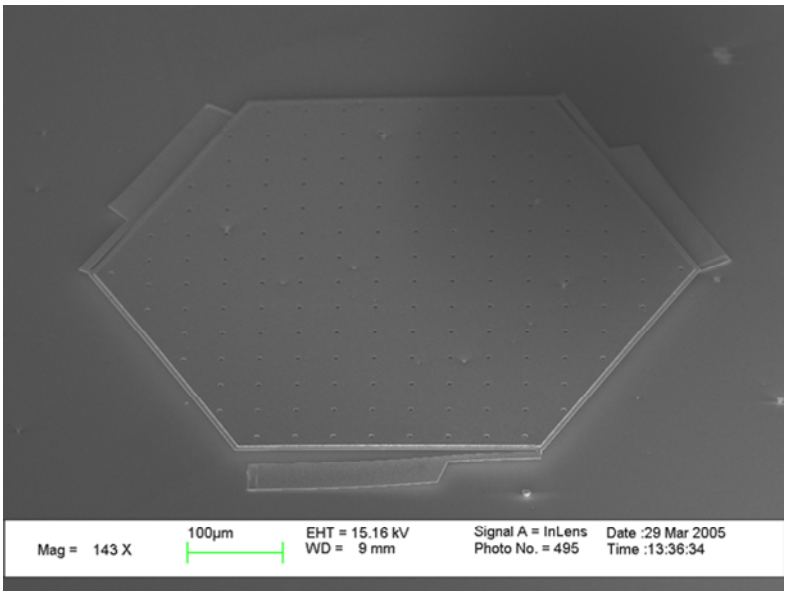

Figure 3.7: A SEM photo of a poly-SiGe deformable-mirror actuator.

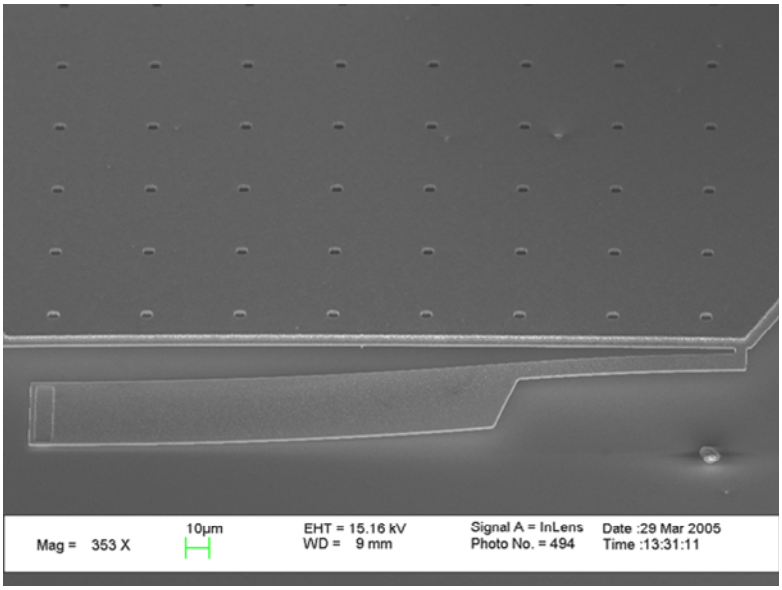

Figure 3.8: SEM photo of one of the poly-SiGe flexural supports shown in Figure 3.7. The bi-layer structure of the platform can also be seen clearly in this figure.

As shown in Figure 3.9, the 286-μm flexural support elevates the mirror platform by 14.6 μm. The gap between the platform and the substrate is therefore 15.6 μm, after the removal of 1 μm sacrificial LTO.

The widths of the flexural support shown in Figure 3.8 are 40 μm and 10 μm for the wide and narrow segments, respectively. The length of the wide segment is 188 μm, which is about 65% of the flexural support length (286 μm). As shown in Figure 3.9, the angular defection of the flexural support increases from the anchor towards the junction of the two segments, where it reaches its maximum, and then decreases towards the joint that connects the flexural support and the platform.

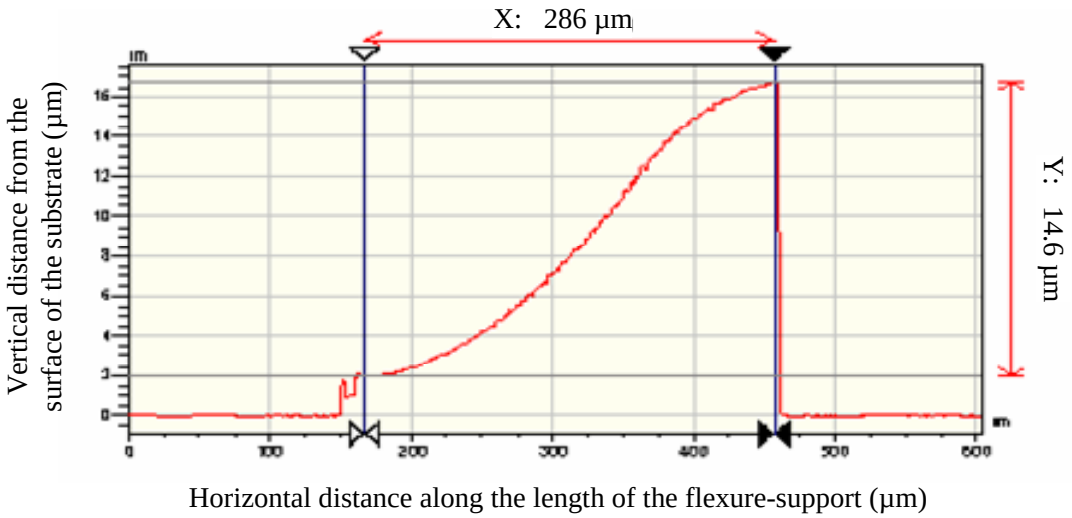

Figure 3.9: Profile showing the curvature of the flexural support pictured in the SEM of Figure 3.7. The profile is measured using a Wyko interferometer. Note that the vertical scale is much smaller than that for horizontal measurements so that angular deflections appear greatly enhanced in the figure.

To compare experimental results with the mathematical model discussed in section 3.2, we designed a number of flexural supports having various dimensions. Table 3.1 summarizes experimental measurements on these supports.

A cantilever array formed of only the first SiGe layer (which is the same layer that forms the flexural supports and is labeled as SiGe1 in Figure 3.6) was fabricated on the same substrate. The strain gradient of the cantilever array was measured to be 9.5×10^{-4} μm^{-1} (equivalent to a 1.05 mm radius-of-curvature). The vertical deflection at the free end of a 286-µm cantilever was measured to be 38

μm. In Table 3.1, we use this value as ($y_{C\max}$) to normalize the measured elevations of the platforms (because the maximum achievable elevation for a flexural support is equal to the vertical deflection of a cantilever with the same length). The normalized elevations calculated using the measured results are plotted as dots in Figures 3.10 and 3.11.

We are not equipped to measure the angular deflections at point C with high accuracy (see the schematic above Table 3.1). Therefore, we use the vertical-deflection measurements near point C and, from them, approximate the angular deflections. The values (θ_C) are also shown in Table 3.1.

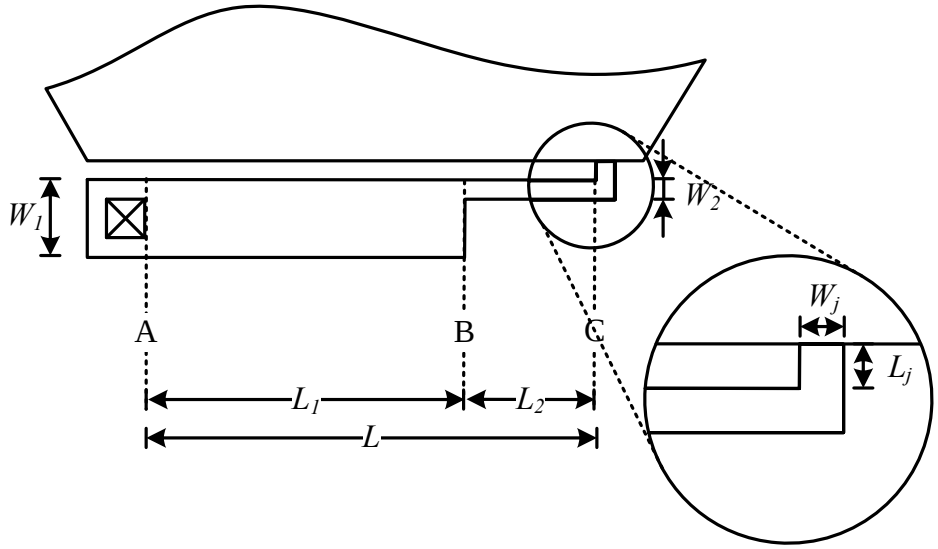

Table 3.1: Measured and normalized platform elevations (no mirrors attached) by flexural supports with different dimensions.

Data #	W_1	W_2	L_1	L_2	W_j	y_C Measured elevation	θ_C (mrad)	$\frac{P}{(\frac{L_1}{L_1+L_2})}$	$\frac{y_C}{y_{C\max}}$
1	40	10	148	138	10	12.5	3.98	0.517	0.329
2	40	10	188	98	10	13.8	3.17	0.657	0.363
3	40	10	228	58	10	12.6	2.82	0.797	0.332
4	20	5	148	138	10	11.6	1.09	0.517	0.305
5	20	5	188	98	10	13.2	7.17	0.657	0.347
6	20	5	228	58	10	11.7	2.20	0.797	0.308
7	40	20	148	138	10	8.0	4.44	0.517	0.211
8	40	20	188	98	10	7.8	11.33	0.657	0.205
9	40	20	228	58	10	7.2	7.51	0.797	0.189
10	20	10	148	138	10	7.6	7.61	0.517	0.200
11	20	10	188	98	10	7.2	8.51	0.657	0.189
12	20	10	228	58	10	6.1	5.16	0.797	0.161
13	40	10	188	103	5	14.6	11.72	0.646	0.384
14	40	40	286	0	10	4.2	8.08	1	0.109
15	20	20	286	0	10	2.8	6.37	1	0.074
16	20	20	286	0	5	4.4	12.56	1	0.115

In Table 3.1, all dimensions are recorded in μm. The lengths of the joints are the same (L_j = 5 μm) in every flexural support. The vertical deflection of a 286μm cantilever was measured to be 38μm. This value is used as $y_{C\max}$ to normalize the platform elevations (y_C).

In Figure 3.10, we plot the 16 data points in Table 3.1 to be compared with two curves derived using Equation 3.18. The two curves represent $a=W_1/W_2$=4, $\theta_C/\theta_{C\max}$ =0 (upper curve) and $a=W_1/W_2$=2, $\theta_C/\theta_{C\max}$ =0 (lower curve). As shown in Figure 3.10, the data points follow the predicted trend but are slightly above the corresponding curves, indicating that the value of $\theta_C/\theta_{C\max}$ is nonzero for every data point.

To include the effect of the nonzero $\theta_C/\theta_{C\max}$, we average the values of angular deflections (θ_C) in Table 3.1 for each group of flexural supports that have the same W_1, W_2, and W_j. For example, the data that are numbered 1, 2, and 3 have W_1, W_2, and W_j equal to 40, 10, and 10 μm, respectively, and the averaged angular deflection (θ_C) for this group is 3.32 mrad (= (3.98+3.17+2.82)/3). The averaged angular deflections are then normalized by 0.26 rad, which is the angular deflection measured at the free end of a 286μm cantilever. Using the normalized values of $\theta_C/\theta_{C\max}$, we plot the curves derived from Equation 3.18 in Figure 3.11 to be compared with the 16 data points of the experimental results.

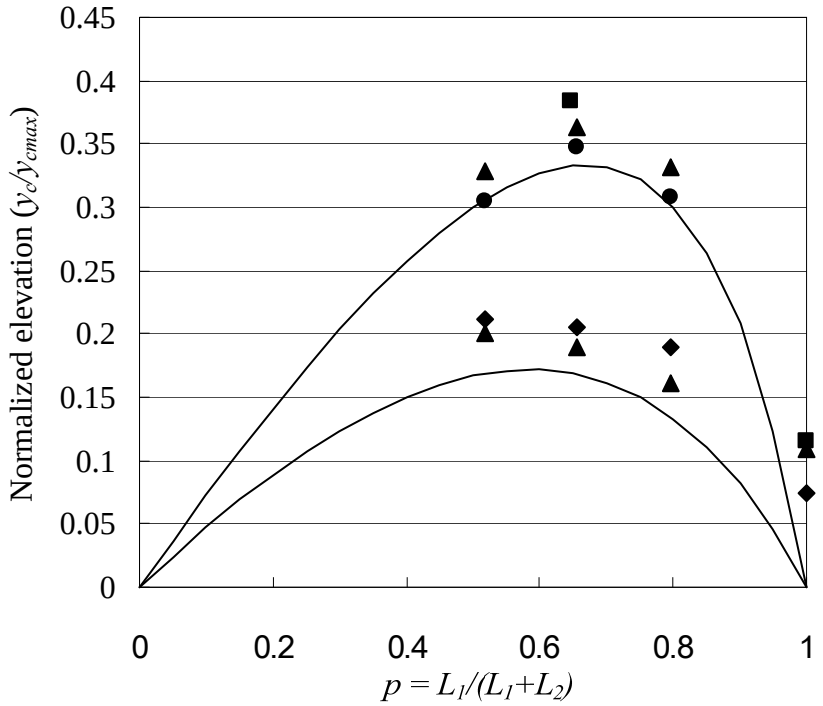

Figure 3.10: A plot to compare the 16 data points in Table 3.1 with the curves derived from Equation 3.18. The two curves represent $a=W_1/W_2$=4, $\theta_C/\theta_{C\max}$ =0 (upper curve) and $a=W_1/W_2$=2, $\theta_C/\theta_{C\max}$ =0 (lower curve).

As shown in Figure 3.11, the 16 data points of the experimental results are in fairly close agreement with the curves derived using Equation 3.18, after the effects of nonzero $\theta_C/\theta_{C\max}$ are included.

The elevation measurements of the three uniform-width flexural supports (data number 14, 15, and 16) were higher than the predicted values. Figure 3.12 shows the curvature of the 40-μm-wide uniform-width flexural support (data number 14) measured using the Wyko interferometer. The difference in curvature

between a uniform-width and a bi-width flexural support can be observed by comparing Figure 3.12 and Figure 3.9. A bi-width flexural support has a (relatively) narrower segment connected with the stiff joint. Hence, the joint causes the narrow segment to exhibit a down-curving curvature but also allows the wide segment to curve up, resulting in a higher elevation. On the other hand, a uniform-width flexural support exhibits an up-curving curvature everywhere along the beam but the curvature is constrained by the stiff joint, resulting in a lower elevation. Furthermore, the excessive stress gradient causes the flexural support to curve towards the substrate near the anchor (as seen in Figure 3.12). This curvature cannot be predicted by the mathematical model because we assume an ideal anchor (zero angular deflection at the anchor) in the model. As the result, the elevation of a uniform-width flexural support is higher than that predicted by the model (but still much lower than the elevation of a bi-width flexural support).

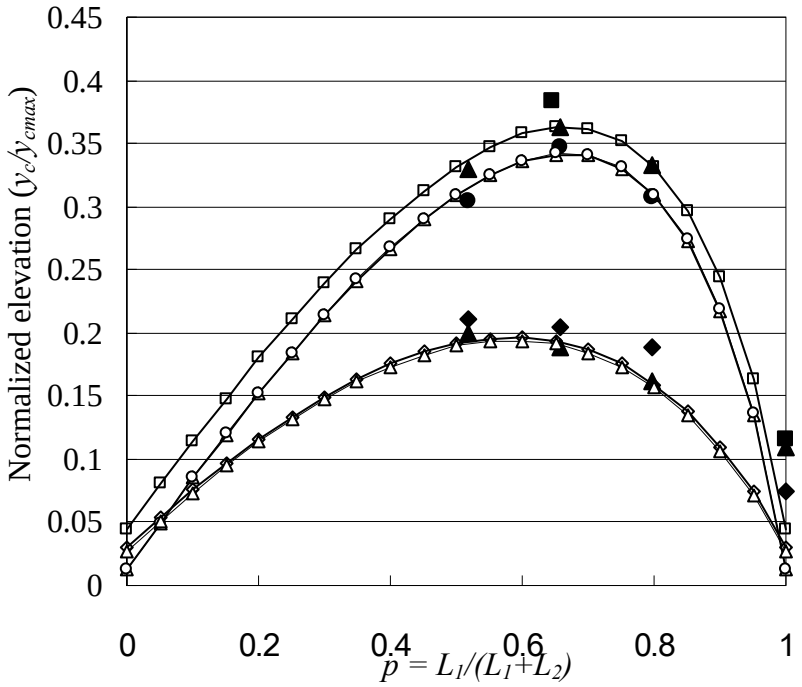

Figure 3.11: A plot to compare the 16 data points in Table 3.1 with the curves derived from Equation 3.18. Each curve has the same values for $a=W_1/W_2$ and $\theta_C/\theta_{C\max}$.

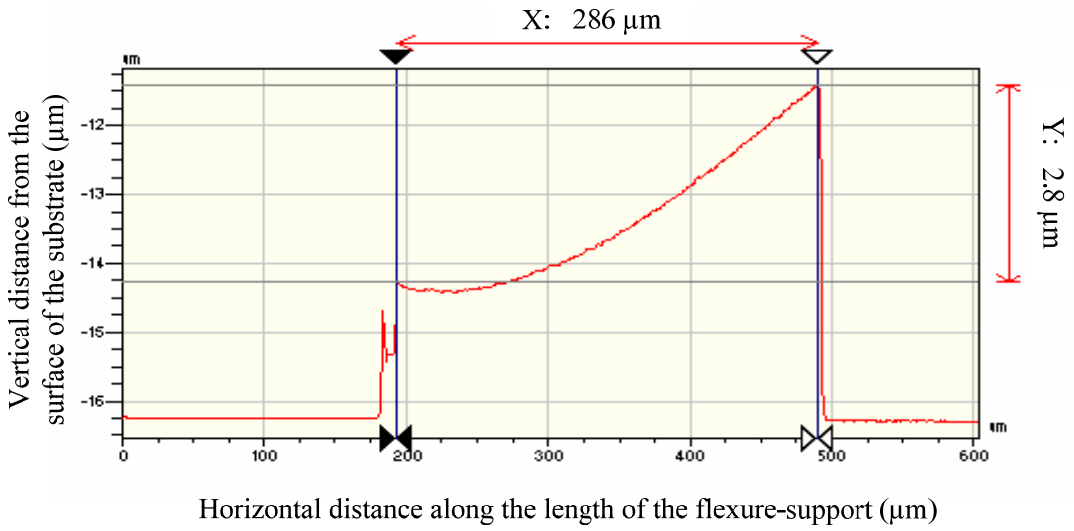

Figure 3.12: The curvature of a uniform-width flexural support measured using a Wyko interferometer.

3.5 Excimer Pulsed Laser Annealing to Increase Mirror Elevations

In the previous section, we demonstrated poly-SiGe bi-width flexures that elevate a hexagonal platform out-of-plane by 14.6 µm. Such elevation would provide a stroke of approximately 4.5 µm if the poly-SiGe structure is actuated as an electrostatic parallel-plate actuator. To achieve strokes in the range of 10-20 µm, which is required for deformable mirrors used in vision-science AO systems, the elevation would have to be enhanced further.

In this section, we investigate the use of an excimer-pulsed laser to enhance the out-of-plane bending of the poly-SiGe flexural supports. The effects of excimer-pulsed-laser annealing on the strain gradients of poly-SiGe films have been studied and reported in Sedky et al. [19-22] and Low et al. [23]. In excimer-

pulsed-laser annealing, the beam delivers high energy pulses (200-800 mJ-cm^{-2}) in very short intervals (38 ns) to the surface of the poly-SiGe film. The high energy of the laser recrystallizes the surface of the poly-SiGe film. The depth of penetration depends on the laser energy, and is typically in the range of 0.1 to 0.3 μm for the range of the laser energy we use. After the recrystallizeation, the surface portion of the poly-SiGe film becomes more tensile than the rest of the film. Consequently, the excimer-pulsed-laser annealing of poly-SiGe results in an enhanced stress gradient.

Table 3.2 shows the experimental results of using excimer-pulsed laser to enhance the strain gradient of poly-SiGe in a 4×4 mm^2 area. This area is the size of the laser beam that we used in the experiment. It also covers the area of an aperture size of 3.5 mm in diameter that is required for deformable mirrors used in vision-science AO systems.

Table 3.2: Strain gradients of poly-SiGe films after excimer-pulsed-laser annealing at different energies

Laser energy	Number of pulses	Strain gradient (μm^{-1})	Uniformity across a 4×4 mm^2 area
without laser annealing	--	5.3×10^{-4}	< ±1%
300 mJ-cm^{-2}	1	1.3×10^{-3}	±25%
500 mJ-cm^{-2}	1	3.5×10^{-3}	±5%

The results show that the strain gradient of the poly-SiGe film is enhanced by 2.5 times (from 5.3×10^{-4} to 1.3×10^{-3} μm^{-1}) at a laser energy of 300 mJ-cm^{-2}, and by 6.6 times (from 5.3×10^{-4} to 3.5×10^{-3} μm^{-1}) at a laser energy of 500 mJ-cm^{-2}. The

uniformity of the strain gradient is also improved at higher laser energy, as shown in Table 3.2.

With a strain gradient of 3.5×10^{-3} μm^{-1}, poly-SiGe bi-width flexural supports with a length of 300 μm would elevate the micromirror by approximately 52 μm. In the next chapter, the excimer-pulsed-laser annealing step is incorporated in the fabrication of a 37-segment deformable-mirror array to achieve large mirror elevations. It has been studied and reported in Sedky et al. [19-22] and Low et al. [23] that the excimer-pulsed-laser annealing does not affect the stability of the poly-SiGe films.

3.6 Conclusion

In this chapter, we describe a novel "bi-width" flexural-support structure that can be used to elevate the top plate of a micromechanical parallel-plate actuator, thereby creating a large gap for large-stroke actuation. The "bi-width" flexural-support structure utilizes the stress gradient in poly-SiGe to achieve the large elevation. The theories behind the "bi-width" shape of the flexural supports are derived in this chapter, and are used to design flexural supports for deformable-mirror actuators. We have demonstrated poly-SiGe bi-width flexural supports that elevate a hexagonal platform (300 μm-long on each side) out-of-plane by 14.6 μm. The elevation can be further increased by annealing the poly-SiGe structural layer using excimer-pulsed laser. We have demonstrated an approximately 7x increase in out-of-plane deflection by using a laser energy of 500 mJ-cm^{-2}. The theories and

experimental results both show that we can use the poly-SiGe flexural supports to achieve the large-stroke actuation required for deformable-mirror actuators used in vision-science AO systems. In the next chapter, we will describe a complete deformable-mirror actuator that incorporates the flexural supports described in this chapter.

Chapter 4 : Design and Fabrication of Deformable Mirrors Using a CMOS-Compatible Micromachining Process

4.1 The Micromachining Process Flow

The goal of this thesis research is to demonstrate a deformable mirror structure for adaptive-optics applications with a thermal budget for the micromachining process that is sufficiently low to allow post-CMOS integration.

It has been shown in previous research [24-28] that poly-SiGe is an attractive structural material for micromechanical devices that are intended for post-CMOS integration. The main advantages of poly-SiGe are that its mechanical properties are roughly similar to those of polysilicon, but the material can be deposited at much lower temperatures (below 425°C) than are needed for polysilicon. In this research, we use poly-SiGe as the structural material for the deformable mirrors.

The most important constraint in designing a micromachining process intended for post-CMOS integration is the thermal budget allowed by the CMOS technology. Researchers have shown that the allowable thermal budget depends on the specific CMOS technology [29-31]. In this thesis research, we use the thermal-budget limit reported by Takeuchi et al. [29] for a 0.25-μm foundry CMOS technology as a guideline to design the micromachining process. The reported thermal-budget limit was determined using the same deposition furnaces in the Microfabrication Laboratory of UC Berkeley as those used for this research. It was found that the thermal-budget limit for integration with a 0.25-μm foundry CMOS is 6 hr at 425°C (or 1 hr at 450°C, or 0.5 hr at 475°C). It was also discovered that the increase in via resistance (used for circuit interconnections), rather than degradation in the CMOS transistor performances, limits the thermal budget of post-processing. In this chapter, we first present the micromachining process flow for the deformable mirror that involves steps at various temperatures. Then we use the empirical equations presented in Takeuchi et al. [29] to establish grounds for the feasibility of integrating the micromachining process together with foundry CMOS technologies.

Another important constraint for a post-CMOS micromachining process is that the use of hydrofluoric acid (HF) in the sacrificial-release step needs to be avoided if the interconnect stack of the CMOS electronics is exposed during the sacrificial-release step. The reason is that the materials used in the interconnect stacks of most CMOS technologies (i.e. aluminum and silicon dioxide) do not have

etch resistance to HF. To avoid the use of HF. in the micromachining process for the deformable mirrors, we use polycrystalline-germanium (poly-Ge) as the sacrificial material, and use hydrogen peroxide (H_2O_2) to etch away the poly-Ge sacrificial layer in the release step. The use of poly-Ge as the sacrificial material adds complication to the fabrication process, however, because the reactive-ion-etch (RIE) step used to pattern the poly-SiGe structural layers etches both poly-SiGe and poly-Ge. Therefore, poly-Ge cannot serve as an etch-stop layer for the patterning of poly-SiGe. This issue is addressed in more detail in the following paragraphs when we discuss the process flow.

In Figures 4.1-4.5, we illustrate the process flow using the top view and two cross-sectional views of one deformable mirror.

Before the beginning of the micromachining process, a 1 μm low-stress silicon-nitride (LSN) layer is deposited to passivate the silicon substrate. This nitride layer mimics the passivation layer that is usually laid down as the topmost layer in CMOS technology.

The first layer of the micromachining process is a 0.25 μm poly-SiGe (labeled as $SiGe_0$ in Figure 4.1) deposited at 410°C (40 min, 600 mTorr, SiH_4 140 sccm, GeH_4 60 sccm, 1%BCl_3 12 sccm). As shown in Figure 4.1, this SiGe0 layer is patterned to form three bottom electrodes and three rectangular strips surrounding the electrodes on which the flexural supports will be anchored. In our actuation scheme, a bias voltage is supplied to the top plate (acting as an electrode) through these rectangular strips.

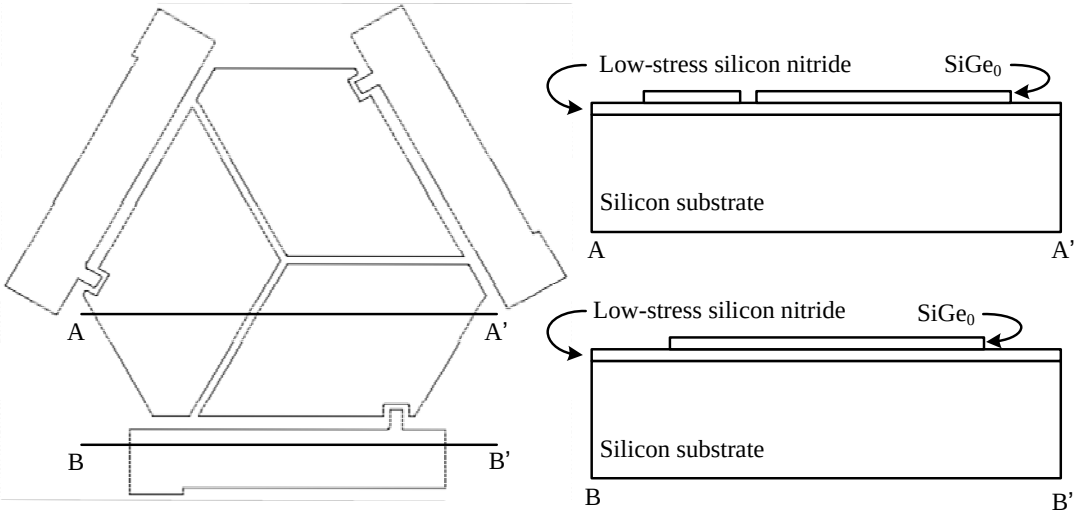

Figure 4.1: Top and cross-sectional sketches for a single deformable mirror after the $SiGe_0$ layer is patterned.

After the $SiGe_0$ layer is patterned, a 0.25 μm low-temperature oxide (labeled as LTO_1 in Figure 4.2) is deposited at 400°C (17 min); then a 1 μm-thick poly-Ge layer, which is the sacrificial layer of the micromachining process, is deposited at 350°C (150 min, 300 mTorr, GeH_4 100 sccm, 1%BCl_3 12 sccm). The 0.25 μm LTO_1 layer serves as the etch-stop layer for the patterning of the poly-Ge sacrificial layer because the reactive-ion-etch step that is used to pattern poly-Ge does not have etch selectivity between poly-Ge and poly-SiGe. After the anchor-hole patterns are defined using a lithographic mask, the poly-Ge layer and the LTO_1 layer are patterned in consecutive reactive-ion-etch steps using different etchers to open the anchor holes. Having the LTO_1 layer between the poly-Ge layer and the $SiGe_0$ layer, we obtain etch selectivity in each of the two reactive-ion-etch steps

and hence can properly over-etch both layers to overcome cross-wafer variation in thicknesses, without etching excessively into the $SiGe_0$ layer.

The first poly-SiGe structural layer (labeled as $SiGe_1$ in Figure 4.2) is a 0.9 μm poly-SiGe deposited at 425°C (110 min, 300 mTorr, SiH_4 140 sccm, GeH_4 100 sccm, 1%BCl_3 12 sccm). The reason for choosing 0.9 μm for the thickness of this layer is discussed in Section 4.3, where we discuss the design considerations for the flexural supports. Prior to the deposition of the $SiGe_1$ layer, the wafers are dipped in 100:1 HF for 60 sec to remove native oxide in the anchor holes. After the deposition, the $SiGe_1$ layer is annealed using a single excimer-laser pulse at 500 mJ-cm^{-2}. As was discussed in Chapter 3, the excimer-laser pulse recrystallizes the surface of the $SiGe_1$ layer, resulting in an enhanced stress gradient. The $SiGe_1$ layer is patterned to from the flexural supports and the bottom layer of the mirror platform. Due to the lack of etch selectivity between poly-SiGe and poly-Ge in the reactive-ion-etch step, the patterning of the $SiGe_1$ layer is carefully timed using a calibrated etch rate obtained by etching test wafers that are included in the same deposition batch with the device wafers.

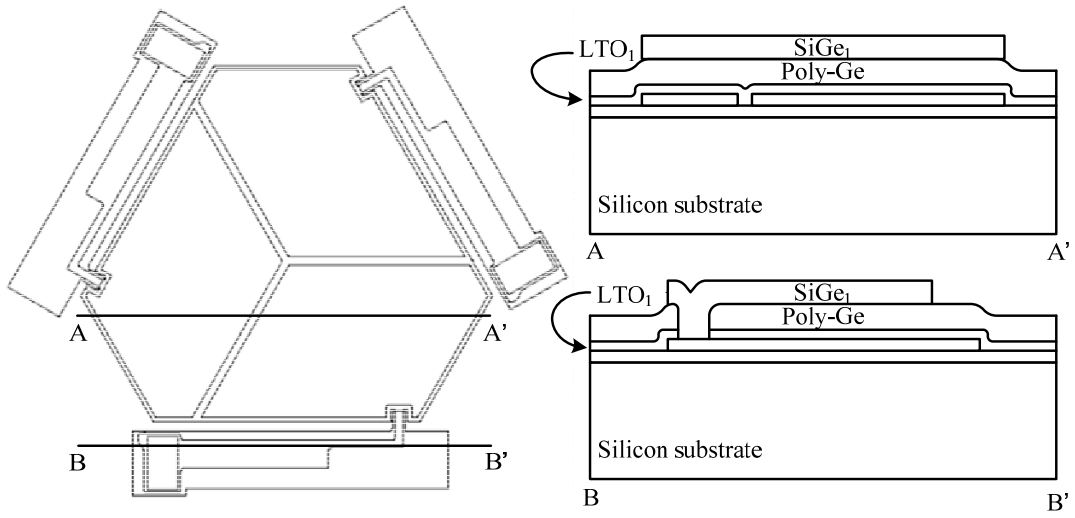

Figure 4.2: Cross-sectional sketches for a single deformable mirror after the $SiGe_1$ layer is patterned.

After the $SiGe_1$ layer is patterned, a 0.3 μm low-temperature oxide (labeled as LTO_2 in Figure 4.3) is deposited at 400°C (20 min). The purpose of this LTO_2 layer is to cover the areas in which a second poly-SiGe layer is not needed. Hence, after the deposition, the LTO_2 layer is patterned to expose the mirror-platform area.

After the pattering of the LTO_2 layer, a 1 μm poly-SiGe (labeled as $SiGe_2$ in Figure 4.3) is deposited at 410°C (180 min, 600 mTorr, SiH_4 140 sccm, GeH_4 60 sccm, 1%BCl_3 12 sccm). The 1 μm thickness for this SiGe2 layer is determined using the experimental procedures presented in Section 2.6, with the goal of minimizing the effective strain gradient of the bilayer ($SiGe_1$+$SiGe_2$) mirror platform. The reactive-ion-etch step that patterns the $SiGe_2$ layer also opens the etch holes in the mirror-platform area. Because the mirror platform is formed of a bilayer poly-SiGe, we need to etch through both the $SiGe_1$ and $SiGe_2$ layers in the

reactive-ion-etch step in order to open the etch holes in the mirror platform completely. During this reactive-ion-etch step, the flexural supports are protected by the LTO_2 layer owing to the etch selectivity between poly-SiGe and LTO. After the etch holes are completely opened, the wafers are dipped in 10:1 HF for 4 min to remove the LTO_2 layer. This HF-dip step does not affect the compatibility with CMOS technologies because the underlying CMOS electronics would not be exposed when it is carried out. As seen in Figure 4.3, the poly-Ge layer covers all the underlying layers.

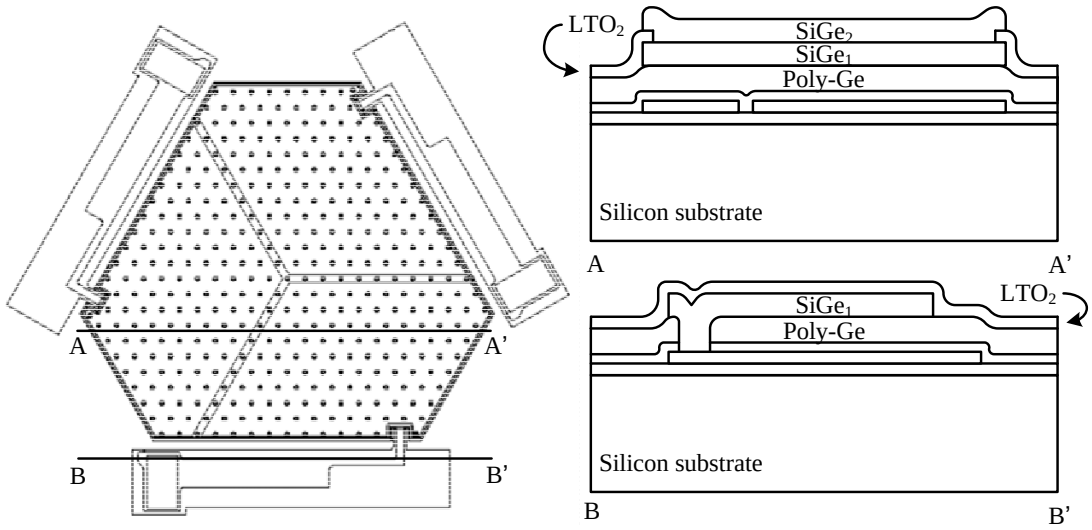

Figure 4.3: Cross-sectional sketches for a single deformable mirror after the $SiGe_2$ layer is patterned.

As discussed in Chapter 1, the specifications for the deformable mirror require that the rms (root-mean-square) deformation of the optical surface be less than 30 nm (equivalent to a peak-to-valley deformation of 42 nm). This value of

maximum allowed deformation can be used to calculate the maximum strain gradient that is allowed in the structural film that forms the mirror. The hexagonal mirror is about 300 μm from its center to the vertices. Given that the difference in height between the vertices and the center cannot exceed 42 nm, we derive (using Equation 1.1) that the maximum allowed strain gradient in the structural film that forms the mirror is 9.3×10^{-7} μm^{-1}. At this time, it has not been demonstrated that the strain gradient in poly-SiGe can be reduced to such a low level. The lowest strain gradient that has been demonstrated is 1.1×10^{-6} μm^{-1} [31], reported in 2006. Therefore, we cannot use poly-SiGe to form the "mirror" part of the deformable-mirror device.

It has been demonstrated by Helmbrecht et al. [32-34] that the top single-crystalline-silicon layer of a SOI wafer can be used to form mirror segments having high quality (rms deformations lower than 10.3 nm). This approach is adopted into our fabrication process for the deformable mirror. A joint project was established with Iris AO, Inc. in 2006 to assemble 20 μm-thick single-crystalline-silicon mirrors, which are fabricated using a SOI wafer by Iris AO, Inc., onto our poly-SiGe deformable-mirror actuators using a flip-chip-bonding step.

The mirrors are fabricated by etching through the 20 μm-thick top single-crystalline-silicon layer of a SOI wafer in a deep-reactive-ion-etch (DRIE) step using a STS inductively-coupled-plasma (ICP) system. In order to attach the single-crystalline-silicon mirrors to the poly-SiGe actuators, we use gold (Au) as the bonding material between the mirrors and the actuators. Before the flip-chip-

bonding step, matching patterns of gold bondsites are formed on both the mirrors and the actuators. The process to form gold bondsites begins with sputter-depositions of 10 nm of chrome (Cr) and then 100 nm of gold. The chrome layer serves as the adhesion layer between gold and poly-SiGe (actuators) or single-crystalline-silicon (mirrors). We then use a lithographic step to cover the actuators or mirrors with photoresist except the locations of the bondsites. An electroplating step is then used to grow the gold in the exposed bondsite locations to 3 μm thick (The sputter-deposited 100 nm gold layer serves as the seed layer in the electroplating step). At last, we remove the photoresist and then dip the wafers in gold etchant (TFA) and chrome etchant (Cr-7) to remove the chrome and gold in the areas other than the bondsites. The wafers are diced into chips before the flip-chip-bonding step. Figure 4.4 shows the cross-sectional views of one deformable mirror after the gold bondsites are deposited.

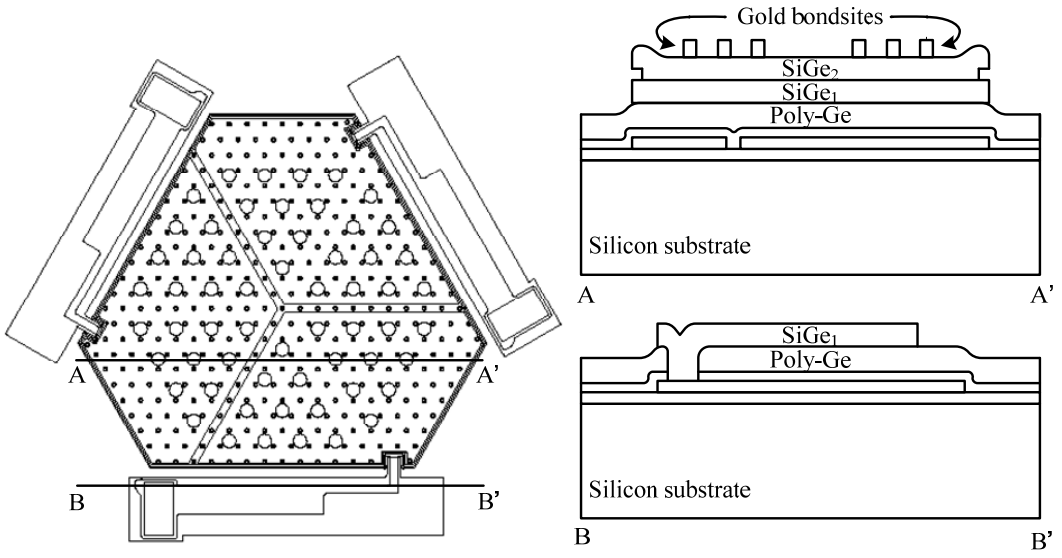

Figure 4.4: Cross-sectional sketches for a single deformable mirror after the gold bondsites are formed.

The flip-chip-bonding step is carried out using a Suss Microtech FC150 flip-chip bonder. In the bonding step, the matching patterns of gold bondsites on the mirrors and the actuators are carefully aligned before being pressed against each other while heated at 350°C for 10 min to form a strong bond. After the mirror chip is flip-chip-bonded to the actuator chip, the substrate of the mirror chip is removed in a deep-reactive-ion-etch step. The silicon dioxide layer of the SOI substrate serves as an etch-stop layer in this step. After the etch step is completed, the chips are placed in 49% HF for 5 min to remove the silicon dioxide layer.

In the last step of the fabrication process, the sacrificial poly-Ge layer is etched away in H_2O_2 at ambient temperature for 200 min to release the deformable mirror. The device is critical-point-dried after the sacrificial release step. Figure 4.5

shows the cross-sectional views of one deformable mirror before and after the sacrificial release step.

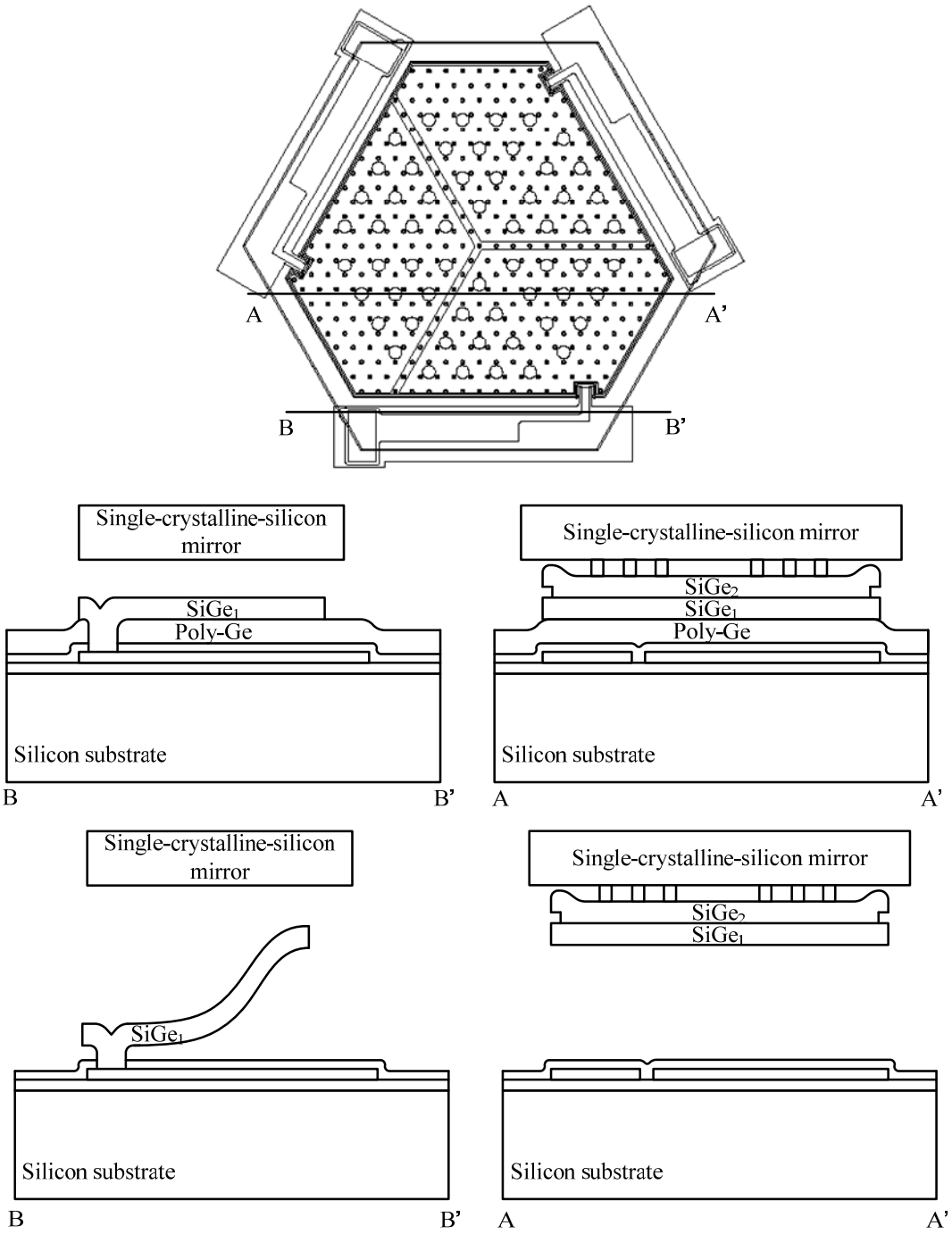

Figure 4.5: Cross-sectional sketches for a single deformable mirror before and after the sacrificial-release step.

4.2 Thermal Budget of the Micromachining Process

The micromachining process flow presented in Section 4.1 is designed to be compatible with foundry CMOS technologies. In Table 4.1, we summarize the thermal steps in the process flow. The deposition furnaces in the Microfabrication Laboratory of UC Berkeley are setup to have a 60-minute temperature-stabilization step before each deposition. Therefore, we include an additional 60 min to each of the deposition steps, as shown in Table 4.1.

Table 4.1: Thermal steps in the micromachining process for the DMs

Step	Processing temperature of step (°C)	Time of step (min)	Temperature-stabilization time of the furnace (min)	Total processing time of step (min)
Deposition of $SiGe_0$	410	40	60	100
Deposition of LTO_1	400	17	60	77
Deposition of poly-Ge	350	150	60	210
Deposition of $SiGe_1$	425	110	60	170
Deposition of LTO_2	400	20	60	80
Deposition of $SiGe_2$	410	180	60	240
Flip-chip bonding	350	10	--	10

In an integrated process, the CMOS electronics would experience these temperatures for corresponding times during the fabrication of the deformable mirrors. The highest temperature occurs in the deposition of $SiGe_1$, which is at 425°C for 170 min.

In this section, we use an empirical model reported in Takeuchi et al. [29] to determine the feasibility of integrating the deformable mirrors with CMOS

electronics. The experiment was conducted using the same deposition furnaces in the Microfabrication Laboratory of UC Berkeley as those used for this thesis research. The procedures of the experiment were as follows: 0.25-μm CMOS chips provided by a foundry were placed in the furnaces at various temperatures for incremental amounts of time. The performance of the CMOS electronics was measured before and after each furnace step to monitor degradation. It was discovered that, for the 0.25-μm CMOS technology under study, the increase in via resistance (used for circuit interconnections), rather than degradation in the CMOS transistor performances, limits the thermal budget of post-processing. It was observed that the via resistance increased more than 10% after 6 hr at 425°C, or 1 hr at 450°C, or 0.5 hr at 475°C. This 10% increase in via resistance occurred before other degradations were observed. Therefore, in Takeuchi et al. [29], the 10% increase in via resistance is defined as the criterion of failure.

An empirical equation (Equation 4.1) was derived from the experimental data, which shows that the via resistance (R_{via}) increases linearly with the processing time to a power of 1.5 ($t^{1.5}$). In addition, the degradation coefficients (A_0) exhibit Arrhenius behavior with an activation energy of 4.4 eV.

$$\Delta R_{via} = A_0 t^{1.5} \qquad 4.1$$

where

$A_0 = 1.25 \times 10^{27} \exp(-4.4/kT)$

and

ΔR_{via} is the increase in via resistance (Ω). The initial via resistance is ~2.3Ω.

A_0 is the degradation coefficient at a given temperature (Ω-min$^{2/3}$). The unit has a 2/3-power term because in Equation 4.1 the via resistance (R_{via}) increases linearly with the processing time to a power of 1.5 ($t^{1.5}$).

t is the post-processing time (min).

k is the Boltzmann constant (=8.617×10^{-5} eV-K^{-1}).

T is the post-processing temperature (K).

Using Equation 4.1, we can estimate the maximum allowable post-processing time at any given temperature such that the via resistance of the 0.25-μm CMOS electronics would not increase by more than 10%, which was defined as the criterion of failure according to Takeuchi *et al* as described above [29]. Table 4.2 summarizes the maximum allowable post-processing times at temperatures ranging from 350°C to 475°C. The maximum allowable times for 425-475°C were determined in the experiment, whereas those for 350-410°C were estimated using Equation 4.1 derived from the experimental results for 425-475°C.

Table 4.2: Maximum allowable post-processing times at given temperatures

Post-processing temperature (°C)	Maximum allowable post-processing time (min)
475	30
450	60
425	360
410	1260
400	2700
350	15600

The micromachining process for our deformable mirror involves thermal steps at several temperatures. Using Equation 4.1, we can estimate the increase in via resistance caused by each thermal step of the micromachining process. The processing temperatures and times shown in Table 4.1 are used in this calculation, and the calculation results are summarized in Table 4.3.

Table 4.3: Estimated percentage increases in via resistance caused by the micromachining process.

Step	Processing temperature of step (°C)	Total processing time of step (min)	Estimated percentage increase in via resistance of step
Deposition of $SiGe_0$	410	100	0.2%
Deposition of LTO_1	400	77	<0.1%
Deposition of poly-Ge	350	210	<0.1%
Deposition of $SiGe_1$	425	170	2%
Deposition of LTO_2	400	80	<0.1%
Deposition of $SiGe_2$	410	240	0.7%
Flip-chip bonding	350	10	<0.1%

Based on the analysis above, use of the micromachining process presented in Section 4.1 to fabricate deformable mirrors on top of a 0.25-μm foundry CMOS

technology would be compatible with CMOS processing. The thermal budget for the process would be carried out without causing the via resistance of the CMOS to increase by more than 10%, the increase reported as the limiting factor for post-processing at the 0.25-μm technology node. The allowable thermal budget is higher at lower technology nodes. For example, as reported by Sedky et al. [30], the allowable thermal budget is 1.5 hr at 525°C for a 0.35-μm CMOS technology. Therefore, we conclude that the micromachining process presented in this chapter can be integrated with foundry CMOS technologies.

4.3 Deformation-Mirror Design Considerations

In Chapter 3, we derived the mathematical model for the design of flexural supports with the goal of maximizing mirror elevations. Aside from elevating the mirrors to create large gaps for large displacements, the flexural supports also serve as the springs of the actuators. Therefore, the spring constant of the flexural supports significantly affects the performance of the deformable mirrors, including the actuation voltages and resonant frequencies. When designing deformable mirrors intended for integration with CMOS electronics, we need to minimize the actuation voltages because there are fewer foundry CMOS technologies that can supply/sustain high voltages, and these technologies are typically expensive. The resonant frequency determines the step-response times, including both rise and fall times, of the deformable mirrors in response to the control voltages. The minimum

required resonant frequency is approximately 200 Hz for vision-science application [1].

In this section, we first derive the equations that can be used to calculate the spring constant of the “bi-width” flexural supports. Then, we derive the equations to calculate the resonant frequency of the deformable mirrors. Last, we discuss deformable-mirror design considerations to achieve the performance required for the intended applications.

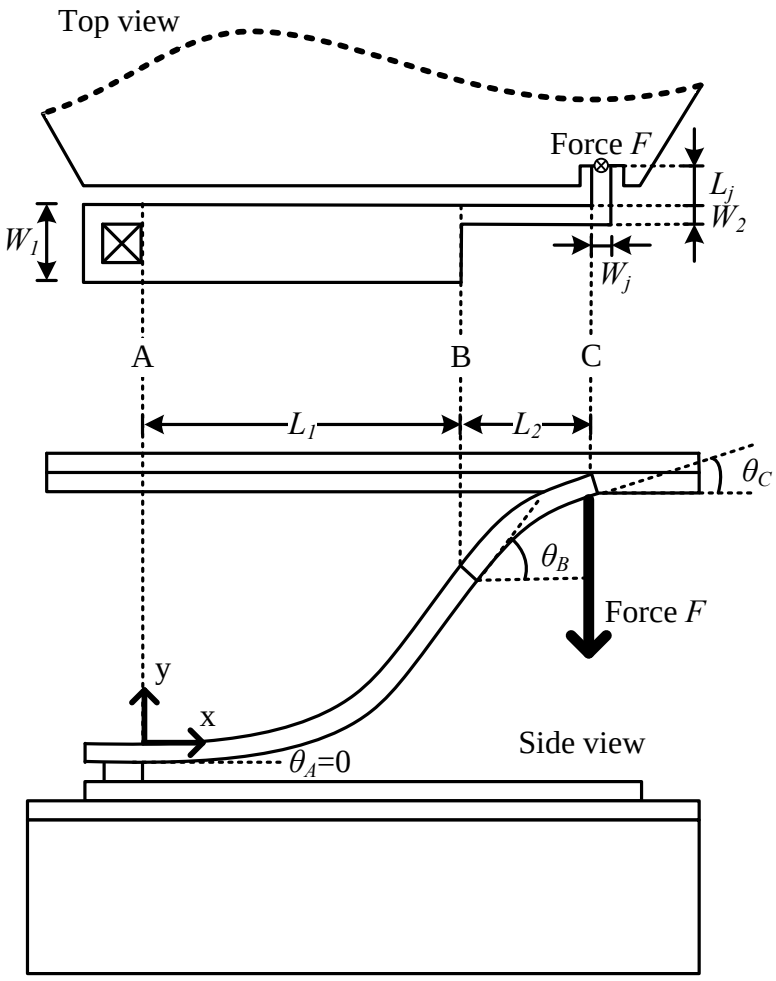

Figure 4.6: Schematics showing one flexural support with a force *F* applied to it.

Figure 4.6 shows a bi-width flexural support with a force (*F*) applied at the point where the torsional joint of the flexural support meets the mirror platform. Following the derivations in Chapter 3 for the flexural supports with the addition of the force (*F*), we can express the angular deflection ($\theta(x)$) and vertical deflection ($y(x)$) at the joint ($x = L_1 + L_2 = L$) using Equations 4.1 and 4.2. The notations

used in the equations are the same as those defined and used in Sections 3.2 and 3.3.

$$\theta(L) = \frac{1}{EI_1}\left(M_1 - M_j - FL + \frac{FL_1}{2} \right) L_1 + \frac{1}{EI_2}\left(M_2 - M_j - FL + FL_1 + \frac{FL_2}{2} \right) L_2 \quad 4.1$$

$$y(L) = \frac{1}{EI_1}\left(\left(M_1 - M_j - FL\right) L_1 L_2 + \frac{FL_1{}^2 L_2}{2} + \frac{\left(M_1 - M_j - FL\right) L_1{}^2}{2} + \frac{FL_1{}^3}{6} \right) + \frac{1}{EI_2}\left(\frac{\left(M_2 - M_j - FL + FL_1\right) L_2{}^2}{2} + \frac{FL_2{}^3}{6} \right) \quad 4.2$$

As discussed in Section 3.?, when there is no additional force applied to the flexural support (i.e. F=0), the down-curving moment applied at the joint (M_j) is determined by the equilibrium between the up-curving moment in the flexural support and the torsional spring constant of the joint. In the case when a force (F) is applied to the flexural support, the down-curving moment (M_j) is increased but can still be expressed as a function of the torsional spring constant of the joint (k_θ) and the angular deflection at the joint ($\theta(L)$), as shown in Equation 4.3.

$$M_j = k_\theta \theta(L) \quad 4.3$$

Substituting Equation 4.3 into Equation 4.1, we can derive a new expression for $\theta(L)$, as shown in Equation 4.4.

$$\theta(L) = \frac{\frac{1}{EI_1}\left(M_1 - FL + \frac{FL_1}{2}\right)L_1 + \frac{1}{EI_2}\left(M_2 - \frac{FL_2}{2}\right)L_2}{1 + \frac{k_\theta}{EI_1}L_1 + \frac{k_\theta}{EI_2}L_2} \qquad 4.4$$

Because the applied force (*F*) decreases the vertical deflection at the joint ($y(L)$), we define the spring constant of the flexural support (k_y) as the negative of the partial derivative of the applied force (*F*), with respect to the vertical deflection ($y(L)$), shown in Equation 4.5.

$$k_y = -\frac{\partial F}{\partial y(L)} = \left(-\frac{\partial y(L)}{\partial F}\right)^{-1} \qquad 4.5$$

Substituting Equations 4.2-4.4 into Equation 4.5, we derive the expression for the spring constant of the flexural support (k_y), shown in Equation 4.6.

$$k_y = \left(\frac{1}{EI_1}\left(k_\theta \frac{\partial\theta(L)}{\partial F}\left(L_1L_2 + \frac{{L_1}^2}{2}\right) + LL_1L_2 + \frac{{L_1}^3}{3}\right) + \frac{1}{EI_2}\left(k_\theta \frac{\partial\theta(L)}{\partial F}\frac{{L_2}^2}{2} + \frac{{L_2}^3}{3}\right)\right)^{-1} \qquad 4.6$$

where

$$\frac{\partial\theta(L)}{\partial F}=\frac{\frac{1}{EI_1}\left(-L+\frac{L_1}{2}\right)L_1+\frac{1}{EI_2}\left(-\frac{L_2}{2}\right)L_2}{1+\frac{k_\theta}{EI_1}L_1+\frac{k_\theta}{EI_2}L_2}$$

Using Equation 4.6, we can calculate the spring constant of any bi-width flexural support with given dimensions.

Our deformable mirror has three bottom electrodes that are independently controlled and therefore can be actuated in both piston mode and tip/tilt mode. When actuated in piston mode, the deformable mirror can be modeled as a parallel-plate electrostatic actuator. In this mode, the three flexural supports exhibit the same movements when actuated and therefore can be modeled as three springs in parallel.

The relationships between actuation voltage, resonant frequency, and spring constant of a parallel-plate electrostatic actuator have been derived and reported in Helmbrecht [1]. Therefore, the derivations are not repeated here. Equations 4.7 and 4.8 are the key equations that express the relationships.

$$k_{y\_piston}\Delta y=\frac{1}{2}\varepsilon_0 V^2\frac{A_e}{(y_0-\Delta y)^2} \qquad 4.7$$

$$\omega_0^{'} = \omega_0 \left(\frac{1 - \frac{3\Delta y}{y_0}}{1 - \frac{\Delta y}{y_0}} \right)^{1/2} = \left(\frac{k_{y\_piston}}{m} \right)^{1/2} \left(\frac{1 - \frac{3\Delta y}{y_0}}{1 - \frac{\Delta y}{y_0}} \right)^{1/2} \qquad 4.8$$

where

k_{y_piston} is the spring constant when the deformable mirror is actuated in piston mode.

y_0 is the original position of the deformable mirror, when no actuation voltage is supplied.

Δy is the displacement of the deformable mirror from its original position (y_0).

ε_0 is the permittivity of free space (~8.854×10^{-12} F/m).

V is the actuation voltage.

A_e is the area of the electrode.

m is the mass of the deformable mirror.

ω_0 is the mechanical resonant frequency (natural resonant frequency) of the deformable mirror.

$\omega_0^{'}$ is the resonant frequency of the deformable mirror at the displacement Δy.

Equation 4.7 illustrates the equilibrium between the spring restoring force (left-hand side) and the electrostatic force (right-hand side). Equation 4.8 expresses the resonant frequency of the actuator as a function of mass, spring constant, and displacement. The relationship shows a reduction in resonant frequency with increasing displacement. This phenomenon is due to the nonlinear electrostatic force with respect to position inherent to parallel-plate actuation. The resonant frequency of the actuator is equal to the mechanical resonant frequency at zero displacement, and reduces to zero when the displacement reaches one-third of the gap.

Rearranging the terms in Equation 4.7, we derive an expression for the actuation voltage (V), shown in Equation 4.9

$$V = \left(\frac{2k_{y\_piston}\Delta y(y_0 - \Delta y)^2}{\varepsilon_0 A_e} \right)^{1/2} \qquad 4.9$$

Equations 4.8 and 4.9 show a trade-off between actuation voltages and resonant frequency. Deformable mirrors with stiffer flexural supports (higher k_y) and smaller mirrors (smaller m and A_e) could be operated at higher frequency (higher ω_0'), but would require higher voltages to drive (higher V).

Equations 4.6, 4.8, and 4.9 can be used to determine the design parameters for the deformable mirrors, particularly the thickness of the $SiGe_1$ layer. It can be

observed in Equation 4.6 that the spring constant of the flexural supports is proportional to the moment-of-inertia of the beams, which is proportional to the thickness of the $SiGe_1$ layer to the power of three. Therefore, the thickness of the $SiGe_1$ layer has significant effects on both actuation voltages and resonant frequency. In the following analysis, we use a deformable mirror demonstrated in this thesis research (reported in more detail in Section 4.4) as an example to illustrate the methodology that was used to determine the thickness of the $SiGe_1$ layer. The dimensions of the deformable mirror, except the thickness of the flexural supports, are summarized in Table 4.4.

Table 4.4: Dimensions of a deformable mirror demonstrated in this research

L_1 (μm)	L_2 (μm)	W_1 (μm)	W_2 (μm)	L_j (μm)	W_j (μm)	A_e (μm^2)	m (kg)
200	100	40	10	40	10	203100	1.6×10^{-8}

For vision-science application, the specifications are 10-20 μm of stroke and at least 200 Hz of resonant frequency. To achieve a stroke of ~20 μm, an original gap of ~60 μm is required. Therefore, in this analysis, we assume an original gap (y_0) of 60 μm. Substituting the values in Table 4.4 into Equations 4.6, 4.8, and 4.9, we derive the relationships between the actuation voltages, the resonant frequency, and the thickness of the $SiGe_1$ layer. The relationships are plotted in Figure 4.7 for three thicknesses of the $SiGe_1$ layer (0.8, 0.9, and 1.0 μm). In Figure 4.7, the resonant frequency-displacement curves clearly show the reduction in resonant frequency with increasing displacement. It can be observed

that, as the thickness of the $SiGe_1$ layer increases, the natural resonant frequency increases (0.8 μm: 384 Hz, 0.9 μm: 460 Hz, 1.0 μm: 538 Hz) but all reduces to zero when the displacement reaches 20 μm. The actuation voltage for the same amount of displacement also increases with the thickness of the $SiGe_1$ layer. The straight dotted line drawn in each plot represents the displacement at which the resonant frequency reduces to 200 Hz, the minimum required for vision-science application. The displacement and the actuation voltage required to achieve such displacement are also noted in each plot. When the thickness increases from 0.8 μm to 0.9 μm, the maximum displacement increases from 16 μm to 17.3 μm, and the required actuation voltage also increases from 57 V to 68 V. When the thickness increases to 1 μm, the maximum displacement and actuation voltage increase to 18 μm and 80 V, respectively. Our goal in this research is to develop deformable mirrors that can be integrated with CMOS electronics. Therefore, the voltages required to drive the deformable mirrors need to be within the capability of CMOS technologies. As of early 2008, the highest-voltage CMOS technology offered through MOSIS for engineering runs is an 80-V 0.8-μm CMOS technology. Hence, when designing the deformable mirrors, we chose 80 V to be the highest voltage required to drive the mirrors so that they can be integrated with an easily-accessed CMOS technology. With a voltage limit of 80 V, we should not choose 1.0 μm to be the thickness of the $SiGe_1$ layer because the highest voltage required to drive the deformable mirrors in piston mode would be very close to the voltage limit, leaving no margin

for potential process variations. Based on the result of this analysis, we chose 0.9 μm to be the thickness of the $SiGe_1$ layer.

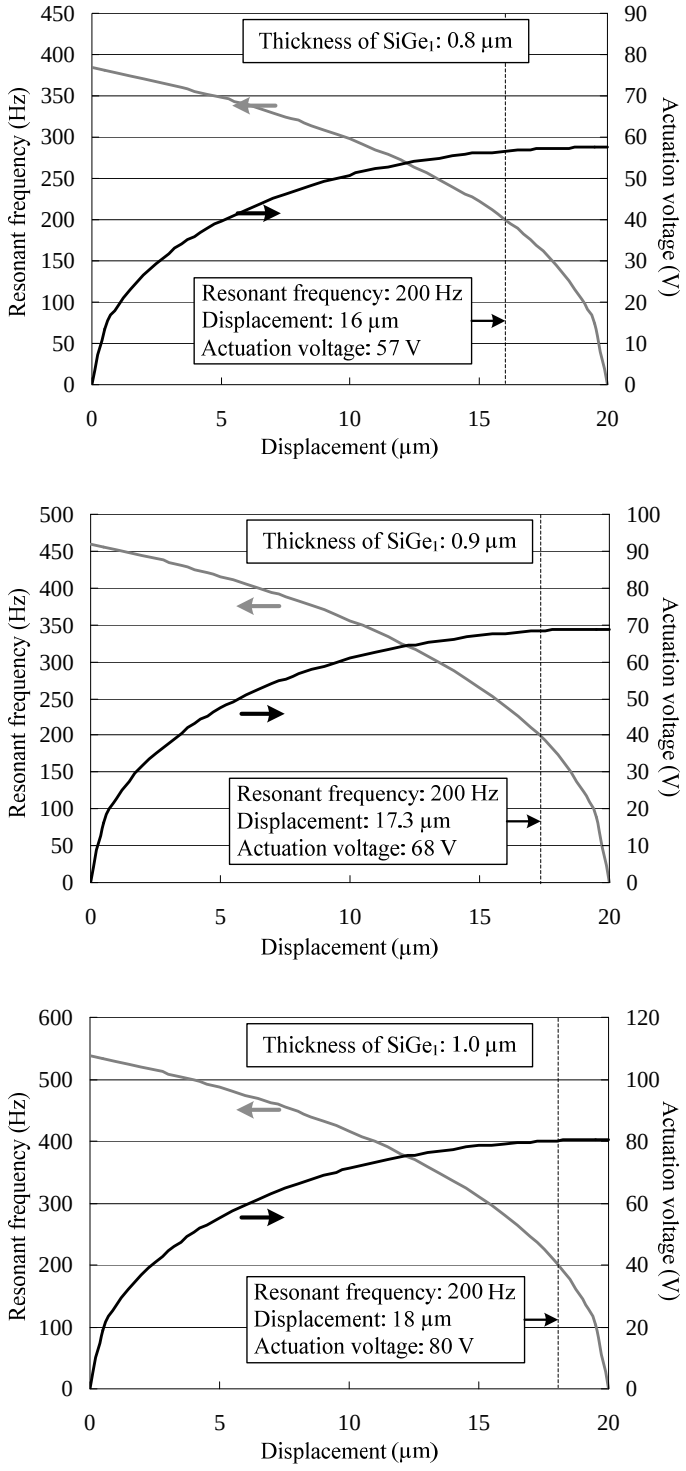

Figure 4.7: Plots showing resonant frequency and actuation voltage versus displacement for different thicknesses of the $SiGe_1$ layer.

4.4 Demonstration of Deformable-Mirror Arrays

Using the micromachining process presented in Section 4.1, we fabricated deformable-mirror arrays in the Microfabrication Laboratory of UC Berkeley. Figure 4.9 shows the layout and a SEM photo of a 37-segment actuator array (before the mirrors were assembled).

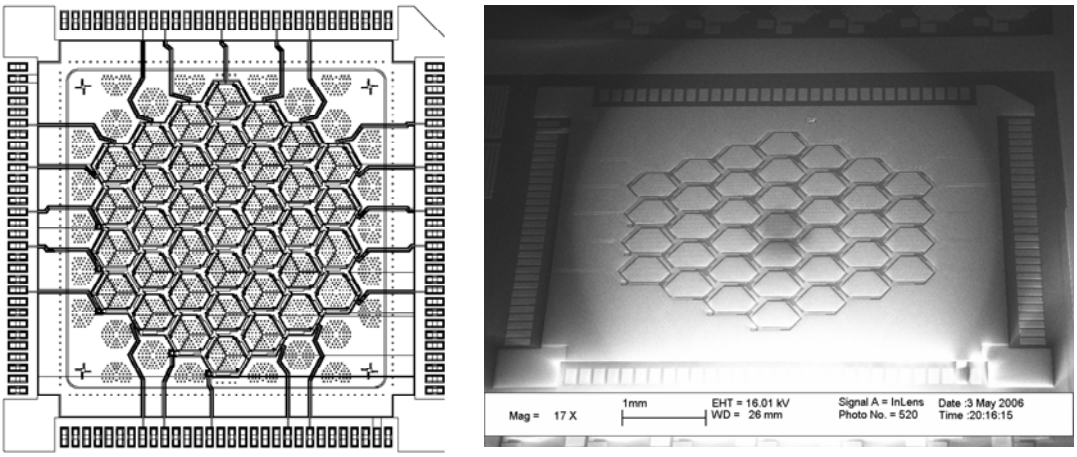

Figure 4.8: Layout (left) and a SEM photo (right) of a 37-segment actuator array

Among all the layers in the deformable-mirror structure, the $SiGe_0$ layer is the only layer that can be used to form signal paths between the bondpads and the electrodes of the deformable mirrors. Therefore, in this demonstration, only the deformable mirrors on the periphery of the array are electrically connected to the bondpads (as seen in Figure 4.8). Because the micromachining process used to

fabricate the deformable-mirror array is compatible with foundry CMOS technologies, the deformable-mirror array can potentially be fabricated directly on top of its control electronics. In that case, signals that drive the deformable mirrors would be supplied to the $SiGe_0$ layer by the underlying electronics.

The 37-segment array shown in Figure 4.8 makes up an aperture size of 3.5 mm in diameter. Although we cannot actuate the deformable mirrors that are not on the periphery of the array, fabricating the deformable mirrors in an array allows us to characterize the cross-array uniformity of the micromachining process.

Figure 4.9 shows SEM photos of a 37-segment deformable-mirror-actuator array (without mirrors assembled on top). The gaps of the parallel-plate actuators were measured using a Wyko interferometer. Across the 37-segment array, the measured values of gaps have a mean of 52.3 μm and a standard deviation of 1.9 μm (which is 3.6% of the mean), and the maximum and minimum are 49.0 μm and 56.0 μm, respectively. The variation is likely due to the fact that we use a single pulse of laser to anneal the poly-SiGe layer that forms the flexural supports. According to the experimental results reported by Sedky et al. [39] and E. Fogarassy et al. [40], the uniformity of pulsed-laser annealing can be significantly improved by using multiple (~10) pulses at the same laser energy, while the depth of penetration remains unchanged.

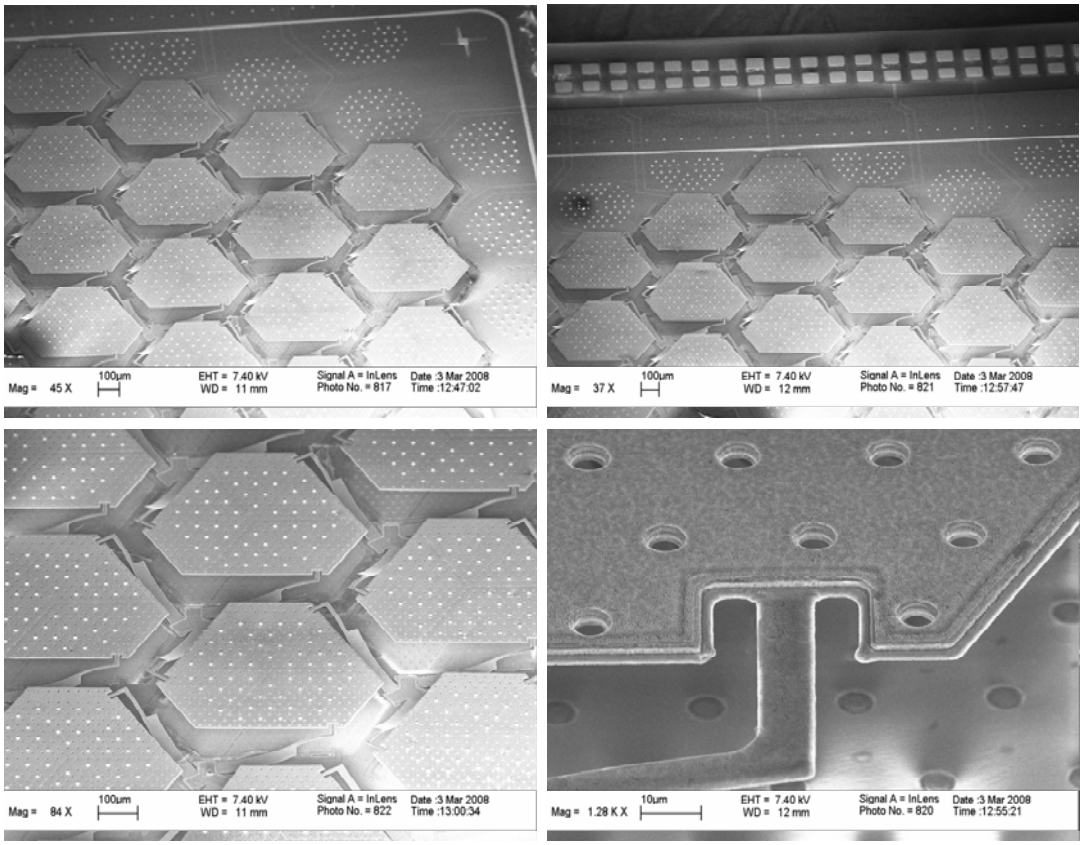

Figure 4.9: SEM photos of a 37-segment deformable-mirror-actuator array (without mirrors assembled on top).

Figure 4.10 shows SEM photos of 37-segment arrays with mirrors assembled on top. The hexagonal mirrors, each having a length of 346 µm on each side (692 µm in diameter), are closely spaced to each other with a gap of 4 µm in between, achieving a fill factor of 98.6%.

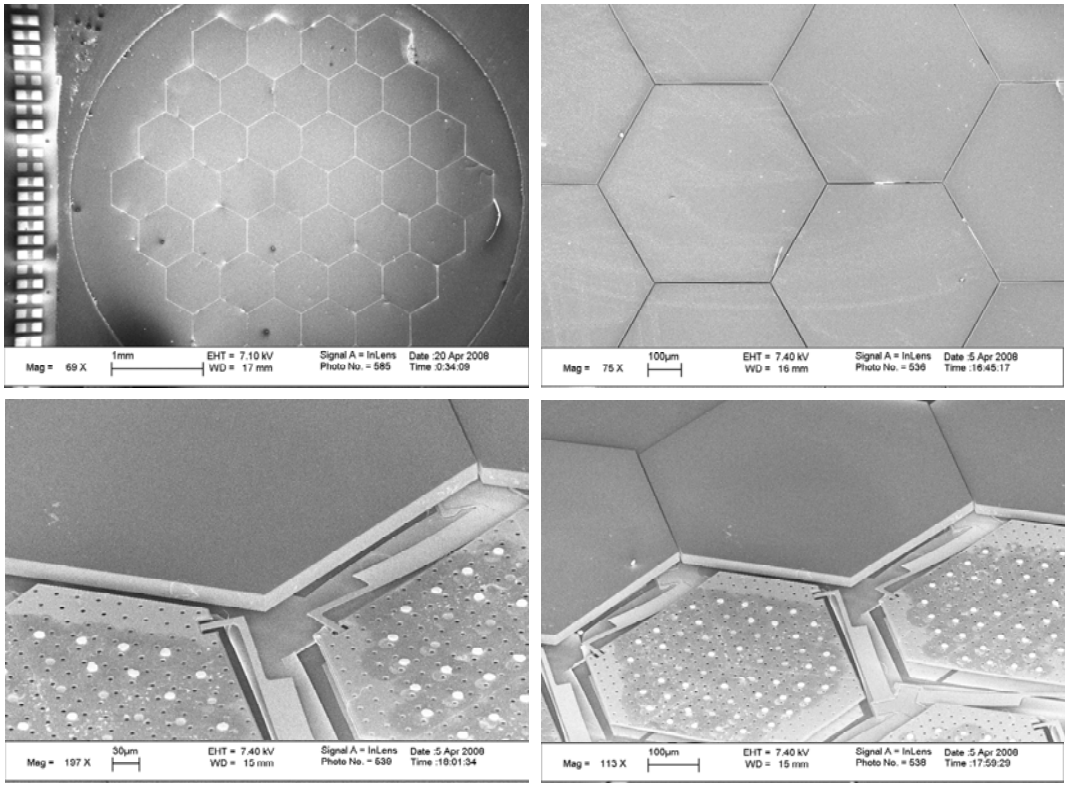

Figure 4.10: SEM photos of 37-segment deformable-mirror arrays. Removing some of the mirrors reveals the underlying actuators.

The surface flatness of the deformable mirrors was measured using a Wyko interferometer. The measurement was taken on released deformable mirrors. Figure 4.11 shows the measured result of one deformable mirror. The root-mean-square (rms) surface deformation (Rq in Figure 4.11) is measured to be 4.38 nm.

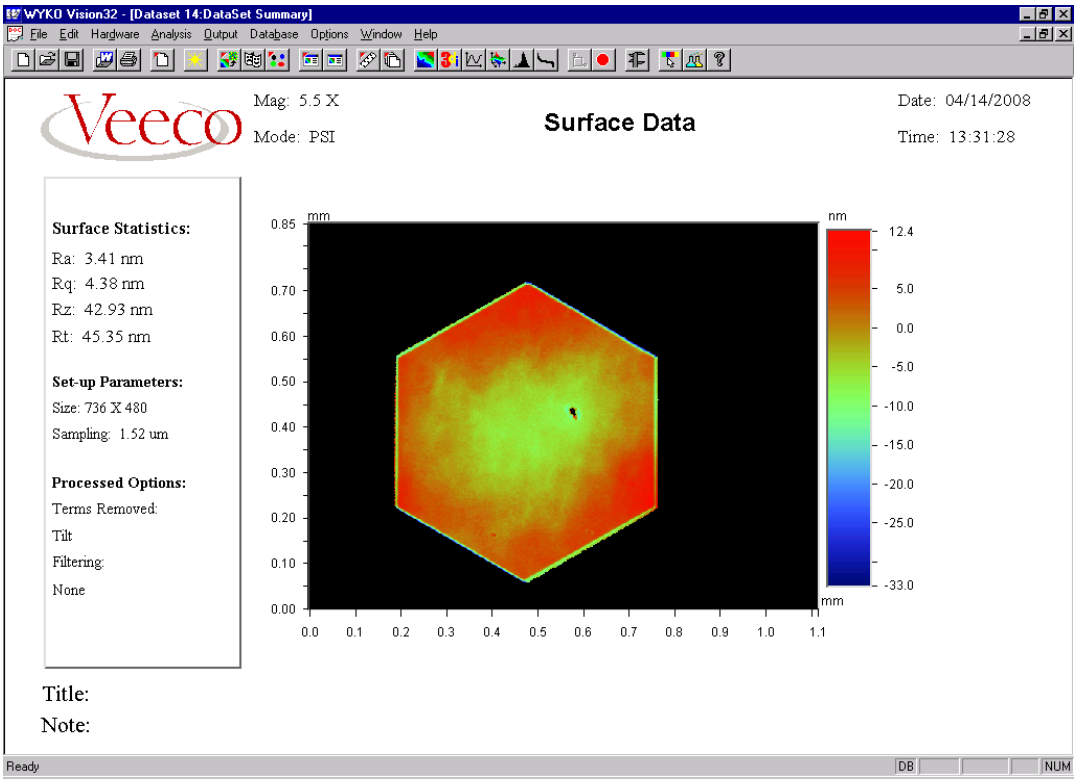

Figure 4.11: Surface quality of a deformable mirror measured using a Wyko interferometer.

In Figures 4.12 and 4.13, we plot the displacements of a deformable mirror at different supplied voltages. The deformable mirror has an initial gap of 52.5 μm. In our actuation scheme, the top electrode of the deformable mirror is electrically grounded, and the control voltages are supplied to one (Figure 4.12) or all three (Figure 4.13) of the bottom electrodes. The measurements were taken using a Wyko interferometer. In the tip/tilt mode, the maximum stroke of the deformable mirror is 15.2 μm (point C in Figure 4.12) at a supplied voltage of 68 V, and the

corresponding maximum tip/tilt angle is 15.7 mrad. In the piston mode (Figure 4.13), the maximum stroke is 16.2 μm at a supplied voltage of 52.5 V.

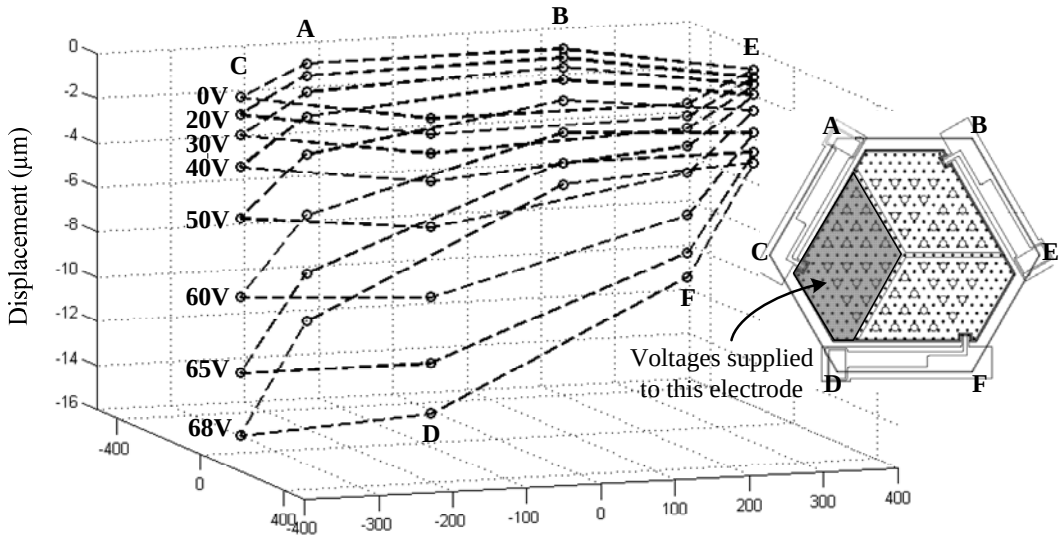

Figure 4.12: Displacements of a deformable mirror actuated in tip/tit mode.

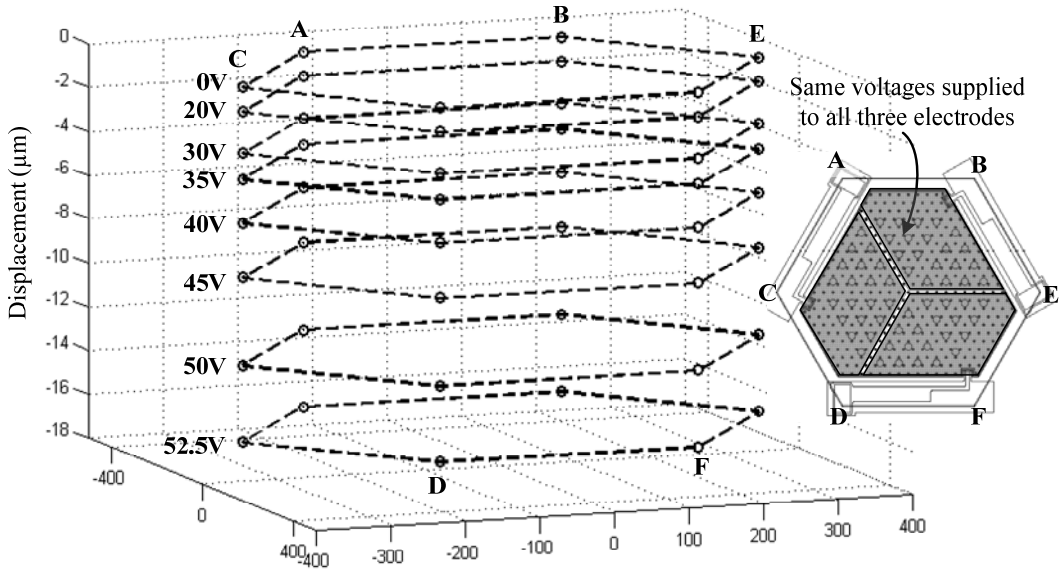

Figure 4.13: Displacements of a deformable mirror actuated in piston mode.

The measured displacements in piston mode are also plotted against the supplied voltages in Figure 4.14. The spring constant derived from the displacement-voltage curve is 0.117 N/m., compared to a predicted value of 0.133 N/m calculated using Equation 4.6.

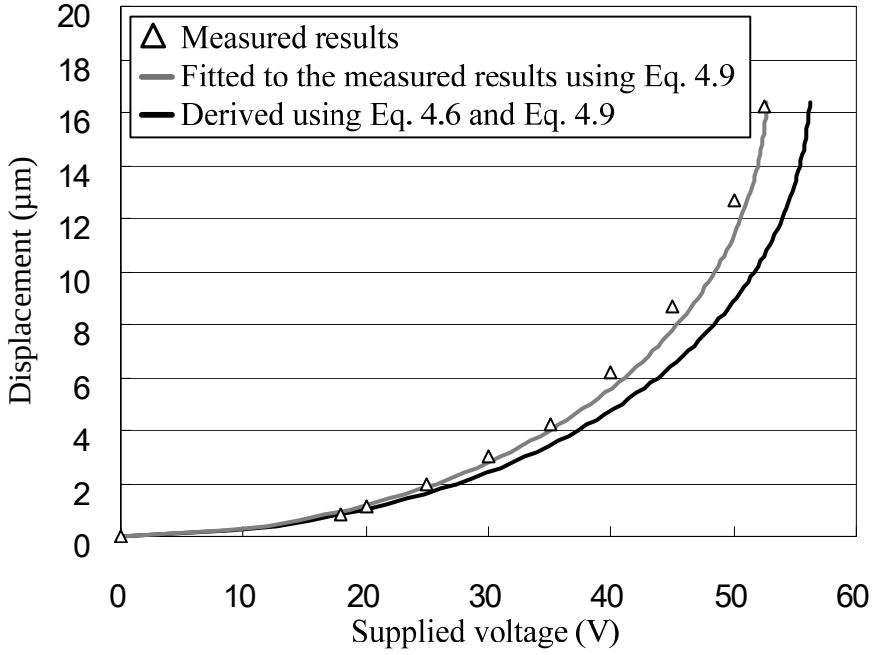

Figure 4.14: Measured displacements plotted against the supplied voltages. Curves derived using Equations 4.6 and 4.9 are also plotted to be compared with the measured results.

Step responses of the deformable mirrors were measured using a Polytec Doppler vibrometer. We plot the measured velocity signals versus time for a deformable-mirror actuator (without a mirror assembled on top) in Figures 4.15-4.16, and for a deformable mirror in Figures 4.17-4.18. The estimated displacements derived from the velocity signals (using discrete integration over time) are also plotted. Figures 4.15 and 4.17 show the responses to a 0V-to-50V transition, and Figures 4.16 and 4.18 show the responses to a 50V-to-0V transition.

The step responses were measured in air, because deformable mirrors for vision-science applications are typically driven in air.

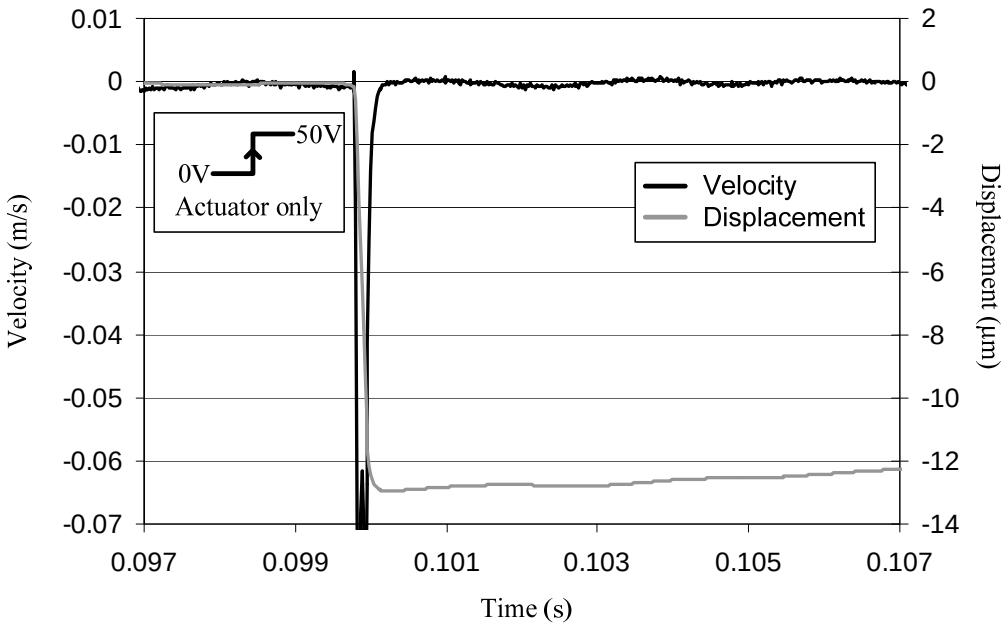

Figure 4.15: Step response of a DM actuator (without mirror) to a 0V-to-50V transition.

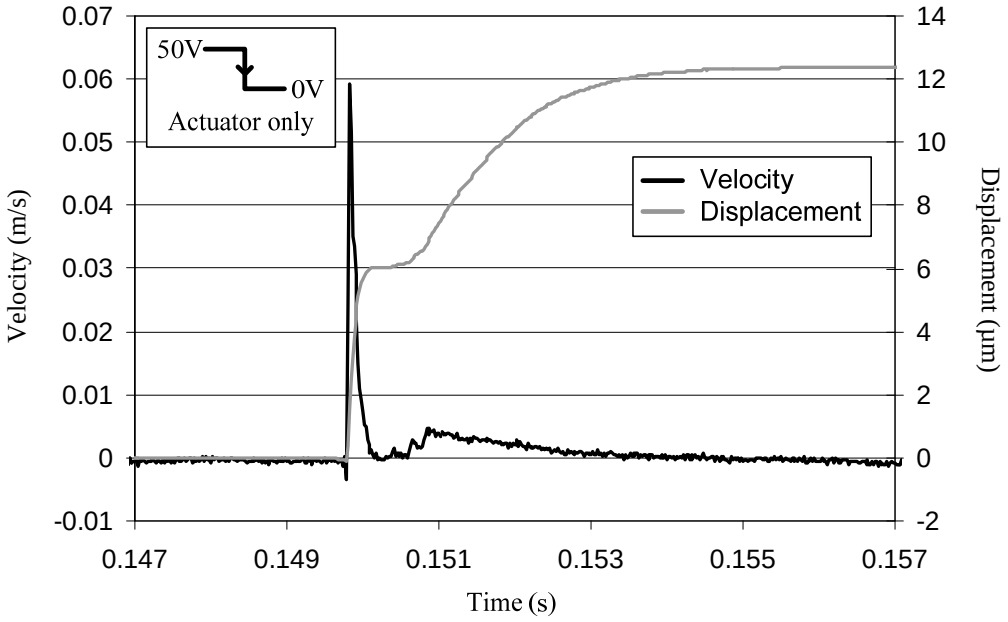

Figure 4.16: Step response of a DM actuator (without mirror) to a 50V-to-0V transition.

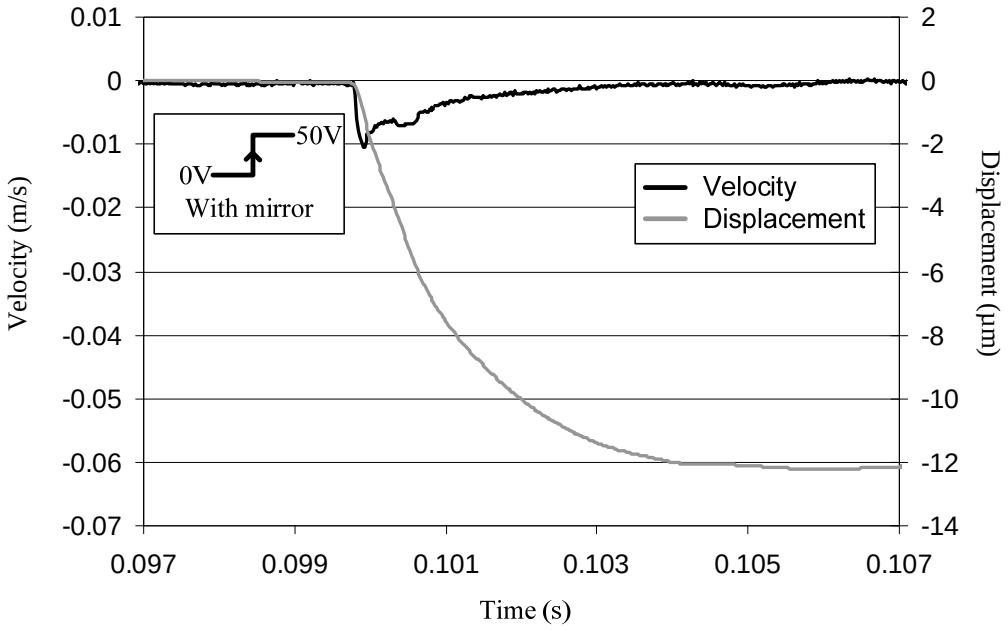

Figure 4.17: Step response of a deformable mirror to a 0V-to-50V transition.

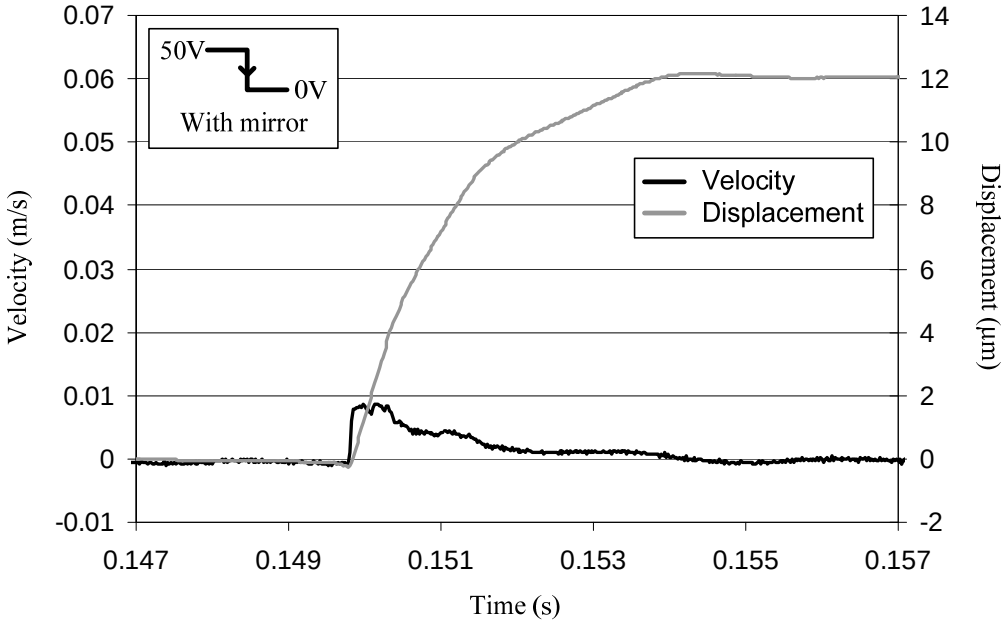

Figure 4.18: Step response of a deformable mirror to a 50V-to-0V transition.

As shown in Figures 4.15-4.18, the mass of the mirror has a significantly effect on the speed of the deformable mirror. Without a mirror, the DM actuator stabilizes within half of a millisecond in response to a 0V-to-50V transition (Figure 4.15). With the additional mass of a mirror, the DM stabiles after about 4 milliseconds (Figure 4.17). Both the actuator and the DM show slower responses to a 50V-to-0V transition than to a 0V-to-50V transition. The actuator (without mirror) stabilizes after about 3.5 milliseconds in response to a 50V-to-0V transition (Figure 4.16), whereas the DM (with mirror) stabilizes after about 6 milliseconds (Figure 4.18).

In practice, for vision-science applications, it is typically required that the deformable mirrors stabilize within one-tenth or one-fifth of time (depending on the specific application) for a data rate of 30 Hz, which is equivalent to a stabilization time within 3 or 6 milliseconds. A stabilization time within 5 milliseconds corresponds to a flat frequency response up to 200 Hz, which is used as a DM-design specification in Section 4.3).

As discussed in Section 4.3, when designing the thickness of the $SiGe_1$ layer, we chose to trade speed for lower actuation voltage. Using a thicker $SiGe_1$ layer would result in faster step responses, but the DMs would also require higher voltages to drive.

The characteristics of the deformable mirrors are summarized in Table 4.5.

Table 4.5: Characteristics of the deformable mirrors demonstrated in this research

Type	Segmented DM
Aperture size	3.5 mm in diameter
Number of segments	37
Mirror-surface flatness	~5 nm rms
Actuation method	Electrostatic
Tip/tilt-mode stroke	15.2 μm (15.7 mrad) maximum at 68 V
Piston-mode stroke	16.2 μm maximum at 52.5V
0V-to-50V stabilization time	4 ms
50V-to-0V stabilization time	6 ms

4.5 Performance Comparison of Deformable Mirrors

Table 4.6 is adapted from Devaney et al. [2] (published in January 2008), in which eight commercially available deformable mirrors are characterized to determine their suitability as the wavefront corrector in adaptive-optics systems. It is informative to compare the characteristics of our deformable-mirror array with these devices.

Table 4.6: Characteristics of deformable mirrors

Mirror	Technology	Diameter (mm)	Actuators	Individual stroke (μm)	Total stroke (μm)
OKO37	Electrostatic	15	37	0.3-0.6	3.5
OKO19_PZT	Piezoelectric	30	19	3, 7-9	--
AOptix35	Bimorph	10.2	35	3, 7	16
MIRAO52	Magnetic	15	52	10-15	25
BMC140	Electrostatic	3.3×3.3	140	1.5	3.5
AgilOptics37	Electrostatic	16	37	0.2-0.6	4.5
IrisAO37	Electrostatic	3.5	37	5	--
OKO37_PZT	Piezoelectric	30	37	2, 3.5-5	--
This work	**Electrostatic**	**3.5**	**37**	**15-16**	**--**

The “individual stroke” in Table 4.6 is the maximum displacement of the mirror surface when the maximum actuation voltage is supplied to only one actuator, whereas the “total stroke” is the maximum displacement when the maximum actuation voltage is supplied to all actuators. For continuous-face-sheet deformable mirrors, the actuator located at the center can pull the mirror surface down much further when the actuators surrounding it are all pulling down the mirror surface at the same time. Therefore, the “total stroke” is much larger than the “individual stroke”. The OKO37, AOptix35, MIRAO52, BMC140, and AgilOptics37 DMs are all continuous-face-sheet DMs.

For segmented deformable mirrors, the displacement of each actuator is unaffected by the actuators surrounding it. The IrisAO37 DM and the DM demonstrated in this work are both segmented DMs. The OKO19_PZT and OKO37_PZT DMs both have an overlying continuous mirror surface, but the movements of the underlying piezoelectric actuators are independent of each other. For these DMs, the “total stroke” is the same as the “individual stroke”.

Compared with the eight commercially available DMs, the DM demonstrated in this work achieves the highest individual stroke (15-16 μm). The MIRAO52 DM has a higher “total stroke” of 25 μm, but the size of its actuators is also much larger (52 actuators in a 15-mm-diameter aperture compared to 37 actuators in a 3.5-mm-diameter aperture).

Most of the compared DMs require actuation voltages greater than 200 V to achieve the maximum strokes [2]. The MIRAO52 DM is driven by magnetic force

and thus requires low voltages but high currents (maximum actuation voltage of ±1 V, maximum power consumption of 50 W [35-37]). Iris AO Inc., the provider of the IrisAO37 DM, has demonstrated another prototype DM (still in development) that can achieve 7 μm of stroke at 60 V [38]. The DM demonstrated in this work achieves 15-16 μm of strokes at voltages below 68 V, and is the only DM fabricated using a CMOS-compatible process. The low actuation voltage makes our DM more suitable for integration with CMOS electronics.

4.6 Conclusion

In this chapter, we present a 37-segment deformable-mirror array that is fabricated using a low-thermal-budget micromachining process. The total thermal budget of the process is below the maximum allowable thermal budget to be integrated with a 0.25 μm foundry CMOS technology. The deformable-mirror array, which has 37 three-degree-of-freedom segments that form an aperture of 3.5 mm in diameter, was designed specifically for vision-science adaptive-optics applications. The DM achieves a maximum stroke of 15-17 μm and a maximum tip/tilt angle of 15.7 mrad (0.9 degree) at a maximum actuation voltage of 68 V.

Chapter 5 : Conclusions

5.1 Contribution of this Research

The technologies developed in this research contribute both to the field of post-CMOS integration of MEMS and the field of MEMS for adaptive optics. In this section, we discuss the contribution of this research in both fields.

Although previous research has shown that poly-SiGe is a promising material for post-CMOS integration of MEMS, high strain gradients in the material has limited its applications to those with small micromechanical structures (less than 200 μm from anchors to freed ends) (e.g. high-frequency micromechanical resonators, as reported in [13]). The bilayer technology developed in this research, as discussed in Chapter 2, allows us to build poly-SiGe micromechanical actuators that have large platforms (ours are hexagonal-shaped with a diagonal of 700 μm) that are sufficiently flat (radius-of-curvature approximately 100 mm) to carry micromirrors. It is shown in this research that the bilayer structure can reduce the effective strain gradient (curvature) of poly-SiGe by 10 to 100 times without any post-deposition annealing.

Besides developing a technology to produce flatter microstructures, we also developed a technology that utilizes the strain gradient of poly-SiGe to build large-vertical-motion microstructures. As shown in Chapters 3 and 4, the bi-width poly-SiGe flexural supports designed and demonstrated in this research can elevate the micromirrors out-of-plane by 52.5 μm. The large out-of-plane elevation significantly enhances the range of vertical motion of the micromechanical device. Moreover, it is demonstrated that we can build microstructures that require both flat and curving parts in the same structure when it is built using two layers of poly-SiGe. The actuated micromirror platform discussed in Chapter 4 has a nearly flat mirror platform (radius-of-curvature approximately 100 mm), and three curving flexural supports each with radii-of-curvature of approximately 0.3 mm. The technologies developed in this research can be applied to other integrated-MEMS applications that require flat microstructures with large vertical motions.

As a contribution to adaptive optics, this research developed technologies and methodologies to design and fabricate a segmented DM that meets specifications required for vision-science AO systems.

Table 5.1 compares eight commercially available DMs as reviewed in Devaney et al. [2] and includes comparable data for a prototype DM that might be built based on the research we have described. Table 4.6 in the previous chapter has shown comparisons regarding stroke. In Table 5.1, we add the information regarding the required actuation voltages for the DMs. The values of the actuation voltages for the commercially available DMs are taken from manufacturers'

datasheets [37-38, 41-43]. None of the DMs shown in Table 5.1 is integrated with control electronics. The control electronics are fabricated on separate chips (or PCB boards), and the control signals are introduced to the micromirror actuators through bond wires.

Table 5.1: Comparisons of deformable mirrors

Mirror	Technology	Diameter (mm)	Actuators	Stroke (μm)	Actuation voltage
OKO37	Electrostatic	15	37	0.3-0.6	150V
OKO19_PZT	Piezoelectric	30	19	3, 7-9	400V
AOptix35	Bimorph	10.2	35	3, 7	300V
MIRAO52	Magnetic	15	52	10-15	±1V (50W)
BMC140	Electrostatic	3.3×3.3	140	1.5	275V
AgilOptics37	Electrostatic	16	37	0.2-0.6	n/a
IrisAO37	Electrostatic	3.5	37	7	60V
OKO37_PZT	Piezoelectric	30	37	2, 3.5-5	400V
This research	**Electrostatic**	**3.5**	**37**	**15-16**	**68V**

Compared with the commercially available DMs, the DM structure demonstrated in this work achieves the longest stroke (15-16 μm). Moreover, the long stroke is achieved using actuators that are relatively small compared with those used in the commercially available DMs. As shown in Table 5.1, the structure demonstrated in this research has 37 actuators in an aperture size of 3.5 mm, which is the size of a human pupil. On the other hand, six of the eight commercially available DMs have similar numbers of actuators but significantly greater aperture sizes (10 to 30 mm). The BMC140 DM has 140 actuators in a square-field array that measures 3.3×3.3 mm^2, but the actuators in the BMC device provide only

piston motion (one degree-of-freedom). The stroke of the BMC140 DM is also significantly lower than that achieved by the structure demonstrated in this research.

As for the actuation voltage, the structure demonstrated in this research requires 68 V to achieve the maximum stroke of 16 μm. As shown in Figure 5.1, this actuation voltage is substantially lower than those required by most of the commercially available DMs. The MIRAO52 DM is driven by magnetic force and thus requires low voltages but high currents (maximum actuation voltage of ±1 V, maximum power consumption of 50 W [35-37]). The DM demonstrated in this research is driven by electrostatic force. Due to the large gap between the parallel-plate electrodes (area: 203100 μm^2, gap: 36.5-52.5 μm, dielectric constant: 1), the capacitances of the electrostatic actuators are extremely low (in the range of 30-50 fF). Consequently, the current that is required to actuate the micromechanical device is expected to be very low (e.g. the average current required to charge a capacitance of 50 fF from 0 to 68 V in 3 ms is approximately 1nA). Therefore, we can expect the electrostatic actuators to dissipate very low power. In the case when the DM is integrated with CMOS control electronics, the power consumption of the integrated device would mostly be contributed by the CMOS, which would be required to deliver up to 68V to the DM actuators.

A major and unique achievement of this research has been to develop a fabrication procedures for the DM array that enables compatibility with the process needed to produce CMOS selection and drive electronics. The thermal steps in the

micromachining process to fabricate the DM demonstrated in this research are summarized in Table 5.2. The highest-temperature step in the micromachining process is at 425°C for 170 minutes.

Table 5.2: Thermal steps in the micromachining process to fabricate the DM demonstrated in this research

Step	Processing temperature of step (°C)	Time of step (min)	Temperature-stabilization time of the furnace (min)	Total processing time of step (min)
Deposition of $SiGe_0$	410	40	60	100
Deposition of LTO_1	400	17	60	77
Deposition of poly-Ge	350	150	60	210
Deposition of $SiGe_1$	425	110	60	170
Deposition of LTO_2	400	20	60	80
Deposition of $SiGe_2$	410	180	60	240
Flip-chip bonding	350	10	--	10

The research result that we have presented demonstrates a means to produce a DM array that meets the specifications for vision-science AO applications. We have also shown that this process can be carried out subsequent to (and overlaying) a previously processed CMOS select-and-drive integrated circuit

5.2 Recommended Future Research Directions

The ultimate goal of this research is to fabricate the DMs directly on top of the addressing and controlling CMOS integrated circuits. The fabrication process for the micromechanical structures has been developed, but we did not fabricate the DMs on top of an array of control electronics. Further research is required to design

an integrated-circuit array for the 37-segmented DM array demonstrated in this thesis. After the control electronics are fabricated, the micromechanical structures can then be fabricated on top of them to demonstrate a fully-integrated DM array.

In this research, we focused on AO applications to vision science. Another important field of AO applications is astronomy, in which DMs with actuator counts in the range of hundreds to thousands are required [1]. The CMOS control electronics can be designed and laid-out in a manner similar to that used when building an SRAM array. The well-established procedure is to input digital control signals for the individual DMs from the periphery of the array. Analog control signals would be used for individual mirrors to provide for continuous control.

The DMs used in astronomy AO systems have to meet different specifications from those used in vision-science AO systems. AO for astronomy requires a mirror stroke of approximately 4 μm and a frequency bandwidth in the range of 4 to 10 kHz, depending on the applications [1]. Using an analysis similar to the one used in Section 4.3, it can be shown that the thickness of the flexural supports would need to be approximately 4.2 μm in order to achieve a frequency-bandwidth of at least 4 kHz. However, the deposition recipe that was developed in this research cannot be used to deposit 4.2 μm of poly-SiGe for the flexural supports, because the required deposition time would exceed the maximum allowable thermal budget limit imposed by CMOS-compatibility. Further research would be required to develop another deposition recipe that can be used to deposit 4.2 μm of poly-SiGe at a deposition temperature lower than 425°C, so that the total

thermal budget of the micromachining process would be within the limit allowed by the CMOS.

Furthermore, to achieve a stroke of 4 μm using an electrostatic parallel-plate actuator, an original gap of approximately 16 μm is required. Further research would be required to develop an excimer-pulsed-laser annealing step that can enhance the strain gradient of the 4.2 μm-thick poly-SiGe to achieve an original gap of approximately16 μm.

Bibliography

[1] M. A. Helmbrecht, *Micromirror Arrays for Adaptive Optics*, Ph.D. Thesis, Dept. of Electrical Engineering and Computer Sciences, University of California, Berkeley, (2002).

[2] N. Devaney, D. Coburn, C. Coleman, J. C. Dainty, E. Dalimier, T. Farrell, D. Lara, D. Mackey, and R. Mackey, "Characterization of MEMs mirrors for use in atmospheric and ocular wavefront correction," *Proc. of SPIE,* Vol. 6888, 688802, (2008).

[3] E. Dalimier and C. Dainty, "Comparative analysis of deformable mirrors for ocular adaptive optics," *Optics Express*, Vol. 13, Issue 11, pp. 4275-4285, (2005).

[4] E. Daly, E. Dalimier, and C. Dainty, "Requirements for MEMS mirrors for adaptive optics in the eye," *Proc. of SPIE*, Vol. 6113, 611309, (2006).

[5] T. Farrell, E. Daly, E. Dalimier, and C. Dainty, "Task-based assessment of deformable mirrors," *Proc. of SPIE*, Vol. 6467, 64670F, (2007).

[6] A. E. Franke, *Polycrystalline Silicon-Germanium Films for Integrated Microsystems*, Ph.D. Thesis, Dept. of Electrical Engineering and Computer Sciences, University of California, Berkeley, (2000).

[7] A. E. Franke, J. M. Heck, T.-J. King, and R. T. Howe, "Polycrystalline silicon-germanium films for integrated microsystems," *Journal of Microelectromechanical Systems*, Vol. 12, pp. 160-171, (2003).

[8] S. A. Bhave, B. L. Bircumshaw, W. Z. Low, Y.-S. Kim, A. P. Pisano, T.-J. King, and R. T. Howe, "Poly-SiGe: a high-Q structural material for post-CMOS integrated RF MEMS," *Solid-State Sensor, Actuator, and Microsystems Workshop* (Hilton Head 2002), Hilton Head Island, SC, pp. 34-37, (2002).

[9] J. M. Heck, *Polycrystalline Silicon Germanium for Fabrication, Release, and Packaging of Microelectromechanical Systems*, Ph.D. Thesis, Appl. Sci. and Tech., University of California, Berkeley, (2001).

[10] B. C.-Y. Lin, T.-J. King, and R. T. Howe, "Optimization of poly-SiGe deposition processes for modular MEMS integration," *Mat. Res. Soc. Symp. Proc.*, Vol. 782, pp. A2.4.1-A2.4.6, (2004).

[11] M. A. Eyoum and T.-J. King, "Low resistance silicon-germanium contact technology for modular integration of MEMS with electronics," *Journal of Electrochemical Society*, Vol 151, No. 3, pp. J21-J25, (2004).

[12] B. L. Bircumshaw, M. L. Wasilik, E. B. Kim, Y. R. Su, H. Takeuchi, C. W. Low, G. Liu, A. P. Pisano, T.-J. King, and R. T. Howe, "Hydrogen peroxide etching and stability of p-type poly-SiGe films," *17th IEEE International Conference on Micro Electro Mechanical Systems (MEMS)*, pp. 514- 519, (2004).

[13] A. E. Franke, Y. Jiao, M. T. Wu, T.-J. King, and R. T. Howe, "Post-CMOS modular integration of poly-SiGe microstructures using poly-Ge sacrificial layers," *Tech. Dig. 2000 Solid State Sensor and Actuator Workshop*, pp. 18-21, (2000).

[14] T.-J. King, R. T. Howe, S. Sedky, G. Liu, B. C.-Y. Lin, M. Wasilik, and C. Duenn, "Recent progress in modularly integrated MEMS technologies," *Digest. International Electron Devices Meeting 2002*, pp. 199-202, (2002).

[15] M. Wasilik, "Silicon-germanium film deposition characteristics in Tystar 20," presented at the *Industrial Advisory Board*, (Berkeley Sensor & Actuator Center), Berkeley, CA, (2002).

[16] R. T. Howe and T.-J. King, "Low-Temperature LPCVD MEMS Technologies," *Mat. Res. Soc. Symp. Proc.*, Vol. 729, pp. U5.1.1-U5.1.9, (2002).

[17] C. W. Low, *Novel Processes for Modular Integration of Silicon-Germanium MEMS with CMOS Electronics*, Ph.D. Thesis, Dept. of Electrical Engineering and Computer Sciences, University of California, Berkeley, (2007).

[18] C. W. Low, T.-J. King Liu, and R. T. Howe, "Characterization of polycrystalline silicon-germanium film deposition for modularly integrated MEMS applications," *Journal of Microelectromechanical Systems*, Vol. 16, No.1, pp. 68-77, (2007).

[19] S. Sedky, R. T. Howe, and T.-J. King, "Pulsed-laser annealing, a low-thermal-budget technique for eliminating stress gradient in poly-SiGe

MEMS structures," *Journal of Microelectromechanical Systems*, Vol. 13, Issue 4, pp. 669-675, (2004).

[20] S. Sedky, J. Schroeder, T. Sands, R. T. Howe, and T.-J. King, "Pulsed Laser Annealing of Silicon-Germanium Films," *Mat. Res. Soc. Symp. Proc.*, Vol. 741, pp. J4.2.1-J4.2.6, (2003).

[21] S. Sedky, J. Schroeder, T. Sands, T.-J. King, and R. T. Howe, "Effect of excimer laser annealing on the structural properties of silicon germanium films," *J. Mater. Res.*, Vol. 19, No. 12, pp. 3503-3511, (2004).

[22] S. Sedky, M. Gromova, T. Van der Donck, J.-P. Celis and A. Witvrouw, "Characterization of KrF excimer laser annealed PECVD Si_xGe_{1-x} for MEMS postprocessing," *Sensors and Actuators A*, Vol. 127, pp. 316-323, (2006).

[23] C. W. Low, *Excimer laser annealing of silicon germanium for MEMS applications*, M.S. report, Dept. of Electrical Engineering and Computer Sciences, University of California, Berkeley, (2004).

[24] A. E. Franke, J. M. Heck, T.-J. King, and R. T. Howe, "Polycrystalline silicon-germanium films for integrated microsystems," *Journal of Microelectromechanical Systems*, Vol. 12, pp. 160-171, (2003).

[25] A. E. Franke, Y. Jiao, M. T. Wu, T.-J. King, and R. T. Howe, "Post-CMOS modular integration of poly-SiGe microstructures using poly-Ge sacrificial layers," *Tech. Dig. 2000 Solid State Sensor and Actuator Workshop*, pp. 18-21, (2000).

[26] A. E. Franke, D. Bilic, D. T. Chang, P. T. Jones, T.-J. King, R. T. Howe, and G. C. Johnson, "Post-CMOS integration of germanium microstructures," *Proc. IEEE Int. Conf. Micro Electro Mechanical Systems* Orlando, pp. 630-637, (1999).

[27] E. P. Quévy, A. San Paulo, E. Basol, R. T. Howe, T.-J. King, and J. Bokor, "Backend-of-line Poly-SiGe disk resonators," *19th IEEE Micro Electro Mechanical Systems Conference (MEMS-06)*, Istanbul, Turkey, (2006).

[28] A. Witvrouw, A. Mehta, A. Verbist, B. Du Bois, S. Van Aerde, J. Ramos-Martos, J. Ceballos, A. Ragel, J. M. Mora, M. A. Lagos, A. Arias, J. M. Hinojosa, J. Spengler, C. Leinenbach, T. Fuchs and S. Kronmüller, "Processing of MEMS gyroscopes on top of CMOS ICs," *Proc. 52nd IEEE International Solid-State Circuits Conference*, San Francisco, CA, pp. 88-89, (2005).

[29] H. Takeuchi, A. Wung, X. Sun, R. T. Howe, and T.-J. King, "Thermal budget limits of quarter-micrometer foundry CMOS for post-processing MEMS devices," *IEEE Transactions on Electron Devices*, Vol. 52, Issue 9, pp. 2081-2086, (2005).

[30] S. Sedky, A. Witrouw, H. Bender, and K. Baert, "Experimental determination of the maximum annealing temperature for standard CMOS wafers," *IEEE Trans. Electron Devices*, Vol. 48, No. 4, pp. 377-385, (2001).

[31] C. W. Low, *Novel Processes for Modular Integration of Silicon-Germanium MEMS with CMOS Electronics*, Ph.D. Thesis, Dept. of Electrical Engineering and Computer Sciences, University of California, Berkeley, (2007).

[32] M. A. Helmbrecht, *Micromirror Arrays for Adaptive Optics*, Ph.D. Thesis, Dept. of Electrical Engineering and Computer Sciences, University of California, Berkeley, (2002).

[33] U. Srinivasan, M. A. Helmbrecht, C. Rembe, R. S. Muller, and R. T. Howe, "Fluidic self-assembly of micromirrors onto surface micromachined actuators," *Proc. 2000 IEEE/LEOS Int. Conf. Optical MEMS* Kauai, HI, pp. 59-60, (2000).

[34] M. A. Helmbrecht, U. Srinivasan, C. Rembe, R. T. Howe, and R. S. Muller, "Micromirrors for adaptive-optics arrays," *Transducers '01, Proc. 11th Int. Conf. Solid State Sensors and Actuators*, pp. 1290-1293, (2001).

[35] S. Tuohy, A. Bradu, A. Gh. Podoleanu, N. Chateau, "Correcting ocular aberrations with a high stroke deformable mirror," *Proc. of SPIE-OSA Biomedical Optics*, SPIE Vol. 6627, 66271L, (2007).

[36] E. J. Fernandez, L. Vabre, B. Hermann, A. Unterhuber, B. Povazay, and W. Drexler, "Adaptive optics with a magnetic deformable mirror: applications in the human eye," *Optics Express*, Vol. 14, Issue 20, pp. 8900-8917, (2006).

[37] Imagine Optic website. http://www.imagine-optic.com/iop_en_products_mirao_main.php

[38] M. A. Helmbrecht. Iris AO, Inc., personal communication, (2007).

[39] S. Sedky, R. T. Howe, and T.-J. King, “Pulsed-laser annealing, a low-thermal-budget technique for eliminating stress gradient in poly-SiGe MEMS structures,” *Journal of Microelectromechanical Systems,* Vol. 13, Issue 4, pp. 669-675, (2004).

[40] E. Fogarassy, B. Prevot, S. de Unamuno, C. Prat, D. Zahorski, Y. Helen, and T. Mohammed-Brahim, “Long-pulse duration excimer laser processing in the fabrication of high performance polysilicon TFTs for large area electronics,**”** *Mat. Res. Soc. Symp. Proc.*, Vol. 685E, pp. D7.1.1-D7.1.11, (2001).

[41] Flexible Optical BV (a.k.a. OKO Tech) website. http://www.okotech.com/

[42] AOptix Technologies website. http://www.aoptix.com/

[43] Boston Micromachines Corporation website. http://www.bostonmicromachines.com/